1500-2100 Forcing Impacts on the Freshwater Balance in Polar Regions

Master's thesis

Faculty of Science

University of Bern

presented by

Flavio Lehner

2009

Supervisor:

Prof. Dr. Thomas F. Stocker

Co-Supervisor:

PD Dr. Christoph C. Raible

Climate and Environmental Physics

Physics Institute of the University of Bern

Contents

1 Introduction **1**
- 1.1 Background and motivation . . . 2
- 1.2 State of knowledge . . . 3
- 1.3 Geographical characteristics of the Arctic and Antarctic region . . . 6
- 1.4 Objectives . . . 9

2 Model and experimental design **10**
- 2.1 Model description . . . 10
  - 2.1.1 Model components . . . 10
  - 2.1.2 Climate and hydrological sensitivity . . . 11
  - 2.1.3 River runoff . . . 12
- 2.2 Experimental design . . . 20
- 2.3 Methods . . . 22
  - 2.3.1 Regridding . . . 22
  - 2.3.2 Calculations . . . 23

3 Changes in the freshwater cycle and possible feedbacks **26**
- 3.1 Freshwater flux components . . . 26
  - 3.1.1 Freshwater flux to the ocean . . . 26
  - 3.1.2 Precipitation, evaporation, runoff and sea ice meltwater . . . 31
  - 3.1.3 Annual and seasonal variability . . . 31
- 3.2 Freshwater Budget . . . 37
  - 3.2.1 Arctic region . . . 37
  - 3.2.2 Arctic Ocean basin . . . 40
  - 3.2.3 Antarctic region . . . 41
- 3.3 Freshwater transport and Meridional Overturning . . . 47
  - 3.3.1 Ocean passages . . . 47
  - 3.3.2 Deep water formation sites . . . 50
  - 3.3.3 Meridional Overturning . . . 56
- 3.4 Comparison with observations and other models . . . 63
- 3.5 Discussion . . . 70
  - 3.5.1 Summary of main results . . . 70
  - 3.5.2 Related work and comparison to other studies . . . 73

4 Conclusions **76**

5 Outlook **78**

A Ocean data **80**

List of Tables **83**

List of Figures **85**

References **86**

Abstract

Despite the scientifically consistent picture of climate change, a comprehensive understanding of the hydrological cycle, which is of fundamental importance for the climate system, is still missing – especially in polar regions. To assess changes of the hydrological cycle in polar regions we use a series of simulations with the Community Climate System Model version 3 (CCSM3) from NCAR. Starting from different initial conditions an ensemble of four transient simulations from 1500 to 2100 (with natural forcing and the SRES scenario A2 from 2000 to 2100) is generated. Thereby future changes are placed in the context of the pre-industrial climate (1500-1870). These long ensemble simulations enable us to assess changes on the basis of a robust data set. We found the freshwater cycle and budget in the polar regions to vary little during the pre-industrial period, while the simulations project substantial changes as a response to the increasing greenhouse gas concentrations in the future. These changes in polar regions occur in a temporally and spatially non-uniform way and exert a strong feeback on lower latitudes. In the Arctic region the freshwater import increases stronger than the export, transforming the Arctic Ocean from a freshwater source to a sink with a decreasing density and a rising sea surface height. Discharge from rivers dominates these freshwater budget changes. The Southern Ocean, on the other hand, loses freshwater due to the fact that oceanic export exceeds atmospheric import of freshwater. In the Northern Hemisphere distinct changes of the freshwater discharge through ocean passages to adjacent ocean basins are identified which alter deep-water formation and consequently the Atlantic Meridional Overturning Circulation. The latter is decreasing by about 20% until the end of the 21st century. In the Southern Hemisphere, local modifications in sea ice production and other ocean surface freshwater forcing cause changes in deep-water formation. Based on these projections, substantial changes in the distribution of water masses on hemispheric scale are expected for the 21st and subsequent centuries.

Chapter 1

Introduction

Strong and growing evidence is at hand that the Earth's climate has undergone distinct changes in the past, and more recently, since the beginning of the industrialisation in the 19^{th} century. The United Nations Intergovernmental Panel on Climate Change (IPCC) concluded in its 4^{th} Assessment Report (AR4) in 2007 that a large part of this ongoing change is – for the first time in history – caused by anthropogenic influence and is very likely to be maintained throughout the 21^{st} century. Rising carbon dioxide (CO_2) emissions and concentrations are identified as one of the major causes of these changes, prominently characterized by increasing temperatures due to enhanced absorption of terrestrial long-wave radiation. Together with CO_2, other climate-relevant gases are summarized under the term greenhouse gases. Atmospheric CO_2 concentration has experienced significant variations in the past, fluctuating within a range of 172-300 ppmv during the last 800,000 years (*Lüthi et al.* [2008]). In 2009, the concentration is currently 387 ppmv (source: http://www.esrl.noaa.gov/gmd/ccgg/trends/ [13.08.2009]) and it was shown that the 20^{th} century increase occured at a rate more than two magnitudes larger than any prolonged change in the last 22,000 years (*Joos and Spahni* [2008]). Caused mainly by energy production and industry as well as land use change, CO_2 emissions are assumed to continue to rise to meet the growing energy and land demand of human society. The question as to how the climate system will react to this anthropogenic forcing is difficult to answer, as it is influenced by many factors. On the one hand, the understanding of the complex climate system is still limited, even though remarkable progress and robust consensus have been achieved in the past decades. On the other hand it is impossible to precisely predict how greenhouse gas emissions will develop in the future or what mitigation option human society will take. The two problems are addressed simultaneously by defining different future scenarios of greenhouse gas emissions and using models to estimate climate system changes based on the assumed greenhouse gas forcing. Along with reconstructions and measurements, models are therefore a valid tool to investigate the changes in Earth's climate – especially since they are the only possibility assessing its future.

This study aims at investigating the changes of the freshwater cycle in polar regions from 1500-2100 utilizing a state-of-the-art coupled general circulation model described in chapter 2. Chapter 3 presents the results and is composed of an analysis of the freshwater budget and flux terms and a discussion on possible consequences of changing flux terms.

This first chapter presents a short introduction on parts of the freshwater cycle and its ge-

ographical setting, as well as an overview on the current knowledge and the motivation for this study.

1.1 Background and motivation

Within the climate system the ocean plays a key role. It serves as carbon and heat storage and along with water masses distributes the heat excess of the equatorial regions to higher latitudes. The latter is achieved by the Thermohaline Circulation (THC), a global system of ocean currents driven by density differences, the arrangement of the continents and the Earth's rotation. A simplified global view of the THC is shown in Fig. 1.1 where warm surface and cold deep currents are given in red and blue-to-purple, respectively.
As the warm and salty surface waters are transported to higher latitudes they become colder and therefore denser. They also freshen, which slightly counteracts the cooling-induced density increase. In the Nordic Seas, the Labrador Sea, the Weddell Sea and the Ross Sea these increasingly dense waters start to subside or convect and flow back towards lower latitudes as intermediate and deep currents. These areas of subsiding waters are referred to as deep water formation sites and are represented as yellow dots in Fig. 1.1. The downwelling of water masses is governed by the high in-situ density and is therefore very sensitive to changes in heat and freshwater flux to the ocean surface, as they both influence density. It has been stated that a sudden influx of large quantities of freshwater from an ice sheet into the Labrador Sea during the last ice age might have caused frequent shut-downs of the THC ("Heinrich event", *Heinrich*, 1988, *Broecker et al.*, 1992), simply due to the drastically reduced density (*Stocker*, 2000, *Hemming*, 2004). In the AR4 the IPCC projects the Meridional Overturning Circulation (MOC), as the meridional component of the THC, to weaken during the 21st century due to increasing temperature and precipitation in high latitudes (*IPCC*, 2007). Furtheron, the river and sea ice meltwater discharge to the ocean is predicted to increase, prompting a

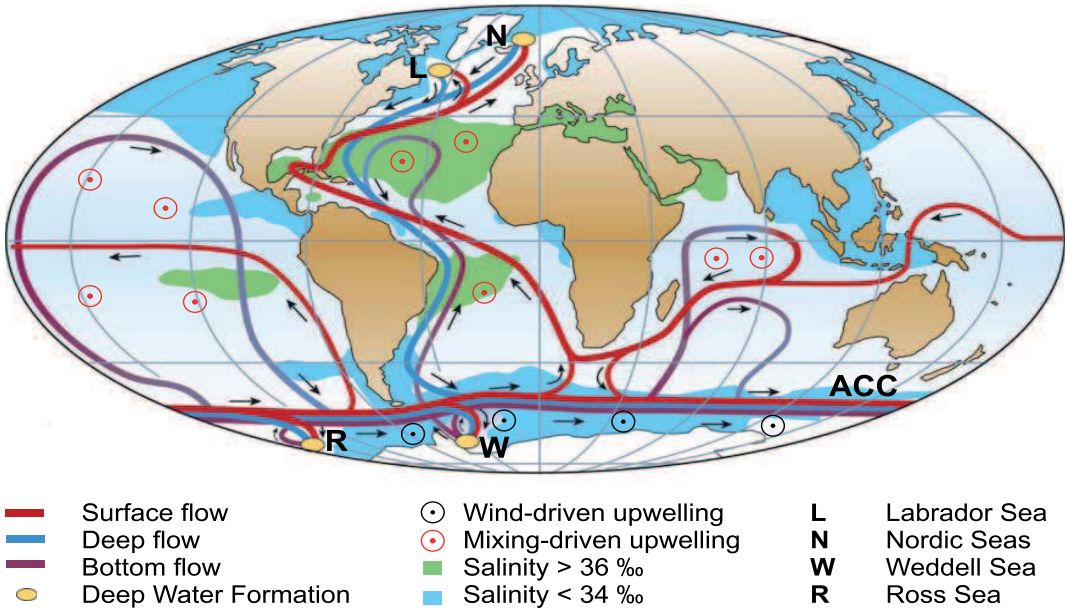

Figure 1.1: Simplified scheme of the Thermohaline Circulation (figure from *Kuhlbrodt et al.*, 2007).

discussion on a possible reduction of the convection in the Labrador Sea due to the increased influx of freshwater.

On a global scale the freshwater flux to the ocean is expected to change in a non-uniform way. This rises the question about a possible redistribution of major water masses in the hydrological cycle and specifically the ocean (*Stocker and Raible*, 2005). Since the differential meridional freshwater forcing is assumed to be one of the prime factors determining the MOC in the Atlantic Ocean (*Wu et al.*, 2007), it is essential to further investigate the freshwater cycle and its evolution under changing forcing parameters, whereby a special focus on the polar regions is required.

1.2 State of knowledge

While climate change is expected to have a growing impact on ecosystems on a mid- to long-term perspective, dramatic changes have already been observed in the Arctic region during the last century. The Arctic region is also expected to be disproportionally affected by the global warming that is still ahead. At the same time, this sensible region may itself be able to exert a strong feedback on global climate (*IPCC*, 2007). Therefore, monitoring climate change in the Arctic region has lately become a research area of growing activity (e.g., *Curry et al.*, 2003, *ACIA*, 2004, *Serreze et al.*, 2006), along with several attempts to model and predict future changes.

Regarding the freshwater cycle of the Arctic region, substantial changes of storage and flux terms are observed (*White et al.*, 2007). On land, precipitation, river runoff, lake abundance and size, glacier area and volume, soil moisture and permafrost characteristics have changed whereas in the ocean a decrease of sea ice thickness and areal coverage as well as shifts in water mass circulation patterns have been observed (*White et al.*, 2007). Together with changing precipitation patterns over the ocean, this again alters the freshwater exchange between the ocean and the atmosphere, possibly triggering other feedbacks (*White et al.*, 2007).

The atmospheric meridional moisture transport is the predominant source of water for the Arctic region and exhibits an upward trend during the second half of the 20^{th} century. However, the uncertainty of this quantity's trend is considerable as it is superimposed by large inter-annual variability and the strong connection to large-scale atmospheric circulation pattern such as the North Atlantic Oscillation (NAO; *Groves and Francis*, 2002). Moreover, observational data over the ocean area is sparse.

River runoff to the Arctic Ocean is thought to play a significant role in changing the Arctic freshwater budget and receives increasing attention by the scientific community in recent years. *Peterson et al.* [2002] compiled gauge data from several Eurasian river discharging into the Arctic Ocean and found a trend of 2.0 ± 0.7 km^{3}yr^{-1} per year for the period of 1936 to 1999 which amounts to an increase in runoff of about 7%. From a comparison with the NAO it is concluded that the rivers are responding to changes in large-scale hemispheric climate patterns (*Peterson et al.*, 2002), which can cause anomalies in precipitation over Siberia (*Dickson et al.*, 2000). From a linear regression with global surface temperature (SAT) a

trend of 212 ± 69 km^3yr^{-1} per °C was estimated. Applying this trend to projections of SAT for 2100 by the IPCC, a roughly estimated increase of 315 to 1,260 km^3yr^{-1} is projected for the Eurasian river runoff by the end of the 21st century. A continuation of the observed upward trend in river runoff to the Arctic Ocean is predicted also by *Wu et al.* [2005], who used the HadCM3 to simulate the climate of the 20th and 21st century. They expect a rise from a 20th century mean of about 3,300 km^3yr^{-1} to approximately 4,000 km^3yr^{-1} by the end of the 21st century. Comparing a simulation with anthropogenic forcing to a simulationwith natural forcing only, *Wu et al.* [2005] concluded that the observed increase in river runoff is mainly driven by anthropogenic influence. This is confirmed by a recent data assimilation and model study (*Gerten et al.*, 2008).

From the modeled freshwater flux to the ocean it is shown that the hydrological cycle can intensify in a warming climate without increase in total global precipitation. The freshwater flux is projected to increase stronger in the high northern compared to southern high latitudes. This is dominated by the runoff in the Northern Hemisphere. In the southern high latitudes precipitation is projected to gain more importance. Another model study found the variability of the freshwater flux to the ocean surface to be dominated by the thermodynamic growth of sea ice (*Köberle and Gerdes*, 2006). Based on this, they argue that maxima and minima in Arctic Ocean freshwater content are controlled by the export rate through the different straits which easily can be altered by an anomalous contribution from sea ice meltwater. On a global scale, oceanic freshening and cooling in the second half of the 20th century is reported for both polar regions while tropics and subtropics show a trend towards warmer and more saline waters (*Curry et al.*, 2003, *Boyer et al.*, 2005). Between 1965-2000 a freshening was observed in the North Atlantic, which is attributed to an anomalous export of freshwater from the Arctic region where the freshwater content has been building up over time (*Peterson et al.*, 2006).

The question if this anomalous export was triggered by atmospheric circulation modes rather than by a change in the Atlantic MOC cannot be answered with certainty. However, it is concluded that atmospheric modes are primarily responsible. From that, *Peterson et al.* [2006] propose the possibility of a trajectory shift occuring in the future as a response to the continuation of the building up of the freshwater storage in the Arctic region: as the NAO and the Northern Annular Mode (*Thompson and Wallace*, 2001) pass into a high mode again, the Arctic freshwater excess may be exported to the North Atlantic within comparably short time. A model study using the IPCC SRES A1B scenario found the Arctic Ocean freshwater budgets to be already in the midst of large changes with an increasing net freshwater export from the Arctic region to the North Atlantic as its prominent feature (*Holland et al.*, 2006). The detailed mechanism regulating the variability of the liquid freshwater export from the Arctic region is still subject to research, whereas it is confirmed that the freshwater export through the Fram Strait and the Canadian Arctic Archipelago (CAA) indirectly responds to changes in the atmospheric forcing (*Jahn et al.*, 2009).

Based on the globally asymmetric anomaly of freshwater flux in the future found by *Wu et al.* [2005], *Stocker and Raible* [2005] point out the possibility of a net transfer of freshwater from the Southern to the Northern Hemisphere. It is stated that such a transfer, if long-lasting, might modify the balance of deep water formation in both polar regions and that future model studies have to assess the probability and reversibility of such events. Numerous studies address the question of the stationarity and stability of the THC (e.g., *Stocker and*

Schmittner, 1997, *Schmittner and Stocker*, 1999) and possible consequences from a slow-down of the circulation (e.g., *Rahmstorf*, 1995, *Vellinga and Wood*, 2002), whereby a consensus is detectable on the importance of the freshwater flux for the stratification and stability of the ocean.

In fact, measurements of a decreasing overflow from the Nordic Seas into the North Atlantic through the Faroe Bank Channel during the last decades lead to the conjecture that the Atlantic MOC is weakening already (*Hansen et al.*, 2001). Observations also show a freshening of the deep sub-polar North Atlantic Ocean since the 1970's (*Dickson et al.*, 2002), which would be a commonly expected signal accompanying a weakening Atlantic MOC. However, a model study over the same time period did not find a weakening of the MOC (*Wu and Rodwell*, 2004) and failed to attribute the freshening in the second half of the 20^{th} century to anthropogenic climate change (*Wu et al.*, 2007). They mentioned natural external forcing as the potential triggering cause, yet, the underlying physical mechanism is not understood. A 16-year measurement time series of the northward flow along the east cost of Florida does not show a significant trend (*Baringer and Larsen*, 2001). Using the newly deployed Rapid Climate Change mooring array at 26.5° N *Cunningham et al.* [2007] estimated the year-long Atlantic MOC to be 18.7 ± 5.6 Sv (1 Sverdrup = $10^6 \text{m}^3\text{s}^{-1}$) with a large annual range of about 30 Sv (from 4.0 to 34.9 Sv). They demonstrated the limitations to detect past changes in the Atlantic MOC from sparsely distributed moorings and emphasized the need of a ten-year time series from this new mooring array.

A recent model study analysing the 20^{th} century Arctic freshwater budget found an increased liquid freshwater export from the Arctic Ocean to the North Atlantic to reduce the simulated MOC by lowering surface salinity in regions of deep water formation (*Jahn et al.*, 2009). Thereby, 20% of the variance of the MOC could be explained by the variability of the freshwater export to the Greenland-Iceland-Norwegian (GIN) Seas. *Bryan et al.* [2006] investigated the response of the North Atlantic MOC to a prescribed climate forcing of 1% increase in CO_2 concentration per year, using a coupled general circulation model. They found the Atlantic MOC to decrease at a rate of 22%-26% per century compared to a control simulation and located the decreasing density of the sub-polar North Atlantic as a cause. However, and in contrast to some of the above mentioned studies, *Bryan et al.* [2006] explain the decreasing density in the sub-polar North Atlantic by increased surface heat flux rather than by increased surface freshwater influx. Surface freshwater influx was revealed to actually increase the density of the water masses involved in deep water formation and hence maintain the MOC. *Holland et al.* [2006] ended up with a similar conclusion when simulating the freshwater budgets of the Arctic Ocean, the Nordic seas and Labrador Sea. As the sea ice export through the Fram Strait decreases in the future the GIN Seas lose their main contributor of freshwater. This will increase the surface salinity there and help maintain the deep water formation. On the other hand, the Labrador Sea is expected to continuously freshen due to increasing freshwater influx. Despite the fact that the largest freshening does not occur in the region of the deep water formation site, overall Labrador Sea ventilation and mixed layer depth are expected to decrease and therefore reduce deep water formation (*Holland et al.*, 2006).

Regarding the deep water formation in the Southern Hemisphere, causes for and implications of a reduction have been discussed for some time (e.g., *Broecker et al.*, 1999, *Brix*

and Gerdes, 2003). Further, the interplay of the two hemispheres in terms of deep water formation has been debated controversly. In a model study the Southern Hemisphere deep water formation sites were found to be sensitive to changes in the Antarctic Circumpolar Current (ACC) which itself can be weakened by an enhanced deep water formation in the Northern Hemisphere (*Brix and Gerdes*, 2003). However, *Brix and Gerdes* [2003] emphasize that this inter-hemispheric connection is not regarded as a fully understood mechanism and that the deep water formation sites of the two hemispheres can also show a synchronized behaviour under different forcing parameters. *Hattermann and Levermann* [2010] simulated the response of the Antarctic ice shelf and the ACC to an experimental 1% CO_2 increase per year. Along with a freshening due to increased sea ice meltwater influx the ACC weakens and the formation of Antarctic Atlantic Bottom Water (AABW) is reduced. After 150 years the ACC strengthens again due to an increasing meridional temperature gradient in the ocean, accentuating the need for long-term simulations when assessing oceanic climate change in the Southern Hemisphere. A recent study shows that a reduced production of AABW can restrain a weakening of the Atlantic MOC, exemplifying the diversity of effects of the bi-polar seesaw (*Swingedouw et al.*, 2008).

As can be seen from this selection of findings the scientific community still struggles to draw a consistent picture of the ongoing and possible future changes of the freshwater cycle in polar regions and their consequences since many complex processes are involved and observational data are limited in temporal and spatial terms.

1.3 Geographical characteristics of the Arctic and Antarctic region

As a response to the continuous rise of global SAT (0.6 ± 0.2°C over the 20^{th} century), an intensification of the hydrological cycle is expected. The SAT is projected to increase strongest in the northern high latitudes with regional anomalies of more than 7°C by the end of the 21^{st} century (*IPCC*, 2007). Fig. 1.2 shows the SAT of the regions 60-90° N and 60-90° S as they are simulated by this study's model. It becomes clear, that the Antarctic region is expected to warm at a slower rate compared to the Arctic region.

As mentioned in section 1.2 the main source of freshwater for the Arctic Ocean comes from river runoff. Fig. 1.3 shows the catchement areas around the Arctic Ocean which are about 1.5 times the area of the Arctic Ocean itself and thereby make the Arctic Ocean the most land-dominated of Earth's ocean basins (*Peterson et al.*, 2002). Eurasian and North-American rivers carry water from as far south as 45° N to the Arctic Ocean. The Eurasian rivers dominate the total runoff budget and contribute over 70% to annual runoff.

Besides the unusual dominance by river runoff the Arctic Ocean basin features a very complex bathymetry. Fig. 1.4 shows the bathymetry of both polar regions used by this study's model. The coastal areas in large parts of the northern high latitudes (Fig. 1.4 (a)) are characterized by a distinct and very shallow shelf; its development dates back to past glacial maxima when the sea level was significantly lower. In contrast, depths of over 3,000 meters are found in the middle of the Arctic Ocean and also in the GIN Seas. It is this particular shape of the basin that also plays a key role in controlling the freshwater cycle and budget of the Arctic

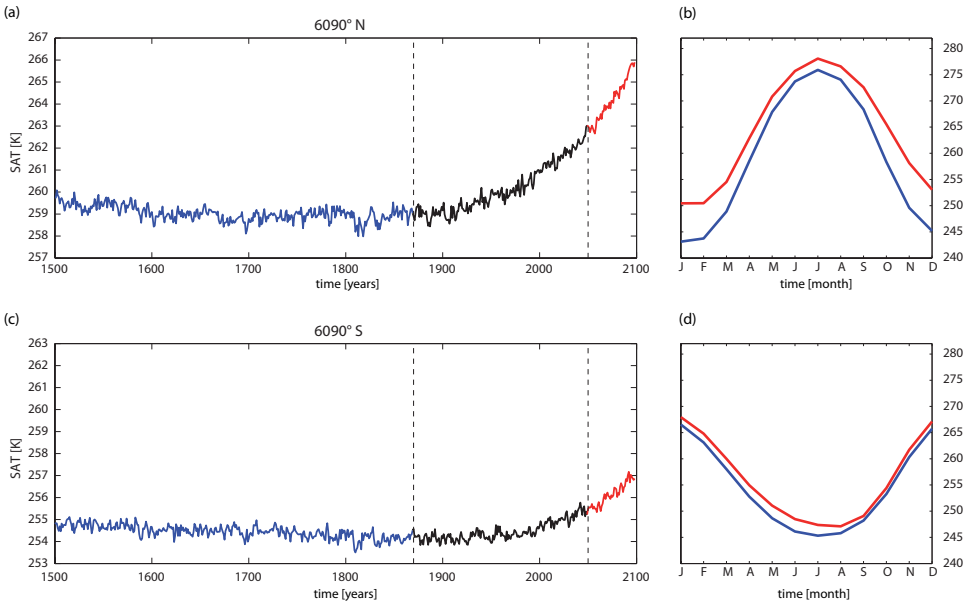

Figure 1.2: Ensemble mean surface air temperature (SAT) at 60°-90° N and 60°-90° S. Annual means are given in colours corresponding to different time periods in (a) and (c). The average annual cycle for the period 1500-1870 and 2050-2098 is given in the corresponding colours (b) and (d). Note that the y-axis in (a) and (c) are different but span the same range.

region. As the freshwater is accumulating in the Arctic Ocean, the discharge possibilities are limited to the narrow Fram Strait and the CAA (Fig. 1.5) and make these regions important regulators of the freshwater cycle. For further details see, e.g., *NATO* [2000].

The geographical setting in the southern high latitudes is profoundly different from the one in the Northern Hemisphere. Only a small shelf band surrounds Antarctica and depths are generally greater. Therefore, no single-basin structure exists and exchange of freshwater from sea ice meltwater and continental runoff with surrounding oceans can take place unhampered. A gradual accumulation of freshwater as it is happening in the Arctic Ocean is therefore unlikely to occur in the Southern Ocean. Nevertheless, these regions are sensible to anomalous freshwater influx too as the Weddell and Ross Seas are regions of deep-water formation where water masses subside and flow northward as AABW.

Figure 1.3: Map of the pan-arctic total watershed, showing catchments of major Eurasian rivers and their average annual discharge. The numbers for the Eurasian rivers are from *Peterson et al.* [2002]. Note, that the sketched catchment of the North-American continent comprises all rivers, while the numbers are for the Mackenzie and Yukon only (taken from *ACIA*, 2004).

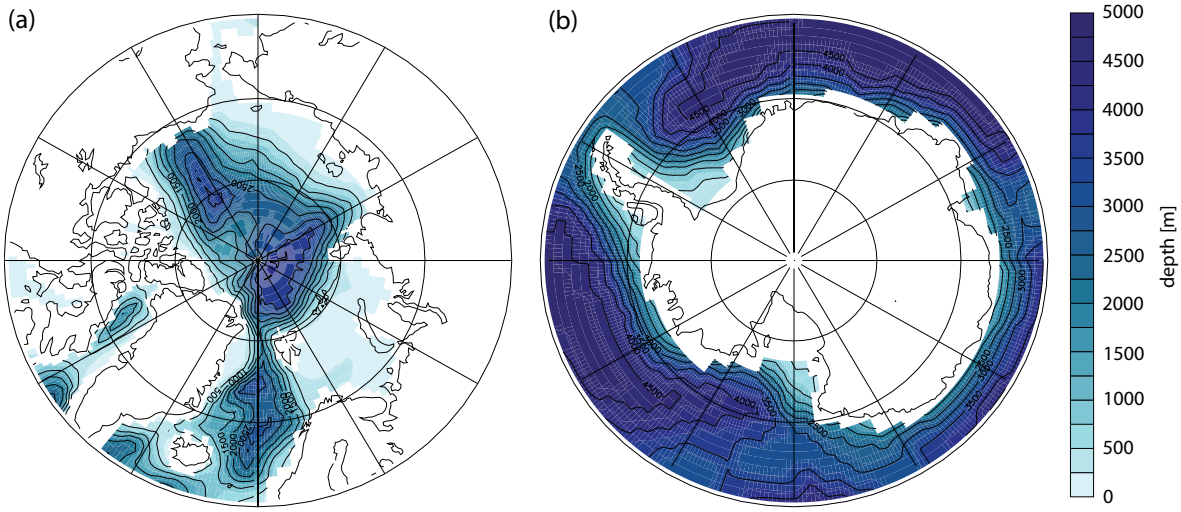

Figure 1.4: The ocean bathymetry as it is represented in this study's model for 60-90° N (a) and 60-90° S (b). Contour intervals are 500 meters.

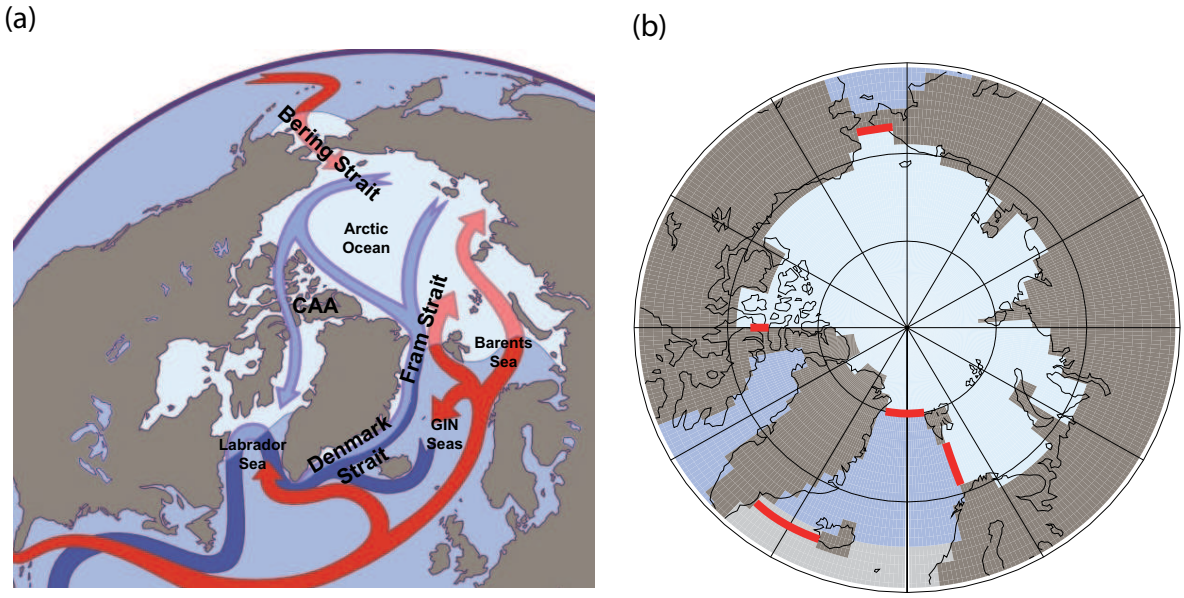

Figure 1.5: Simplified scheme of the ocean currents in the Arctic region with cold currents (blue) and warm currents (red)(a), (source: modified from http://nsidc.org/arcticmet/factors/land_sea_distribution.html [16.08.2009]). The different passages delimiting the Arctic Ocean as they are reproduced on the regridded stereographic map and used in section 3.3 (b). Note that the CAA and the Bering Strait seem to be closed on this projection, however, on the actual model grid, both passages are open.

1.4 Objectives

The objectives of this study are to examine the freshwater budget and cycle of the polar regions under changing climate conditions. The temporal restriction is from 1500-2100 and the tool of choice is a state-of-the-art coupled general circulation model. As there are still some uncertainties about observed and simulated freshwater fluxes in and out of the polar regions, evaluating the model with respect to simulated freshwater fluxes is a first task. Beyond the instrumental period (both past and future) the sensitivity of the freshwater budget and its components to changing forcing parameters such as volcanoes, solar activity and greenhouse gas concentrations is assessed. Regarding the different freshwater flux terms, river runoff and the export paths of freshwater from the polar regions are of special interest as they are considered to play a key role in controlling polar freshwater budgets. Thereby, emphasis is put on changes in the 21st century as they are expected to be substantially larger than what is know from fluctuations during the past 500 years. Furtheron, possible implications of a changing freshwater export from the Arctic regions for the Atlantic MOC is addressed as this is a research area of increasing interest and activity.

Chapter 2

Model and experimental design

The data used in this study were generated by a state-of-the-art coupled climate model. This chapter provides a brief overview on this model and its components. The implementation of the river runoff in the model is discussed in more detail, as this quantity is of particular importance to this study. Further on, the experimental setting is presented as well as some remarks on the methods applied.

2.1 Model description

The model used for the simulations is the Community Climate System Model version 3.0.1 (CCSM3), which was developed by the National Center for Atmospheric Research (NCAR) (*Collins et al.*, 2006). It was released to the climate community in June 2004 and was used at its highest resolution in the IPCC AR4 in 2007. At the present state the model consists of four components for the atmosphere, ocean, sea ice, and land surface, all linked through a coupler (the CCSM Coupler Version 6.0) which exchanges fluxes (without flux corrections) and state information. It is available in different resolutions: the low-resolution version, referred to as T31x3, has an atmospheric and terrestrial grid spacing of about 3.75° and a nominal ocean and sea ice resolution of about 3°×3°. The intermediate-resolution version (T42x1) has an approximate 2.8° spacing for the atmosphere and land component and a nominal 1° ocean and sea ice resolution. The high-resolution version (T85x1), finally, shares the same ocean and sea ice component spacing as T42x1, but has a higher atmospheric and terrestrial resolution of about 1.4°×1.4°.

2.1.1 Model components

The atmospheric component is the Community Atmosphere Model in version 3.1 (CAM3), which is based on the primitive equations. The model has an Eulerian spectral dynamical core and applies a triangular spectral truncation at 31 wavenumbers (T31). This corresponds to a latitudinal and longitudinal resolution of approximately 3.75° × 3.75°(96 longitudes, 48 latitudes). The vertical dimension is discretized on a hybrid coordinate system with finite-differences. It is differentiated into 26 unevenly spaced sigma-pressure levels between the surface and 2.9 hPa. The transition from a pure (terrain-following) sigma level at the ground

to a pure pressure level is located above about 83 hPa. Time-stepping is performed with a semi-implicit leapfrog scheme.

The land surface model is called Community Land Model (CLM3) and shares the same horizontal resolution on a Gaussian grid as the CAM3, although each grid box is further divided into a hierarchy of land units (including glaciers, lakes, wetlands, urban areas, and vegetated regions), soil columns, and up to 16 different vegetation types. In the vertical there are ten sub-surface soil layers, in which temperature and moisture (water and/or ice) are calculated. Further on, up to five thickness-dependent snow layers can be associated to a grid box of the land component. The CLM interacts with the River Transport Model, a 2-dimensional model on an independent grid, which simulates the horizontal transport of water in the CLM (see section 2.1.3).

The ocean component in the CCSM3 is represented by the Parallel Ocean Program version 1.4.3 (POP), a primitive equation model developed at the Los Alamos National Laboratory. The finite-differences method is employed to discretize onto a dipole grid with latitudinal resolution of 3°. The longitudinal resolution varies in space (max. refinement in the Tropics is 0.9°, model average 1.8°) to better refine certain areas. The grid covers 100 longitudes and 116 latitudes. The numerical poles of the grid are located in Antarctica at the true South Pole and in the Northern Hemisphere in central Greenland (77.36°N/39.18°E). By setting the numerical North Pole on an adjacent land mass (such as Greenland) the Arctic Ocean can be covered by a singularity-free grid. The model also allows for an open Bering Strait and the inclusion of a single opening through the CAA. At the Equator this displaced-pole grid joins smoothly with the standard Mercator grid of the Southern Hemisphere. The vertical resolution covers 25 unevenly spaced levels, adding up to a depth of 4,750m at the maximum (5 levels for the top 100 m, 13 for the top 1,000 m). The 1° version of the POP covers 40 levels, extending to 5,370m (not used in this study).

The Community Sea Ice Model version 5.0 (CSIM5) serves as the sea ice component in CCSM3 and is discretized with the same horizontal resolution as the POP. It computes multi-category ice thickness distribution (five categories) and employs the elastic-viscous-plastic ice rheology. It includes energy-conserving thermodynamics.

More detailed descriptions of the model components are available at the NCAR CCSM webpage (http://www.ccsm.ucar.edu/models).

2.1.2 Climate and hydrological sensitivity

The climate sensitivity of the CCSM3 is defined as the simulated change in equilibrium global-mean surface temperature (ΔT_{eq}) due to a doubling of atmospheric CO_2. A study by *Kiehl et al.* [2006] reveals that the climate sensitivity of the CCSM3 explicitly depends on the model resolution and yields 2.32, 2.47 and 2.71°for the resolution T31x3, T42x1 and T85x1, respectively. Thereby the CCSM3 is at the lower end of the range of climate sensitivity estimated by the IPCC, which states: "[...] equilibrium climate sensitivity is likely to be in the range 2°C to 4.5°C with a best estimate of about 3°C . It is very unlikely to be less than 1.5°C . Values substantially higher than 4.5°C cannot be excluded, but agreement of models

with observations is not as good for those values. [...]" (*IPCC*, 2007).

The hydrological sensitivity of the CCSM3 is determined as the change in the global mean rate of precipitation at doubling of CO_2 (reached by a continuous CO_2 increase rate of 1% yr^{-1}), which is 1.7 (T31x3), 1.6 (T42x1) and 1.8 % $^{\circ}C^{-1}$ (T85x1) (*Kiehl et al.*, 2006). Reasons for the differences among the three resolutions of the CCSM3 are the inefficient vertical mixing of water vapour with increasing atmospheric resolution (which results in an underestimation of low clouds) and the overestimation of sea ice (especially in the T31x3 resolution).

2.1.3 River runoff

Reasonable runoff flux values are crucial for the modeled ocean circulation and convection in the POP. Therefore, a sophisticated hydrological cycle is implemented in the CCSM3. In order to be able to close this hydrological cycle the CLM needs to route the surface runoff either to the active ocean or a marginal sea. How much of the incoming precipitation, snow melt, and canopy water flows off as surface runoff or sub-surface drainage is determined by a separate submodel. The River Transport Model specifically deals with the process of routing and transporting of surface runoff. The calculated quantities are then assigned to the POP via the coupler, whereby interpolating, weighting, and smoothing measures are taken into account.

Land surface runoff

The CAM3 provides different types of precipitation, which are bundled and passed to the CLM by the coupler. To calculate and parameterize runoff within the CLM the steady state theory for downslope saturated zone flows of the TOPMODEL (a TOPography based hydrological MODEL, *Beven and Kirkby*, 1979) is used. This theory includes the assumption that the local hydraulic gradient is equal to the local surface slope. Following this, a topographic index

$$I = \frac{a}{\tan B}, \tag{2.1}$$

where a is the drained area per unit contour length and $\tan B$, the slope of the ground surface at the location, can be calculated for all grid points with equal hydraulic properties.
The soil profile is defined by a set of layers, for which a water table level is calculated. From that saturated and unsaturated fractions are derived for every layer. Following *Beven and Kirkby* [1979] the saturated fraction f_{sat} decreases exponential with depth and is given by

$$f_{sat} = w_{fact} \min\left[1, \exp(-z_w)\right], \tag{2.2}$$

where $w_{fact} = 0.3$ is a parameter determined by the distribution of the topographic index. z_w is the mean water table depth (dimensionless)

$$z_w = f_z \left(z_{h,10} - \sum_{i=1}^{10} s_i \Delta z_i \right), \tag{2.3}$$

where $f_z = 1\ \mathrm{m}^{-1}$ is a water table scale parameter, $z_{h,10}$ is the bottom depth of the lowest (10th) soil layer (which is about 3.44 m) s_i is the soil wetness for layer i, and Δz_i is the soil layer thickness in m. The soil wetness s_i is

$$s_i = \frac{\theta_{ice,i} + \theta_{liq,i}}{\theta_{sat,i}} \leq 1, \tag{2.4}$$

where $\theta_{sat,i}$ is the saturated volumetric water content and $\theta_{ice,i}$ and $\theta_{liq,i}$ are the volumetric ice and liquid water contents:

$$\theta_{ice,i} = \frac{w_{ice,i}}{\Delta z_i \rho_{ice}} \leq \theta_{sat,i}, \tag{2.5}$$

$$\theta_{liq,i} = \frac{w_{liq,i}}{\Delta z_i \rho_{liq}} \leq \theta_{sat,i} - \theta_{ice,i}. \tag{2.6}$$

ρ_{ice} and ρ_{liq} are the density of ice and liquid water (917 and 1,000 kg m^{-3}, respectively). The unsaturated fraction is $1-f_{sat}$.
The top soil layer is considered impermeable when $\theta_{sat,1} - \theta_{ice,1} \leq \theta_{imp}$ (with $\theta_{imp} = 0.05$ being the water-impermeable volumetric water content). Given this, all water reaching the soil surface runs off:

$$q_{over} = q_{liq,0} \tag{2.7}$$

where $q_{liq,0}$ is any liquid precipitation reaching the ground plus melt water from an eventually overlying snow pack. If the top soil layer is not impermeable, the surface runoff consists of the runoff from saturated and unsaturated areas:

$$q_{over} = f_{sat}\, q_{liq,0} + (1 - f_{sat})\, \overline{w}_s^4\, q_{liq,0} \tag{2.8}$$

with $\overline{w}_s$ being the soil layer thickness weighted wetness in the top three layers

$$\overline{w}_s = \frac{\sum_{i=1}^{3} s_i \Delta z_i}{\sum_{i=1}^{3} \Delta z_i}. \tag{2.9}$$

This way, a surface water balance is calculated for every grid box.

Besides the surface runoff the sub-surface drainage also contributes to the water flux which later on is delivered to the River Transport Model. Sub-surface drainage (mm s^{-1}) is the sum of lateral drainage from soil layers 6-9 and drainage out of the bottom of every soil column plus any adjustments necessary to keep the liquid water content of each layer between defined maximum and minimum values:

$$q_{drain} = q_{drain,wet} + q_{drain,dry} + \frac{w_{liq}^{excess}}{\Delta t} - \frac{w_{liq}^{deficit}}{\Delta t} + k[z_{h,10}] + \frac{\partial k[z_{h,10}]}{\partial \theta_{liq,10}}\, \theta_{liq,10} \tag{2.10}$$

where $q_{drain,wet}$ and $q_{drain,dry}$ are the lateral drainage from the saturated and unsaturated layers, respectively, w_{liq}^{excess} is the amount of liquid water in excess of saturation in all layers,

$w_{liq}^{deficit}$ is the amount of liquid water required to prevent any soil layer from having negative liquid water content, $k[z_{h,10}]$ is the bottom drainage (10th layer) and $\frac{\partial k[z_{h,10}]}{\partial \theta_{liq,10}} \theta_{liq,10}$ is the change in hydraulic conductivity due to the change in liquid water content of the bottom layer.

This desciption is based on *Oleson et al.* [2004], where more details are presented. Note that there are special terms for surface runoff and drainage from glaciers, wetlands and snow-capped surfaces, which may lead to negative runoff values in some cases (this signal may even be transported downslope, resulting in a negative runoff flux to the ocean). For a description of these terms and the equations governing the snow layers, soil water content and infiltration processes, see *Oleson et al.* [2004], chapter 7.

Including all processes the total runoff in the CLM is

$$R = q_{over} + q_{drain} + q_{rgwl} \tag{2.11}$$

with q_{rgwl} being the runoff from glaciers, wetlands and lakes.

River Transport Model (RTM)

The RTM operates on a $0.5^\circ \times 0.5^\circ$ grid, and thus has a higher resolution than the CLM. The interaction between the CLM and the RTM is schematically illustrated in Fig. 2.1. The exchange is done by the coupler, which interpolates the surface runoff and drainage data from the CLM-grid to the RTM-grid. Due to computational constraints the RTM is run at a time step larger than the CLM which forces the coupler to accumulate the fluxes from the CLM until the RTM is invoked. As indicated in Fig. 2.1 the water storage of a RTM grid cell consists of the cell-internal surface runoff ("Overland Flow"), retention by lakes, wetlands or glaciers ("Return Flow") and sub-surface drainage ("Drainage") and the external upstream inflow from and downstream outflow to a neighboring RTM grid cell.

The phenomenon of negative runoff values as mentioned in the previous section is exemplified in Fig. 2.2, which shows a one month-average of the river flow and the corresponding discharge into the ocean produced by the RTM as well as a 10 year average of river runoff. In the 10 year average nearly no negative values are found limiting the phenomena to seasonal variability of glacier and wetland drainage.

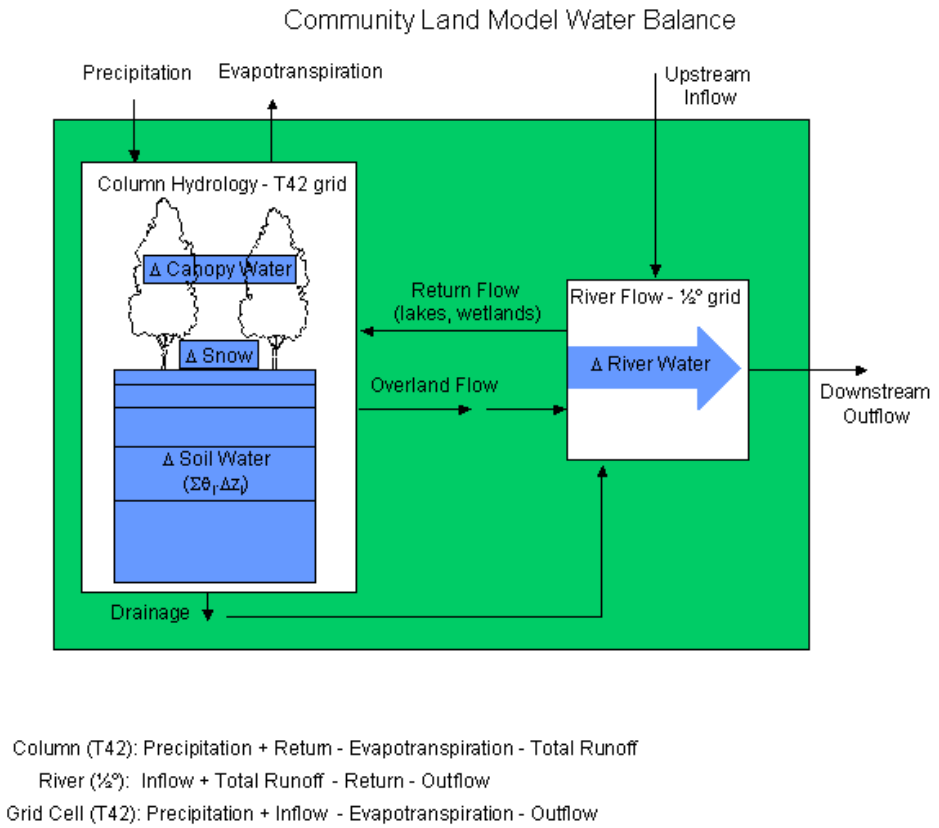

Figure 2.1: CLM RTM flow chart (source: http://www.cgd.ucar.edu/tss/clm/rtm/waterbalance.gif [20.01.2009]).

The storage S of river water within a RTM grid cell can therefore be summarized as

$$\frac{dS}{dt} = \sum F_{in} - F_{out} + R \tag{2.12}$$

where $\sum F_{in}$ denotes the sum of inflows of water from neighbouring upstream grid cells, F_{out} is the water flux leaving the grid cell and R is the total runoff generated by the CLM. The downstream flow direction in each RTM grid cell is defined as one of eight compass points or directions (north, northeast, east, southeast, south, southwest, west, and northwest) determined by the steepest downhill slope (*Graham et al.*, 1999). The elevation information is taken from the digital elevation model TerrainBase (*Row et al.*, 1995). The water flux F_{out} is

$$F_{out} = \frac{v}{d} \cdot S \tag{2.13}$$

where v is the effective water flow velocity ($v = 0.35\ \mathrm{ms}^{-1}$, globally constant), d is the distance between centres of neighbouring grid cells (varying latitudinally) and S is the volume of stored river water (m^3). The RTM distinguishes ocean and land grid cells by a simple if-clause, checking if the predefined river direction is 0 (= ocean cell) or one of the eight possible directions (= land cell). All cells that have been identified as ocean cells are then checked for

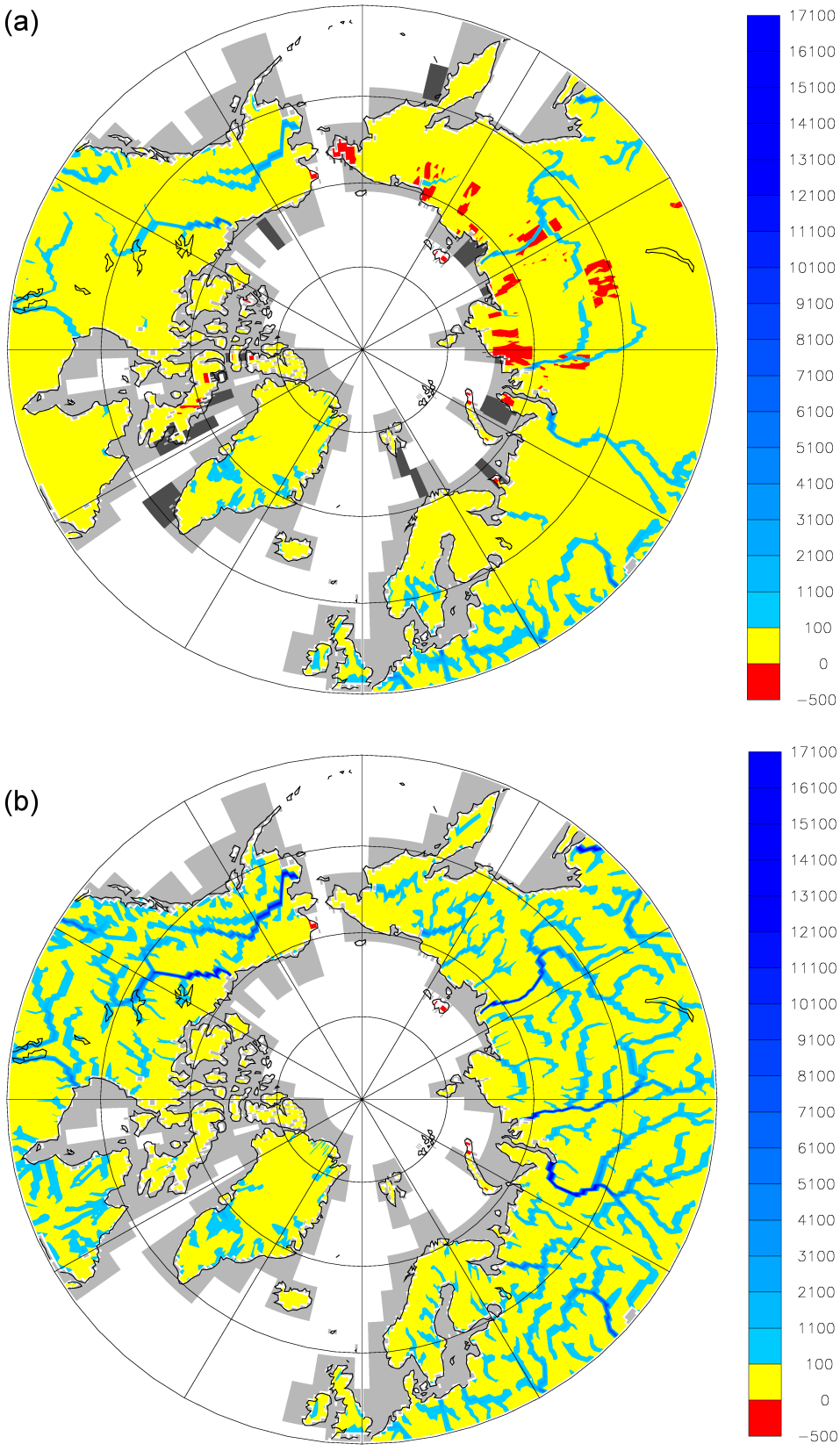

Figure 2.2: Monthly mean of RTM river flow (legend in m^3/s) and RTM river discharge into ocean (black boxes = negative discharge, light gray boxes = positive discharge) for January 2011 (a) and an average from 2011 to 2021 (b). Red areas on land denote glaciers or wetlands where negative river flow values are possible.

their adjacent eight cells if any of them has a predefined direction that points into that ocean cell, thereby defining them as ocean cells that sit on a river mouth and potentially receive river runoff. The calculated runoff is passed to the ocean cells still within the RTM applying no interpolation or weighting (*Kauffmann et al.*, 2004).

The river-routing scheme conserves river water globally as

$$\sum_{i,j} \left(\frac{dS}{dt} \right)_{i,j} = \sum_{i,j} R_{i,j} \tag{2.14}$$

where i and j are the grid cell indices.

Runoff flux to the ocean

The runoff calculated by the RTM is delivered to the POP via the coupler. Since the RTM and POP do not share the same grid, the data have to be remapped during this transfer. For flux data the CCSM coupler applies a second-order conservative remapping scheme using the Spherical Coordinate Remapping and Interpolation Package SCRIP provided by the Los Alamos National Laboratory (*Jones*, 1999, *Jones*, 2001) where the flux F at the destination grid cell k (destination grid = POP grid) is defined as

$$\overline{F}_k = \frac{1}{A_k} \sum_{n=1}^{N} \int \int_{A_{nk}} f_n dA, \tag{2.15}$$

where $\overline{F}$ is the area-averaged flux, A_k is the area of the destination grid cell k, A is the area of the source grid cell n (source grid = RTM grid), N is the number of source grid cells overlapped by k, A_{nk} is the area of the source grid cell covered by k and f_n is the local value of the flux in the source grid cell obtained by using

$$f_n = \overline{f}_n + \nabla_n f \cdot (\vec{r} - \vec{r_n}) \tag{2.16}$$

with $\nabla_n f$ being the gradient of the flux in cell n and $\vec{r_n}$ being the centroid of cell n defined by

$$\vec{r_n} = \frac{1}{A_n} \int \int_{A_n} \vec{r} dA. \tag{2.17}$$

Transformed into spherical coordinates, equation (2.15) yields

$$\overline{F}_k = \sum_{n=1}^{N} \left[\overline{f}_n w_{1nk} + \left(\frac{\partial f}{\partial \theta} \right)_n w_{2nk} + \left(\frac{1}{\cos\theta} \frac{\partial f}{\partial \phi} \right)_n w_{3nk} \right], \tag{2.18}$$

where θ is the new latitude, ϕ is the new longitude. The three remapping weights are defined by

$$w_{1nk} = \frac{1}{A_k} \int\int_{A_{nk}} dA, \tag{2.19}$$

$$w_{2nk} = \frac{1}{A_k} \int\int_{A_{nk}} (\theta - \theta_n) dA$$

$$= \frac{1}{A_k} \int\int_{A_{nk}} dA - \frac{w_{1nk}}{A_n} \int\int_{A_n} \theta dA, \tag{2.20}$$

$$w_{3nk} = \frac{1}{A_k} \int\int_{A_{nk}} \cos\theta(\phi - \phi_n) dA$$

$$= \frac{1}{A_k} \int\int_{A_{nk}} \phi \cos\theta dA - \frac{w_{1nk}}{A_n} \int\int_{A_n} \phi \cos\theta dA, \tag{2.21}$$

where θ_n is the latitude of the source grid cell, ϕ_n is the longitude of the source grid cell. The area integrals in equations (2.19) – (2.21) are actually calculated as line integrals: SCRIP first integrates around every source grid cell, where a search algorithm remembers intersections with destination grid lines. Secondly, it integrates around every destination grid cell in the same manner to obtain all overlapping regions of the two grids. Fig. 2.3 schematically illustrates the integration procedure with two different grids.

However, the SCRIP conservative remapping scheme does not guarantee the global conservation of a mapped quantity. SCRIP cannot take into account the destination grid's mask (e.g., which destination grid cells are land or ocean). Therefore a flux can be mapped into an inactive region of the destination grid and hence be lost to the quantity's global budget. Fig. 2.4 exhibits such a situation when remapping from RTM to the POP grid.

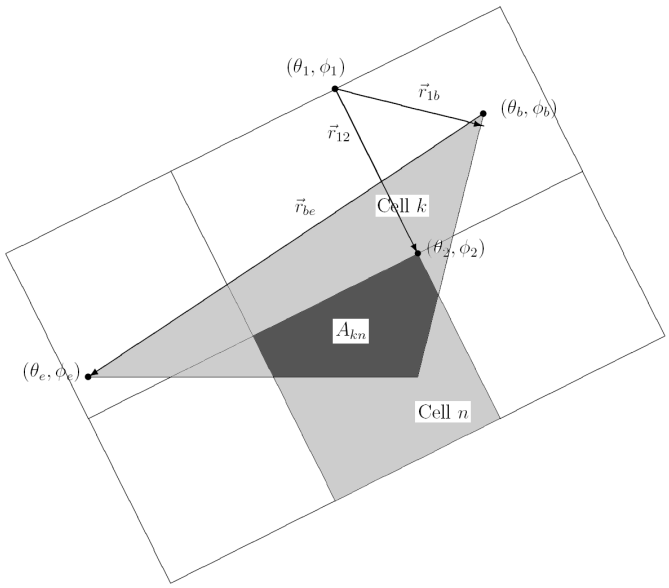

Figure 2.3: A triangular destination grid cell k overlaps a quadrilateral source grid with a specified cell n. The overlapping area is denoted A_{kn} (modified after *Jones*, 2001).

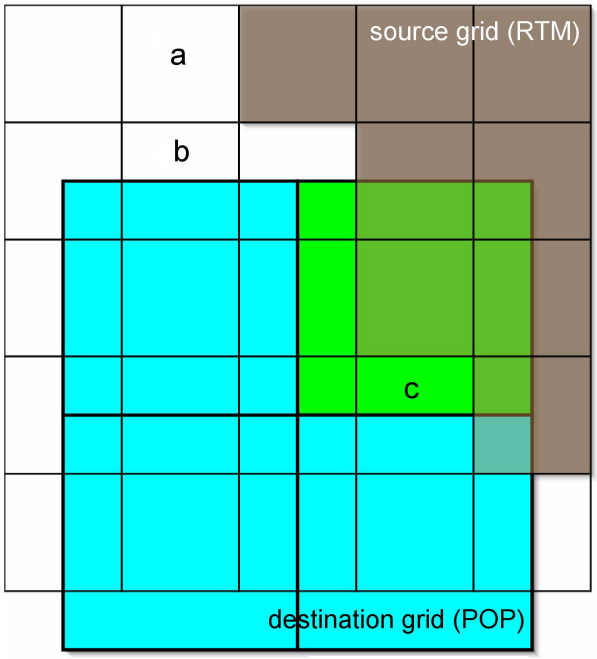

Figure 2.4: Overlapping cells between RTM and POP. White and gray boxes denote ocean and land cells of the RTM, respectively, turquoise and green boxes denote ocean and land cells of the POP, respectively. In the process of remapping, flux losses occur where an active source grid cell (containing river runoff) is not (a) or only partially (b) overlapped by a destination grid cell or where an active source grid cell maps into an inactive destination grid cell (c), i.e., a land cell of the ocean grid (source: www.ccsm.ucar.edu/csm/working_groups/Ocean/presentations/032030 [22.01.2009]).

To correct for such an imbalance a subroutine of the coupler's flux module calculates a scaling factor f for every timestep. For the communication of POP with CAM3 and RTM, respectively, it is defined as:

$$\begin{aligned} E + f(P + R) &= 0 \\ f &= -\frac{E}{(P + R)} \end{aligned} \tag{2.22}$$

where E, P and R are bundled evaporation, bundled precipitation and runoff, respectively. This guarantees that the net zero freshwater flux into the ocean is conserved. Values for f normally fluctuate between 0.75 and 1.25.

Finally, the problem of excessively low ocean salinities in regions of high runoff is addressed by applying a smoothing algorithm which divides the incoming runoff up on surrounding grid boxes.

2.2 Experimental design

For this and other studies (*Yoshimori et al.*, 2009) a series of model simulations were conducted. In this thesis we use the following two setups: a 1500 A.D. equilibrium simulation with perpetual 1500 conditions (hereafter EQ1500) and an ensemble of four transient forcing simulations (TR3, TR4, TR5 and TR6). The transient simulations are used, on the one hand, to calculate an ensemble mean which aims at filtering out or dampening very unlikely events, and on the other hand, to have a measure of the model spread and the uncertainty assigned to it. The EQ1500 simulation is initialized from a control simulation for perpetual 1990 A.D. condition. EQ1500 is used to provide different initial conditions for the four transient simulations. These transient simulations are forced with natural forcing from 1500 to 2000 and with the IPCC SRES A2 scenario further on until 2098. An overview of the simulations used in this study is given in Table 2.1.

In all four transient simulations (TR3 through TR6), time-varying external forcing induced by solar variability, volcanic eruptions and well-mixed greenhouse gases were applied. In Fig. 2.5 the five forcings are illustrated.

The greenhouse gas forcing consists of CO_2, CH_4 and N_2O and is based on ice core data from *Etheridge et al.* [1996], *Blunier et al.* [1995] and *Flückiger et al.* [1999] and *Flückiger et al.* [2002], respectively, all smoothed by a spline interpolation. The solar forcing is given by the total solar irradiance S (or solar constant). The net radiative forcing L_{net} was taken from *Crowley* [2000] and scaled to reconstructed data by *Lean and Bradley* [1995] using

$$S = 1365.0635\ \text{Wm}^{-2} + 5.399 \cdot L_{\text{net}}. \tag{2.23}$$

Under the A2 scenario the solar forcing is set constant at 1366.676 Wm^{-2} for 2001 onwards. The volcanic forcing in the model is defined by the total aerosol mass. Volcanic forcing estimates from *Crowley* [2000] are converted to total aerosol masses applying the linear regression between *Crowley* [2000] and *Ammann et al.* [2003] data for the six strongest volcanic eruptions in the last 130 years. As the data from *Crowley* [2000] focus on tropical eruptions, the calculated total aerosol masses are distributed throughout the lower stratosphere by weighting the aerosol masses by a latitudinal cosine function conserving the total mass. Due to the

Table 2.1: List of simulations

Simulation	Description	Length total	(years) used
EQ1500	1500 A.D. control simulations after spinup	653	599
TR3	Transient simulation with a time-varying forcing 1501-2000 and the A2 scenario 2001-2098, starting from year 21 of EQ1500	599	599
TR4	Same forcing as TR3 but with slightly different initial conditions: starting from year 41 of EQ1500	599	599
TR5	Same forcing as TR3 but with slightly different initial conditions: starting from year 32 of EQ1500	599	599
TR6	Same forcing as TR3 but with slightly different initial conditions: starting from year 43 of EQ1500	599	599

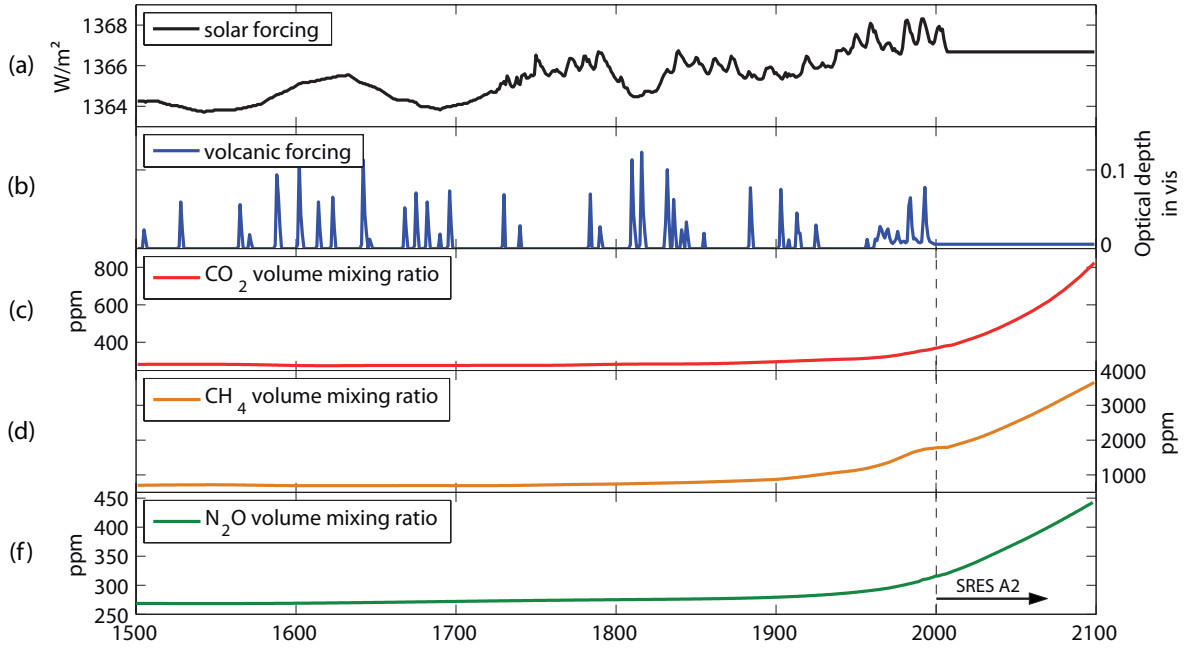

Figure 2.5: Natural and anthropogenic forcing used in the simulations: solar irradiance in W m^{-}2 (a), volcanic forcing as optical depth (b) and the volume mixing ratio in ppm of carbon dioxide (c), methane (d), and nitrous oxide (e).

fact that the exact date of eruption often remains unknown, the volcanic aerosols are added throughout the entire year of eruption. To illustrate the volcanic forcing Fig. 2.5 (b) shows the simulated total aerosol optical depth in the visible band. No artificial volcanic activity is simulated in the A2 scenario but the total aerosol optical depth is stabilized after 2000 at an estimated average value of 0.0054128 in the visible band.

The IPCC SRES includes 40 scenarios bundled into six scenario groups and four scenario families. The four families are based upon different narrative storylines for the 21st century along which demographic, social, economic, technological and environmental developments are estimated.

In the IPCC SRES the A2 scenario family is described as follows:
"The A2 storyline and scenario family describes a very heterogeneous world. The underlying theme is self-reliance and preservation of local identities. Fertility patterns across regions converge very slowly, which results in continuously increasing global population. Economic development is primarily regionally oriented and per capita economic growth and technological change are more fragmented and slower than in other storylines (*IPCC SRES*, 2000)."
Fig. 2.6 shows the projected global carbon dioxide emissions of the four scenario families. It can be seen that the A2 scenario family predicts, together with the A1F1, the strongest increase in carbon dioxide emissions. A new report (*Quéré et al.*, 2008) reveals the CO_2 emissions of the early 21st century to be slightly higher than the estimates from the A2 scenario. Note that the IPCC SRES presents multi-year averages and aims to show possible trends rather than precise predictions of the evolution of the emissions.

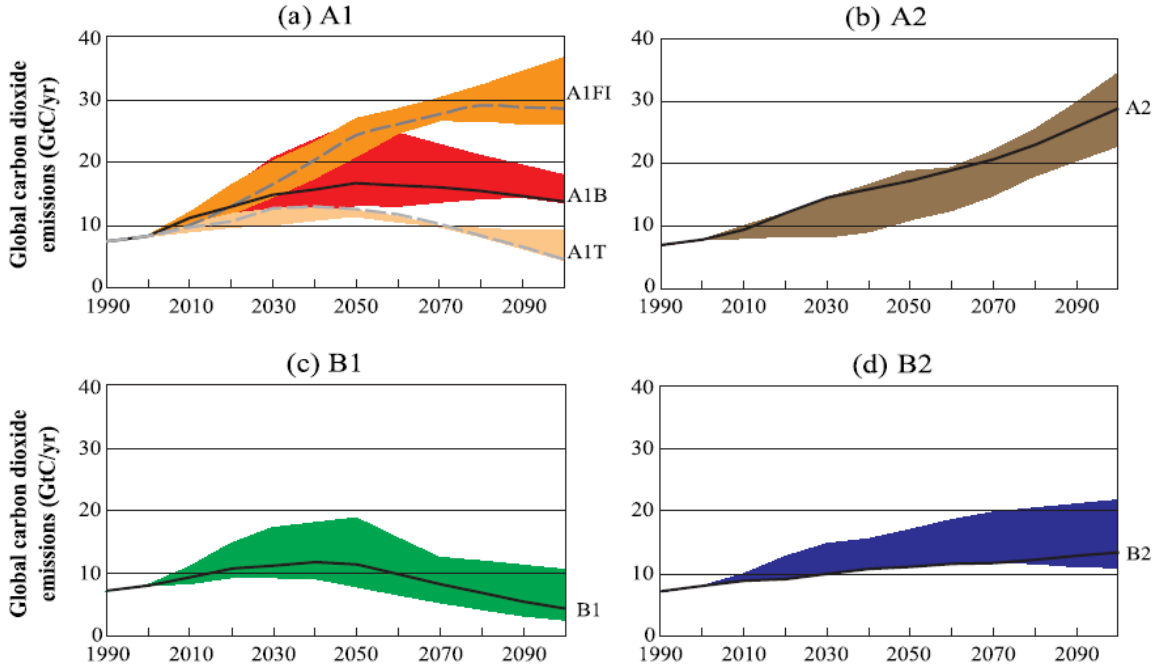

Figure 2.6: Total global annual CO_2 emissions in the four SRES scenario families (Figure from *IPCC SRES*, 2000). Coloured bands incdicate the range of the different scenarios within each family. The A1 family is characterized by a rapid and successful economic development with a convergence of regional average income per capita (a). This state can be achieved via three different paths of energy production: fossil-intensive (A1FI), balanced (A1B) and new technologies/predominantly non-fossil fuel (A1T). In the A2 family the global community exhibits a slow technology transfer between regions and therefore struggles in becoming more energy-efficient (b). The B1 family features a high level of environmental and social consciousness combined with a global approach towards sustainable development (c). The B2 family includes a higher awareness for environmental issues than the A2 family and projects a strengthening of local efforts towards sustainability rather than global attempts (d).

All simulations have a slight drift (as illustrated in Fig. 2.7 for global mean temperature of EQ1500) which needs to be corrected. The EQ1500 simulation (653 years model years) is used to detrend the four transient runs TR3 through TR6. Therefore, a linear trend is extracted from the EQ1500 simulation for every grid point. For the deep ocean data, a quadratic fit is used to determine the trend. This trend is then subtracted from every corresponding grid point in the data set of the four TR simulations.

2.3 Methods

2.3.1 Regridding

Since the ocean and sea ice components of the CCSM3 operate on a non-regular grid, their output has to be regridded (or remapped) onto a regular grid in order to be able to easily conduct operations along latitudinal or longitudial boundaries (e.g., calculate zonal means as in section 3.1.1). The NCAR Command Language (NCL) built-in function "PopLatLon" and the corresponding mapping weight file "map_gx3v5_to_1x1d_bilin_da_040122.nc" are used

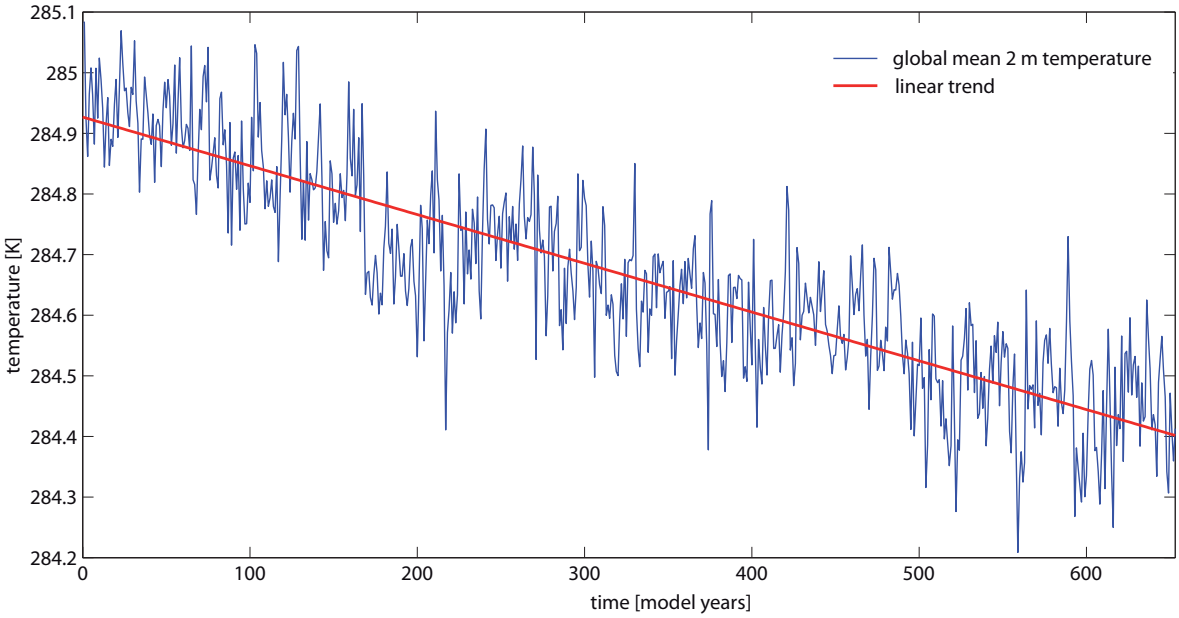

Figure 2.7: Global mean air temperature at two meters of EQ1500, annual means. The linear regression yields $T(t) = 8.04 \cdot 10^{-4}$ yr$^{-1} \cdot t + 285$ K and represents the model drift.

here to perform the regridding. This procedure of interpolating the data from one grid onto another inherits small errors, which are not addressed any further in this study. For a detailed description of the bilinear remapping scheme see *Jones* [2001].

2.3.2 Calculations

The fluxes as they are exchanged between different model components by the coupler are accessible as direct output variables (e.g. precipitation). Other fluxes and storage quantities used in this study have to be calculated manually from provided model output and are introduced here.

The atmospheric water vapour storage (kg m^{-2}) is calculated as

$$Q = -\frac{1}{g} \int_{p1}^{p26} q \, dp, \tag{2.24}$$

where g is the gravitational acceleration and q is the specific humidity. For the vertical integration on the hybrid grid of the atmospheric component a NCL built-in function is applied to scale from sigma to pressure coordinates and to obtain the pressure difference Δp between two overlying levels. The integration is then performed from $p1$ to $p26$, denoting the 26 vertical levels of the atmospheric component (surface to 2.9 hPa).

The meridional moisture transport (kg m^{-1} s^{-1}) is calculated as the vertically integrated convergence of the horizontal water vapour flux

$$\nabla Q = -\frac{1}{g}\int_{p1}^{p26} div\ (\vec{v}q)\ dp, \tag{2.25}$$

with div being the divergence of the horizontal water vapour flux

$$div\ (\vec{v}q) = \nabla_h \cdot F = \frac{\partial F_x}{\partial x} + \frac{\partial F_y}{\partial y}, \tag{2.26}$$

where F_x and F_y are given by uq and vq, respectively.

The meridional transport of sea ice at a certain latitudinal band is calculated on the original displaced-pole grid, implying that the grid boxes do not form a regular grid along latitudes and longitudes. Therefore, an interpolation is used to approximate the boundaries at 60° N and 60° S. First, the grid box closest to 60° N (and 60° S) is determined for every x-axes spacing. Second, the horizontal sea ice velocities u and v are weighted according to their distance to 60° N and 60° S, respectively. Third, the sea ice transport volume IT is calculated by including grid box average ice thickness h and grid box width w and length l. The latitude is given by ϕ. The indices y, x and i, j denote the u-grid (u and v) and t-grid (h) indices, respectively. The scheme is iterative and covers all 100 grid boxes in x-axes direction:

$$\begin{aligned} IT_{y,x} &= \left[\frac{v_1 \cdot |\frac{\phi_{y,x-1}+\phi_{y,x}}{2} - 60| + v_2 \cdot |\frac{\phi_{y-1,x-1}+\phi_{y-1,x}}{2} - 60|}{\frac{\phi_{y,x-1}+\phi_{y,x}}{2} + \frac{\phi_{y-1,x-1}+\phi_{y-1,x}}{2}} \cdot h_{i,j} \cdot w_{i,j}\right] \\ &+ \left[\frac{u_1 \cdot |\frac{\phi_{y,x}+\phi_{y-1,x}}{2} - 60| + u_2 \cdot |\frac{\phi_{y,x-1}+\phi_{y-1,x-1}}{2} - 60|}{\frac{\phi_{y,x}+\phi_{y-1,x}}{2} + \frac{\phi_{y,x-1}+\phi_{y-1,x-1}}{2}} \cdot h_{i,j} \cdot l_{i,j}\right] \end{aligned} \tag{2.27}$$

with the linearly weighted velocities

$$\begin{aligned} v_1 &= \frac{v_{y,x-1} + v_{y,x}}{2}, \\ v_2 &= \frac{v_{y-1,x-1} + v_{y-1,x}}{2}, \\ u_1 &= \frac{u_{y,x} + u_{y-1,x}}{2}, \\ u_2 &= \frac{u_{y,x-1} + u_{y-1,x-1}}{2}. \end{aligned} \tag{2.28}$$

Note that the second term in equation (2.27) represents the transport in grid x-direction and therefore drops out when the neighbouring grid box is also included in the calculation of the transport. This is achieved by a simple if-clause. Fig. 2.8 illustrates the two grids involved.

The liquid freshwater content of the ocean is computed as

$$FWC = \int\int_{z_{max}}^{z1} \frac{S_0 - S}{S_0}\ dz\ dA, \tag{2.29}$$

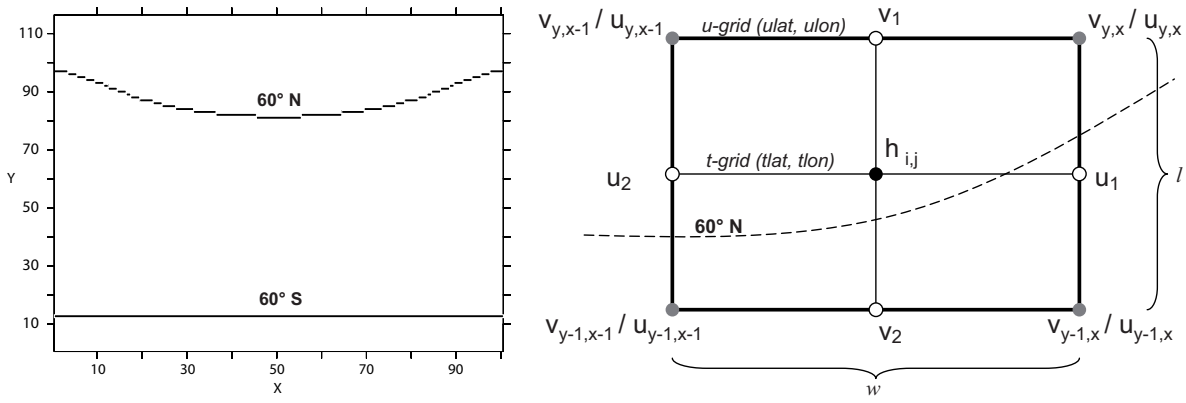

Figure 2.8: Grid boxes at 60° N and 60° S on the displaced-pole grid used for the calculation of sea ice transport (left) and the scheme used for interpolating the sea ice velocity vectors (right).

where z_{max} to $z1$ cover the maximum number of 25 vertical levels of the oceanic component, S_0 is the reference salinity of 34.7 g kg^{-1} and S the in-situ salinity.

The meridional oceanic freshwater transport FWT at a certain latitude is calculated as

$$FWT_t = (FWC_{t+1} - FWC_t) - (\frac{P_t + P_{t+1}}{2} - \frac{E_t + E_{t+1}}{2} + \frac{R_t + R_{t+1}}{2} + \frac{M_t + M_{t+1}}{2}) \quad (2.30)$$

with precipitation P, evaporation E, runoff R and sea ice meltwater M. Timestepping is given by the index t.

The freshwater transport FWT across a specified transect is computed as

$$FWT = \left[l \cdot \int_{z_{max}}^{z1} u \, \frac{(S_0 - S)}{S_0} \, dz \right] + \left[w \cdot \int_{z_{max}}^{z1} v \, \frac{(S_0 - S)}{S_0} \, dz \right], \quad (2.31)$$

where u and v are the horizontal velocities, w and l are the width and length of the grid box.

At some point in section 3.3 a normalized index is used to compare quantities with different unit scales. The normalized data is

$$z = \frac{x - \mu_x}{\sigma_x}, \quad (2.32)$$

where x is the original data, μ_x is the mean of x, and σ_x is the standard deviation of x.

Chapter 3

Changes in the freshwater cycle and possible feedbacks

This chapter provides an overview on the components of the global freshwater cycle as it is represented in the CCSM3. In a first step, the freshwater flux to the ocean surface is investigated with respect to climatology and the changes it undergoes during the 21st century. Second, the freshwater budget in polar regions is discussed with a focus on different characteristic forcing conditions throughout the modeled years 1500-2098. Third, the oceanic freshwater export mechanisms of the Arctic Ocean are investigated as well as properties of the deep-water formation sites in both polar regions. Fourth, comparisons with observations and other models are provided. The chapter closes with a discussion.

3.1 Freshwater flux components

This section addresses the freshwater flux and its evolution over time. We take a look at the global pattern of the freshwater flux and the changes it undergoes. Further, we examine the different quantities the freshwater flux is made of and determine which ones contribute how much to the total change of the freshwater flux.

3.1.1 Freshwater flux to the ocean

The freshwater flux (FWF) to the ocean surface can be defined in different ways:

$$FWF_1 = P - E + R + M, \tag{3.1}$$
$$FWF_2 = P - E + R, \tag{3.2}$$
$$FWF_3 = P - E. \tag{3.3}$$

The definition of equation (3.2) is used by *Wu et al.* [2005] and is applied in this study for reasons of comparability.

The Hovmöller diagram in Fig. 3.1 shows that the freshwater flux to the ocean substantially increases particularly in the equatorial region between approximately 10° N and 10° S during

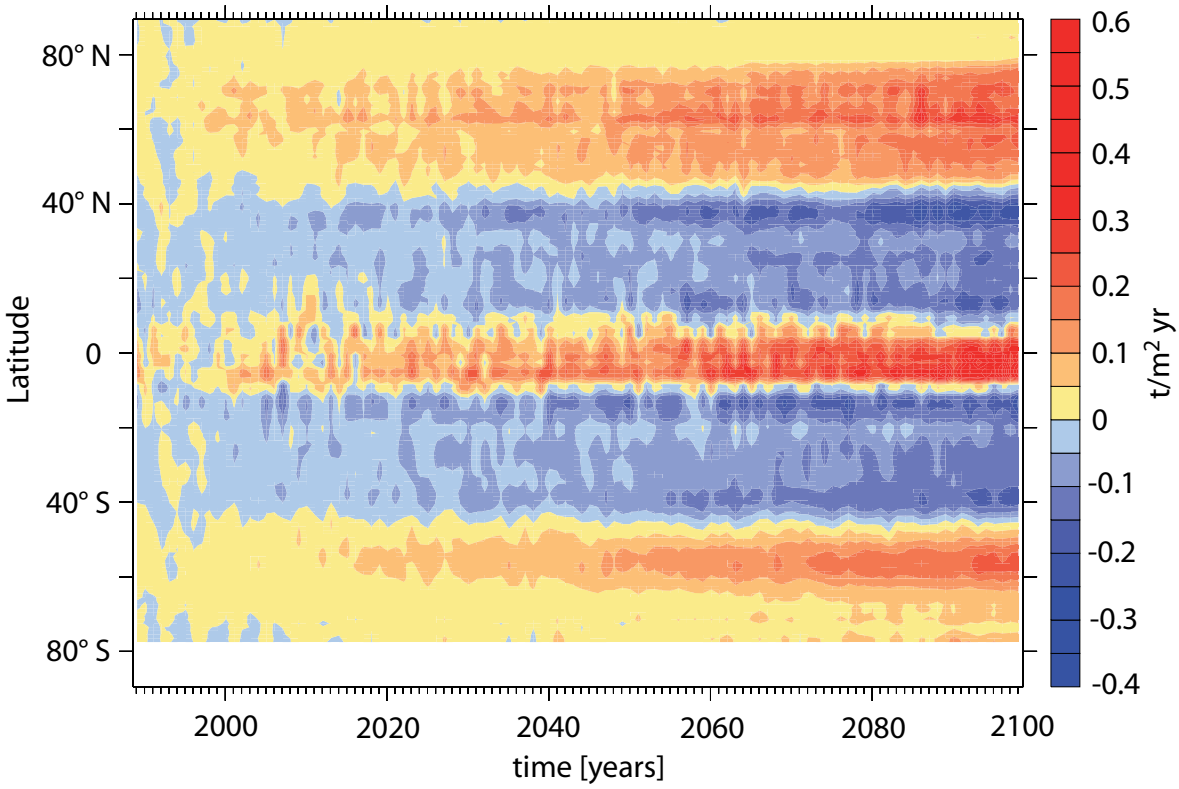

Figure 3.1: Hovmöller diagram of the ensemble annual mean freshwater flux to the ocean surface as anomaly to the period 1961-1990. Compare with Fig. 3.2.

the 21st century. In contrast, the subtropics to mid-latitudes show a continuous decrease in freshwater flux with two latitudinal maxima at approximately 35-42° N and 10-15° S. At latitudes higher than 45° N and S the freshwater flux exhibits a strong positive anomaly, leading to an increasing meridional gradient between the mid latitudes and the subtropics. Further, it can be seen that the anomaly in the northern high latitudes is stronger than in the southern high latitudes.

Expanding the Hovmöller diagram to the full length of available data (1500-2098) the dramatic increase of the meridional gradient of the freshwater flux becomes more obvious (Fig. 3.3). During the pre-industrial period (until 1870) no trends or shifts can be discovered beyond the natural variability of the zonal mean freshwater flux (compare with Fig. 3.4 which shows the data from EQ1500).

To investigate the time behaviour of the total freshwater flux through the ocean surface, we focus on specific regions. Fig. 3.5 shows the zonal mean anomaly of the freshwater flux to the reference period 1961-1990 for the regions 60°-90° N and 60°-90° S. Additionally, the difference between the freshwater flux of 60°-90° N and 60°-90° S is given for the same time period. The strong positive anomaly of the freshwater flux in both hemispheres during the 21st century, as it was shown already in Fig. 3.1 and 3.3, is well visible. However, the rate of change in the northern hemisphere is larger than in the southern hemisphere, resulting in a net gain in freshwater of the northern relative to the southern high latitudes, illustrated by

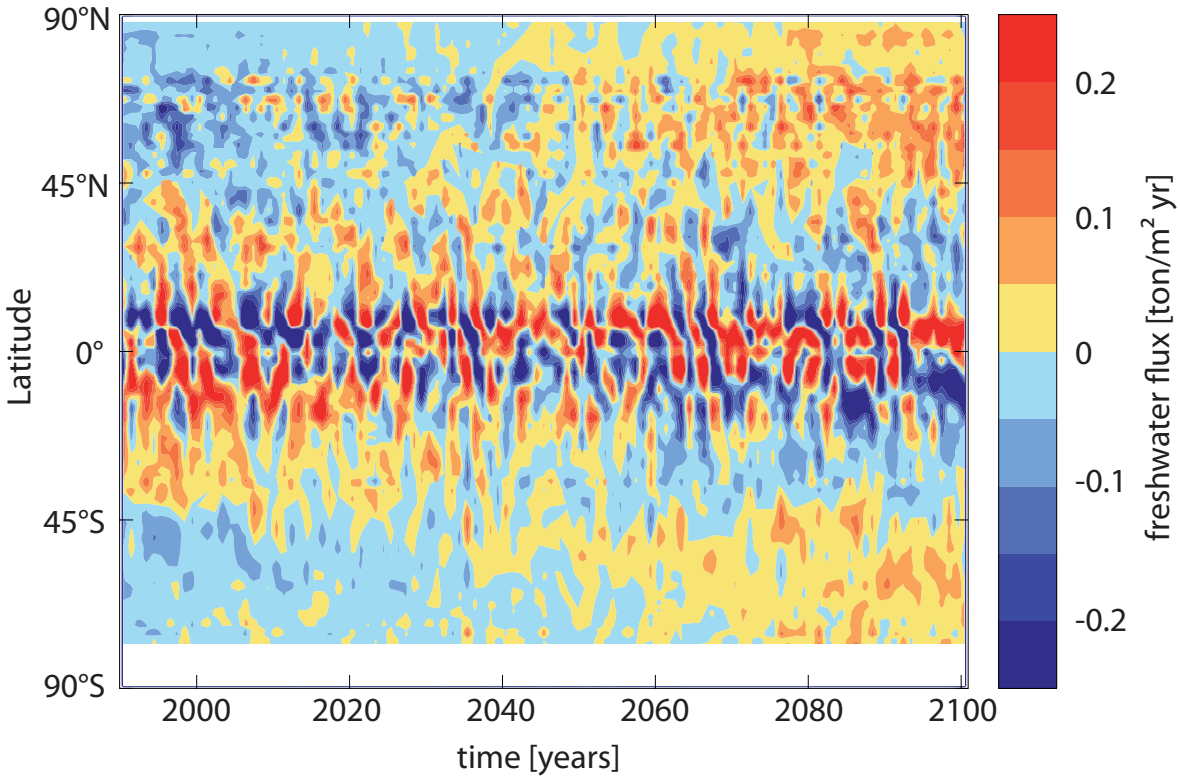

Figure 3.2: Hovmöller diagram of the annual mean freshwater flux into the ocean as zonal mean anomalies. Modified from *Wu et al.* [2005], Fig. 1.

the difference between the north and south.

The spatial structure of the freshwater flux in both polar regions is illustrated by a 100-year mean using EQ1500 (Fig. 3.6). In the Barents Sea the freshwater flux reaches values of up to 3 t m^{-2} yr^{-1} in the river discharge region of the Pechora, Ob and Yenisey. The runoff from the Lena, Kolyma and MacKenzie is also well represented in the model. Generally, the northern high latitudes maximum freshwater flux to the ocean is dominated by the summer influx from rivers and therefore occurs in coastal areas. On the other hand, the central Arctic Ocean, parts of the GIN Seas and a small area south of Iceland show a slightly negative freshwater flux.

In the southern high latitudes values of only up to 0.7 t m^{-2} yr^{-1} are found in the area of the Amundsen Sea. These freshwater fluxes are dominated by the runoff from Antarctic rivers, these being meltwater streams which in the model are defined as river runoff because they originate from actual land mass. This stands in contrast to the model quantity used to estimate sea ice meltwater flux, which covers meltwater fluxes from sea ice only. Negative freshwater fluxes are found in the Ross and Weddell Seas. Generally, the Southern Hemisphere tends to have a positive freshwater flux over most areas.

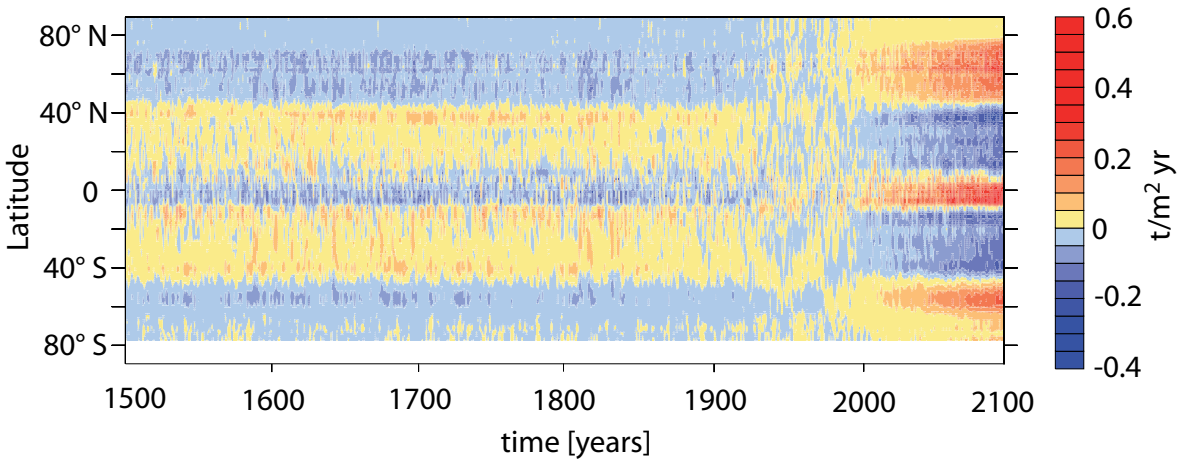

Figure 3.3: Hovmöller diagram of the ensemble annual freshwater flux to the ocean surface as anomaly to the period 1961-1990. Color bar and units as in Fig. 3.1.

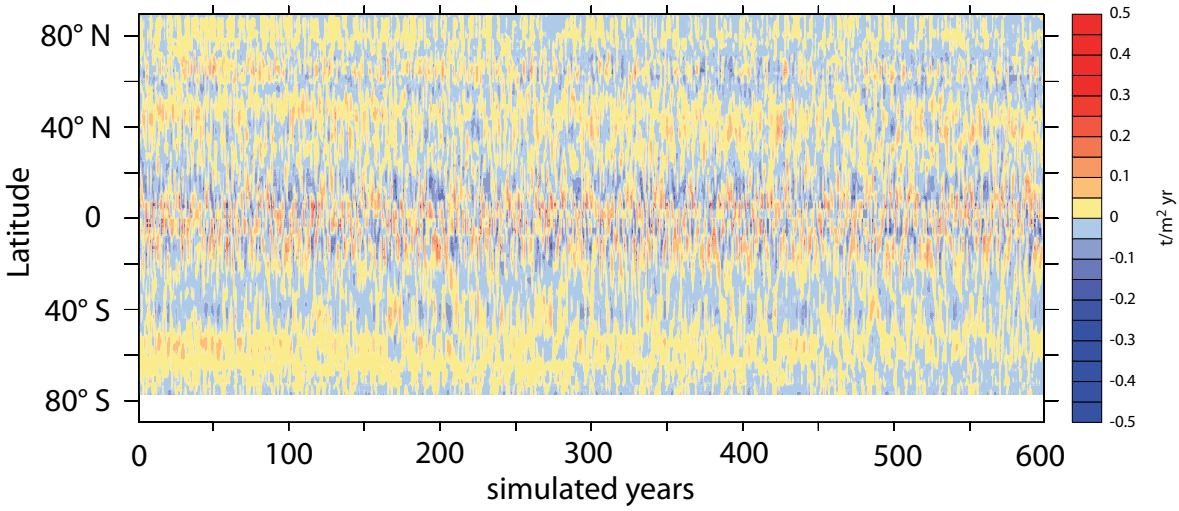

Figure 3.4: Hovmöller diagram of the annual freshwater flux to the ocean surface from EQ1500 as anomaly to the period 1961-1990.

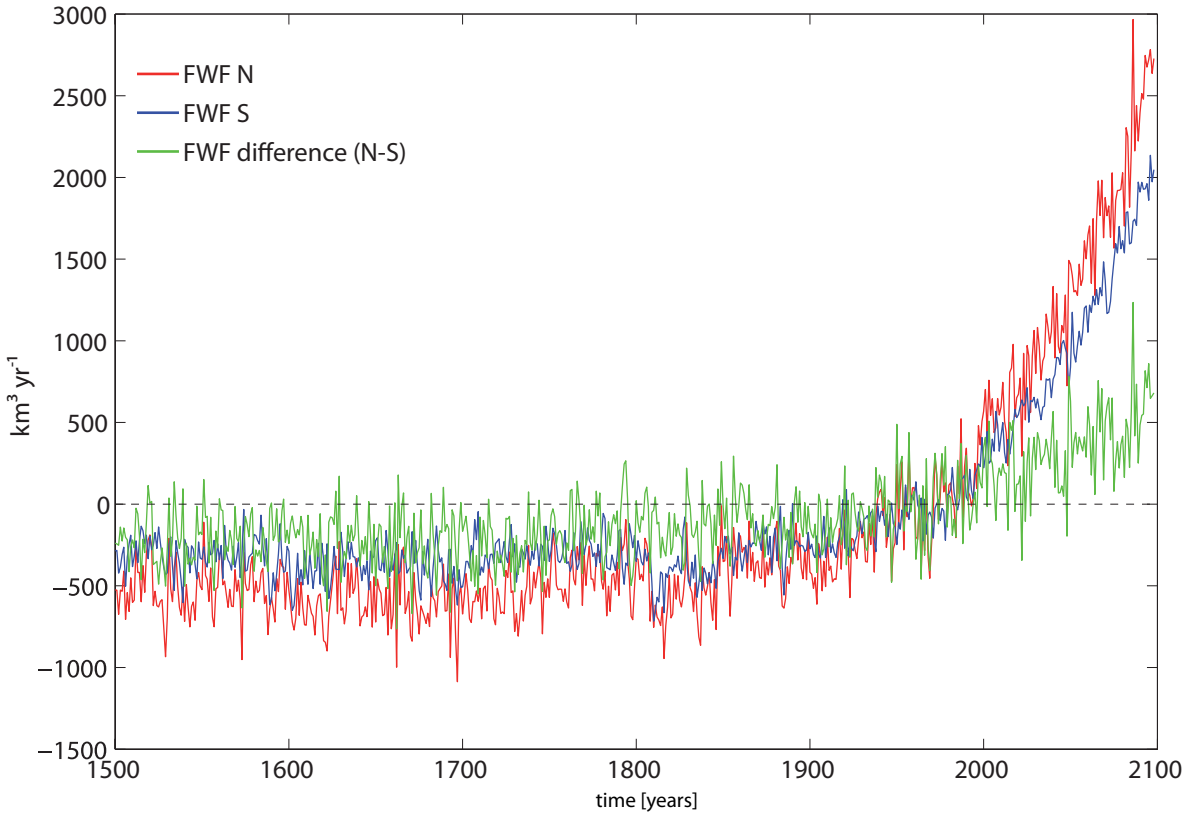

Figure 3.5: Ensemble mean of the spatially integrated annual freshwater flux to the regions 60°-90° N (red) and 60°-90° S (blue) as anomaly to the period 1961-1990, and the difference of the curves (green).

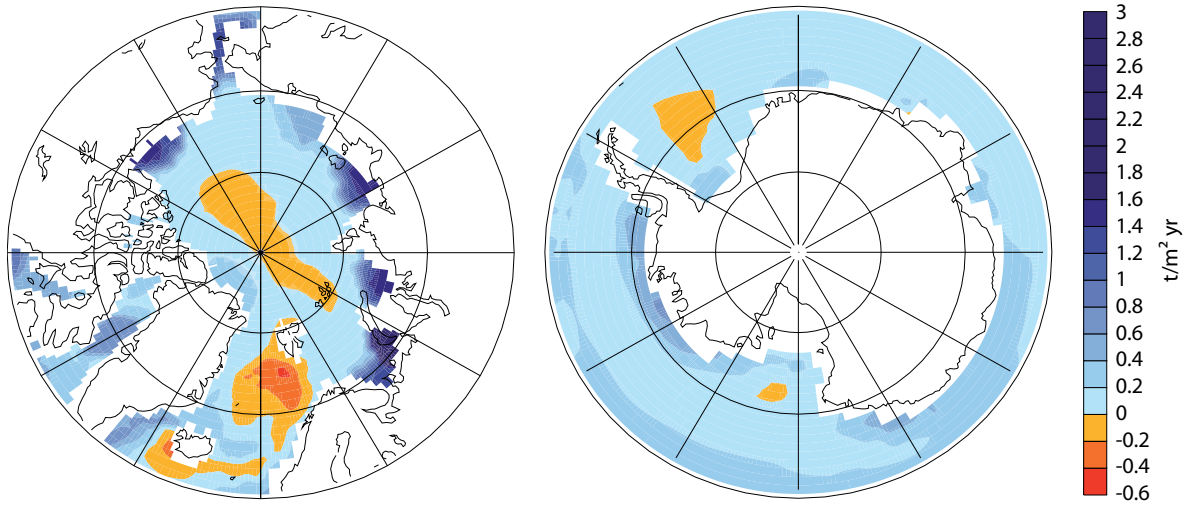

Figure 3.6: 100 year average freshwater flux from EQ1500 for the regions 60°-90° N (left) and 60°-90° S (right).

3.1.2 Precipitation, evaporation, runoff and sea ice meltwater

An overview of the spatial structure of precipitation, evaporation, runoff and sea ice meltwater in the polar regions is provided by Fig. 3.7. A 100-year mean of EQ1500 serves as a model-internal climatology. Fig. 3.7 (a) and (b) show an analogous size, shape and location of the maximum precipitation and evaporation patterns in both polar regions. Also, the absolute values are similar, resulting in a small net freshwater flux from P-E. Therefore the runoff (Fig. 3.7 (c)) dominates the freshwater flux with values of up to 3 t m^{-2} yr^{-1}. Fig. 3.7 (d) finally illustrates the freshwater flux originating from the forming and melting of sea ice. The northern high latitudes experience values between –2 and 13 t m^{-2} yr^{-1} with a strong gradient in the Greenland Sea and along the Denmark Strait, which reflects the sea ice export characteristics of this region. In the southern high latitudes negative values of down to –5 t m^{-2} yr^{-1} are found locally, while the general zonally-symmetric pattern (negative flux in coastal areas and positive flux on the open ocean) exhibits values between –2 and 2 t m^{-2} yr^{-1}.

The Hovmöller diagram in Fig. 3.8 (a) shows the change in annual mean precipitation to the ocean as a percent anomaly. The increase in precipitation in the 21st century is particularly high at northern high latitudes above 70° N, where the increase reaches values of 400%. This is mainly due to the fact that there is generally very little precipitation at these latitudes, thus small absolute changes have a large impact in terms of percent change. Fig. 3.8 (b) illustrates the zonal pattern of annual mean evaporation, where the percent increase is also highest in the northern high latitudes, owing to the retreating sea ice cover which enables formerly covered ocean regions to evaporate. Unlike the precipitation trend the evaporation is projected to increase also in the subtropical regions. The zonal mean runoff is displayed in Fig. 3.8 (c). Warming-induced melting of continental ice sheets and the intensification of the hydrological cycle lead to an increased runoff at nearly all latitudes. Decreased runoff from the east coast of North America and drying of parts of the Mediterranean area result in a small band of negative anomaly at mid-latitudes and subtropics. Note that the zonal mean runoff around 40-45° S is dominated by South America.

3.1.3 Annual and seasonal variability

The annual cycle of the freshwater flux in polar regions has a strong seasonal component, since precipitation, evaporation and runoff are temperature-sensitive quantities (see the annual cycle of surface air temperature in polar regions in Fig. 1.2). To further investigate changes in the annual cycle of the freshwater flux and its components, monthly means of two 30-year periods (1500-1530 and 2068-2098) are are used to estimate the mean annual cycle (Fig. 3.9 and Fig. 3.10). In the northern high latitudes the freshwater flux annual amplitude for the period 1500-1530 (Fig. 3.9 (a)) ranges from below 1,000 km^3 yr^{-1} in early spring up to over 15,000 km^3 yr^{-1} in July. It is well visible, that the runoff dominates the freshwater flux. $P-E$ contributes only a small amount and shows positive values only from June through October. Under the A2 scenario the basic structure of the annual cycle is maintained (Fig. 3.9 (b)). The amplitudes of freshwater flux and runoff are amplified simultaneously, confirming runoff in its dominant role. Meanwhile, the maxima of precipitation and evaporation in September and October, respectively, do not increase at the same rate, which results in a positive anomaly of $P-E$ during late summer/autumn. At the same time runoff decreases slightly. The resulting

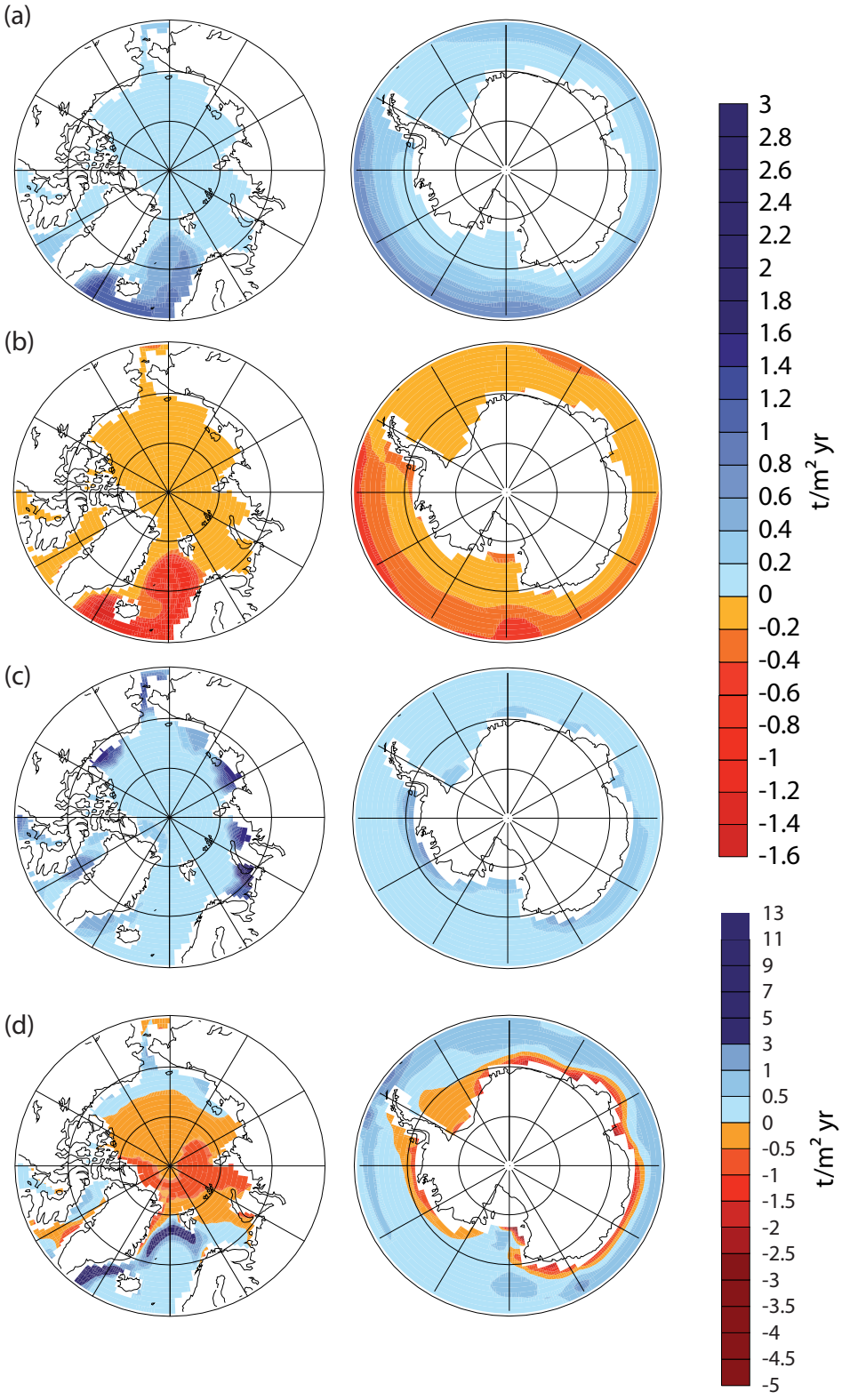

Figure 3.7: 100 year average of annual mean precipitation (a), evaporation (b), runoff (c) and sea ice meltwater (d) from EQ1500 for the regions 60°-90° N (left) and 60°-90° S (right). Note that the scale for (d) is non-linear and different from the scale for (a)-(c).

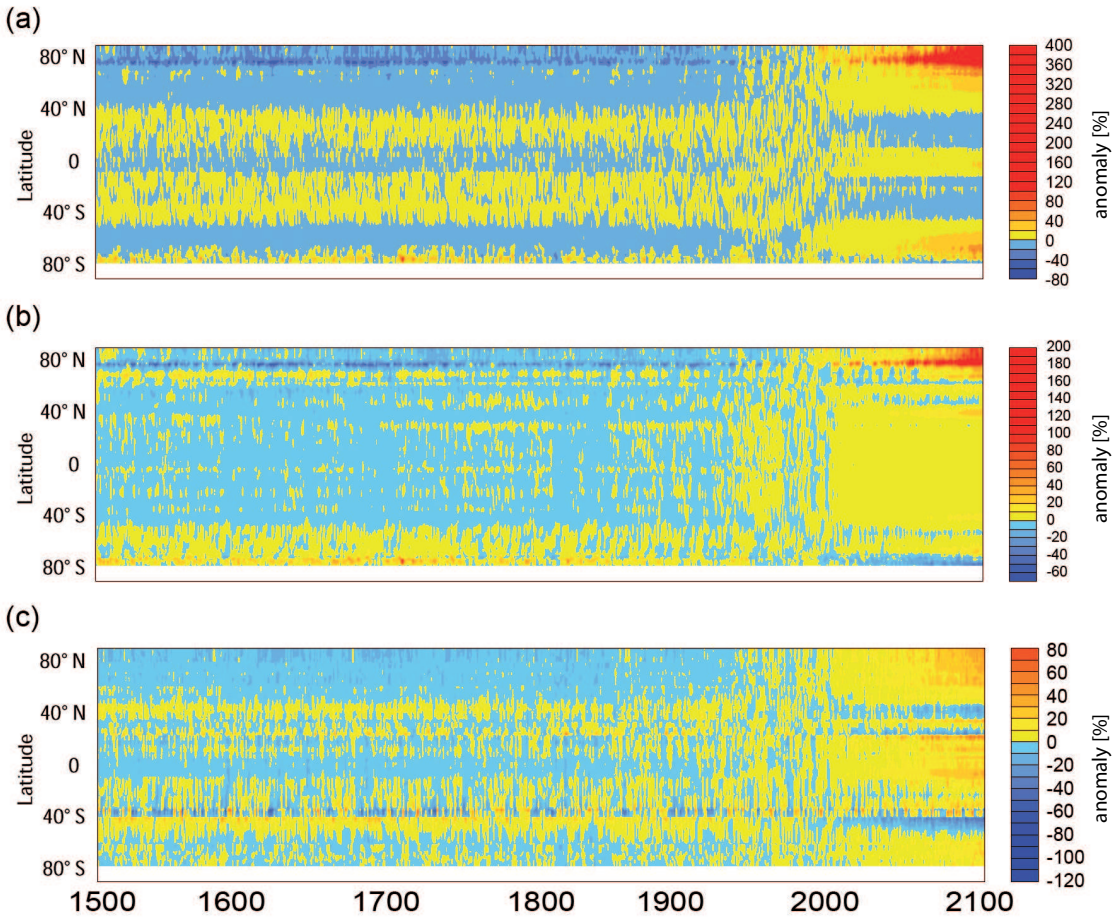

Figure 3.8: Hovmöller diagram of the ensemble annual mean precipitation (a), evaporation (b) and runoff (c) to the ocean surface as anomaly to the period 1961-1990.

gap between runoff and freshwater flux is well visible during August, September and October, where a larger part of the freshwater flux originates from $P - E$.

In the southern high latitudes the maxima of precipitation and evaporation exceed the freshwater flux and runoff maxima (Fig. 3.10 (a)). However, the net flux from $P - E$ only plays a significant role during the southern hemisphere summer months, whereas it drops to around zero in winter. During these boreal winter months the positive freshwater flux is equal to runoff, which does not have a large annual amplitude. Looking at the data from the period 2068-2098 we find a drastic increase in precipitation during the southern hemispheric summer while evaporation remains almost unchanged (Fig. 3.10 (b)). As runoff does not change significantly either, this shows that the southern high latitudes are dominated by $P - E$ rather than runoff. This is in contrast to the northern high latitudes, suggesting that different processes are relevant for the future increase.

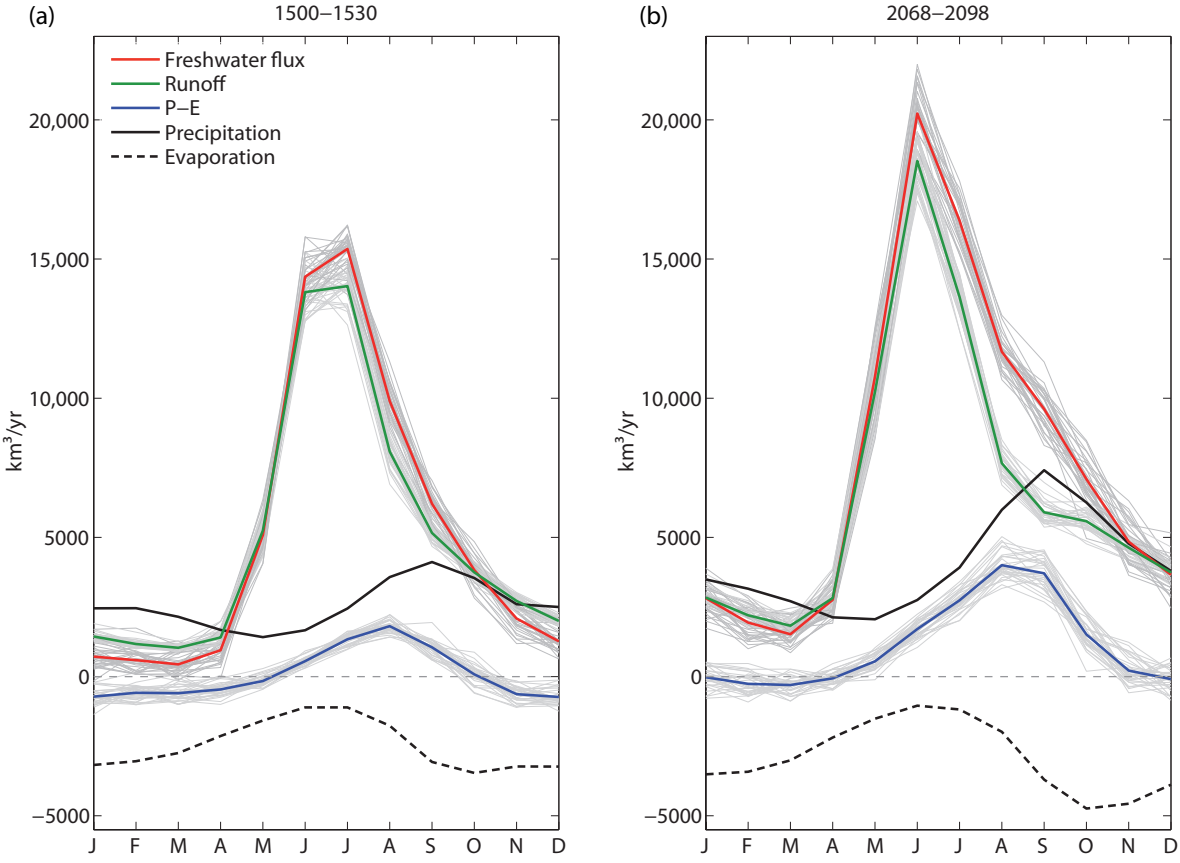

Figure 3.9: Annual cycle of the freshwater flux and its components at 60°-90° N for the period 1500-1530 (left) and 2068-2098 (right). Gray lines are individual years from the 30-year period, colored lines are the 30-year mean. Precipitation is the positive black line, evaporation the negative black line.

To investigate the change of the inter-annual variability of the freshwater flux, the standard deviation averaged over a 50-year moving window is estimated for the two regions of 60°-90° N and 60°-90° S (Fig. 3.11). Therefore, 50 years of monthly data are taken and detrended linearly before the standard deviation of these 50 years is determined. The resulting value is given as percent deviation from the mean of 1500-1899. The curves of the four transient runs are summarized in a grey shading, symbolizing the maximal spread among the four runs.

In the region of 60°-90° N the standard deviation fluctuates within a range of approximately ± 1-3% during the preindustrial period which is on similar order as the fluctuations of the control run EQ1500. While there are no detectable signals of the natural forcing variations during that period the values of the 20th and 21st century show a distinct upward trend and rise to approximately 12% above the long term mean for the period of 2048-2098 (Fig. 3.11, top). As can be seen from the spread, the four transient runs do not diverge among each other in displaying the increasing inter-annual variability of the freshwater flux. Looking at the region of 60°-90° S (Fig. 3.11, bottom) a somewhat different picture is found. The variations of the moving window standard deviation are slightly higher during the pre-industrial period (± 6-7%; also within range of EQ1500), at least in percent terms. Also, the four transient runs oscillate in a less uniform way, which results in a spread of nearly 10% during

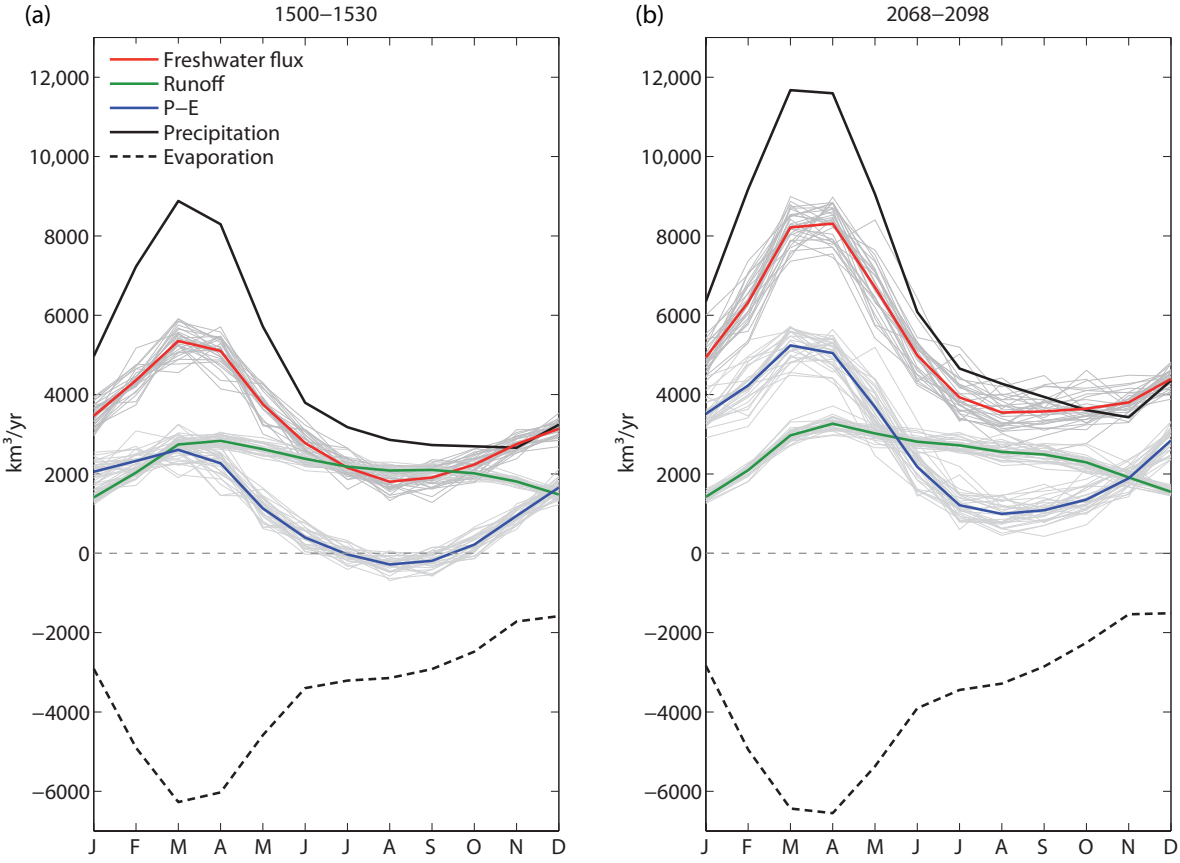

Figure 3.10: Annual cycle of the freshwater flux and its components at 60°-90° S for the period 1500-1530 (left) and 2068-2098 (right). Legend as in Fig. 3.9.

the years around 1560, 1750 and 1800. At the beginning of the 20$^{\text{th}}$ century the ensemble mean standard deviation is higher than the variability of EQ1500. By 1960 the spread of all transient runs outreaches the EQ1500 range as well. During the 21$^{\text{st}}$ century the moving window standard deviation rises by over 40% compared to the long-term mean, indicating a strong increase in inter-annual variability of the freshwater flux to the ocean at 60°-90° S.

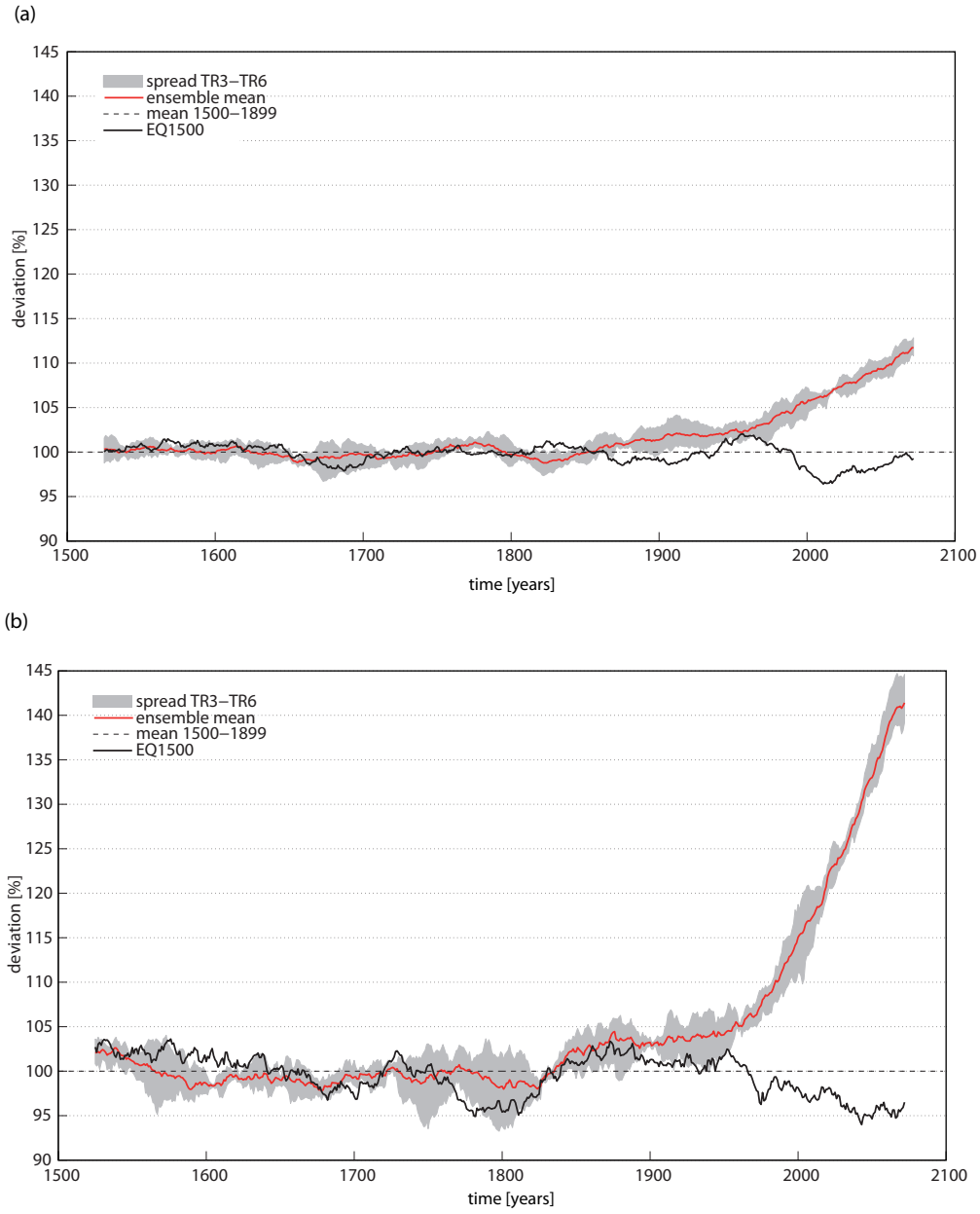

Figure 3.11: Freshwater flux 50-year moving window standard deviation for 60°-90° N (top) and 60°-90° S (bottom). Deviation from the mean standard deviation of 1500-1899 is shown in percent. The maximum spread throughout the four transient runs is given by the grey shading. The values are plotted at the middle year used in the calculation of the standard deviation, so the values for 1525 represent the period 1500-1550.

3.2 Freshwater Budget

The freshwater budget or freshwater balance gives an estimate on how much freshwater is available in a specified system. In order to quantify the budget of a system, its boundaries must be defined and all the freshwater fluxes which enter and exit the system have to be determined. In case of the freshwater cycle in polar regions these fluxes are defined as illustrated schematically in Figs. 3.12 and 3.16. The atmosphere serves as a short-term water storage and tends to be a freshwater source to the polar regions due to meridional advection of moisture (∇Q). It interacts with the land and ocean surfaces via precipitation (P) and evaporation (E). The land component delivers river runoff (R) to the ocean. In this schematic view the sea ice component is included in the ocean component, mainly serving as an annual to inter-annual freshwater storage and in the case of drifting sea ice as a prominent freshwater export or import mechanism. The ocean component inherits a freshwater excess or deficit (referred to as freshwater content) relative to a reference salinity. In this study the reference salinity is defined as the model's global average salinity of 34.7 g kg^{-1}. Sea ice is assumed to have an average salinity of 4 g kg^{-1}, which is taken into account to calculate the freshwater equivalent of the sea ice volume. Oceanic exchange of freshwater for a specified system can be calculated as the residual from the freshwater content (excess or deficit) and the freshwater fluxes at the ocean surface (see section 2.3.2).

In Fig. 3.12 and 3.16 we present an overview of the freshwater budget of the Arctic and Antarctic region (represented by the domains 60-90° N and 60-90° S) for four different 30-year periods throughout the modeled data. The period 1500-1530 (Period I) resembles the steady state from which the model was spun up and is situated within a period of lower solar activity compared to today (see Fig. 2.5). The period 1685-1715 (Period II) is located around the Maunder Minimum, a phase of particularly low solar activity. To enable the possibility of comparing with the last full climatological reference period, the years 1960-1990 (Period III) have been selected. Finally, 30 years at the end of the 21st century (Period IV) indicate how the freshwater budget changes in a warming climate. Also, the percent change between the first and last 30-year period of each quantity is given (small black font).

In addition, Figs. 3.13 and 3.17 show the components of the freshwater budget of the ocean only. Annual means for all 599 model years indicate the long-term trend of the single quantities and document the different rates of change among the quantities.

3.2.1 Arctic region

As it was stated in the Introduction the Arctic region features a complex geographical structure as well as a heterogenic bathymetry, which are only coarsely resolved by the model grid. For example, the CAA is represented only by a single pathway. Nevertheless, large-scale atmospheric and terrestrial fluxes, as well as important exchange paths in the Bering Strait, Fram Strait and CAA, can be estimated and compared to observations. The estimates from the review paper on the large-scale freshwater cycle of the Arctic by *Serreze et al.* [2006] serve as a reference.

The atmospheric water vapour storage during Period II is smaller than during Period I, re-

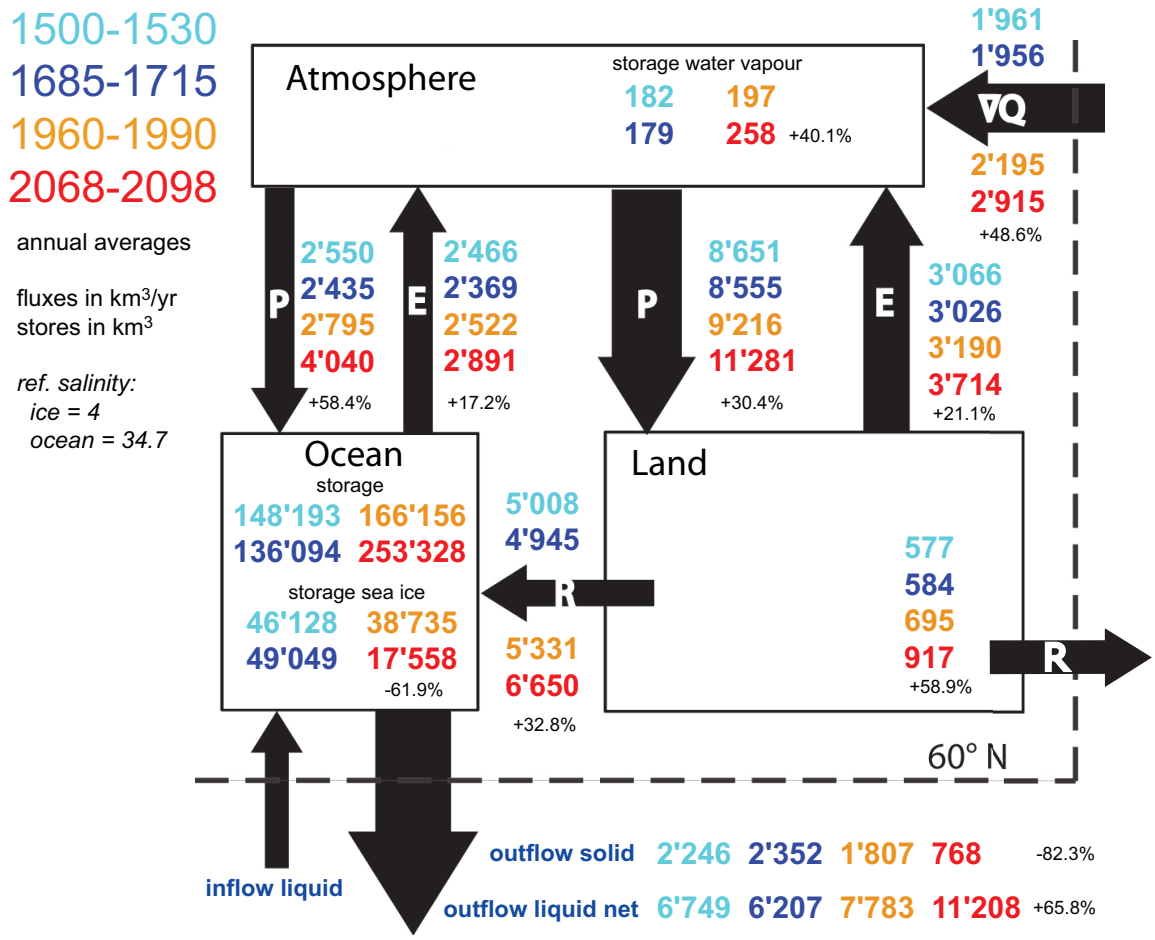

Figure 3.12: Freshwater budget of 60-90° N. Values are ensemble mean 30-year averages according to the colour shading in the upper left corner. Changes between the the first and last period are given in percent (small black font). Note that the runoff leaving the region 60-90° N via land is just estimated from the residual of $P - E - R$ over land, assuming a constant moisture storage by the land component. The oceanic inflow ("inflow liquid") is not specifically given, but is included in the net value of outflow out of the domain ("outflow liquid net").

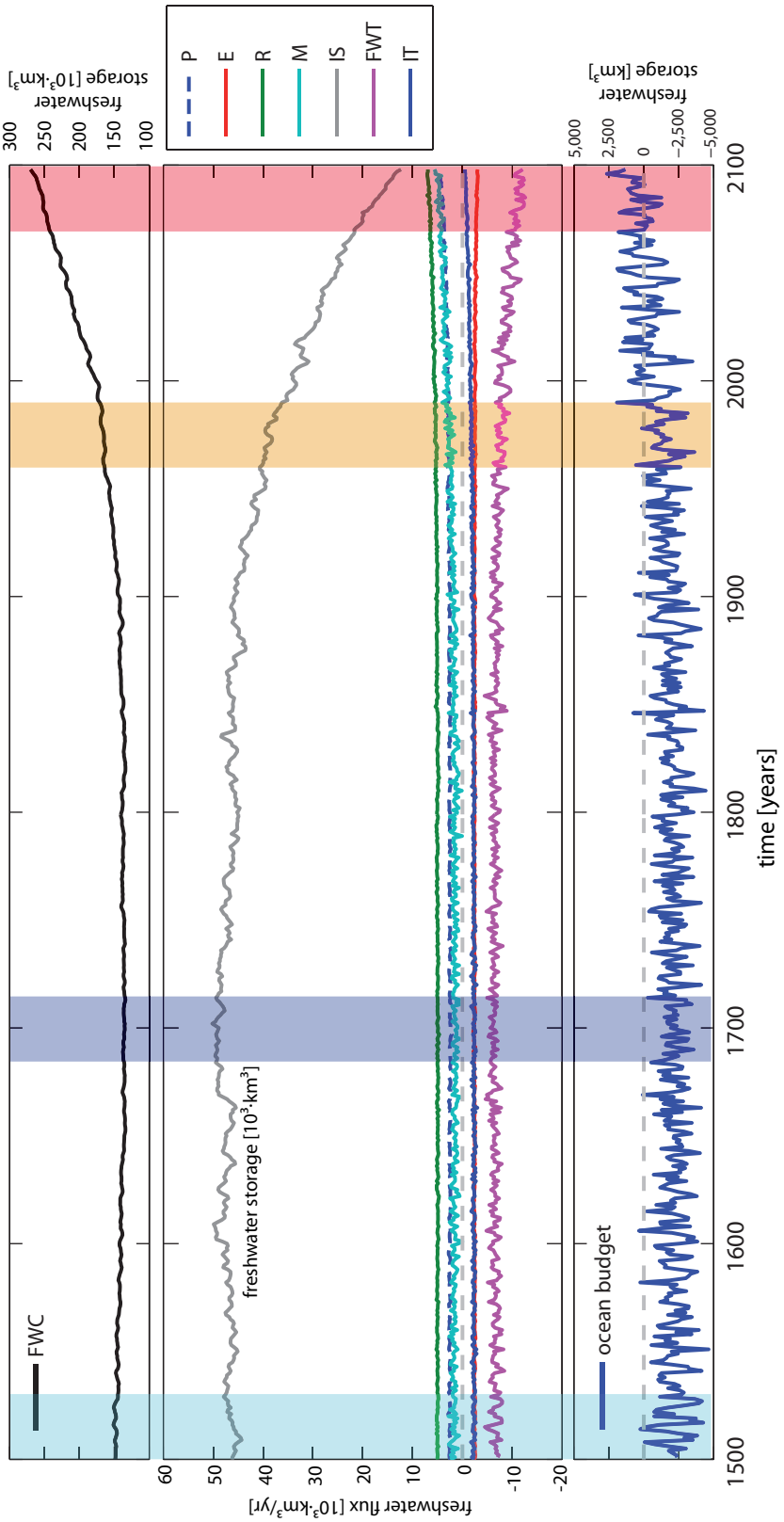

Figure 3.13: Temporal evolution of the single components of the freshwater budget of the ocean at 60-90° N from the ensemble mean: freshwater content (FWC), precipitation (P), evaporation (E), runoff (R), sea ice meltwater (M), ice storage (IS, freshwater equivalent), freshwater transport (FWT), ice transport (IT, freshwater equivalent) and the net ocean budget ($P + R + M + E + IT + FWT$). Data is given as annual means and units of fluxes/transports and stores are in km^3 yr^{-1} and km^3, respectively. Fluxes and transports into the ocean are represented by positive values. The coloured shading resembles Period I through Period IV from Fig. 3.12.

sembling the slightly colder conditions of the Maunder Minimum. Period IV reaches a value of 258 km^3, thereby being approximately 40% higher than Period I and Period II. Along with the atmospheric storage the meridional moisture advection increases as well by over 48% during the six centuries. The same change of increased flux can be found for precipitation and evaporation to and from the ocean surface, respectively. However, the percent increase of precipitation in the 21^{st} century is significantly larger than the increase in evaporation, indicating an growing imbalance in terms of net freshwater flux from the atmosphere to the ocean. As we have seen in section 3.1, runoff increases at high latitudes and plays an important role in the freshwater budget of the Arctic region. Here the runoff increases by about a third from Period I to Period IV. These findings are confirmed by the ocean's freshwater content, which rises by over 70% as a consequence of the increased net flux of freshwater from the atmosphere and land component. The equivalent freshwater storage in sea ice on the other hand is modeled to decrease drastically by over 60%. This could imply that sea ice gradually loses its importance in storing the freshwater on inter-annual time scales. The exchange of freshwater between ocean and atmosphere could be accelerated since sea ice no longer acts as a buffering storage system. The export rate of sea ice is reduced significantly as well in between Period III and Period IV. On the other hand, the oceanic outflow increases massively by 80% from Period II to Period IV, overcompensating the weakening sea ice export as well as the increasing contributions of runoff and $P - E$.

The freshwater content in the region of 60-90° N increases nearly exponentially after the pre-industrial period (Fig. 3.14). Surprisingly, the four transient runs (TR3 to TR6) show a great variance among each other, while their individual variance is comparably low. During the period 1650 to about 2000 the four transient runs each take a slightly different path to then converge again during the 21^{st} century. TR6 drops to about 15% below the initial state around 1650 and returns into the range of EQ1500 values during the 19^{th} century, TR5 drops between 1700 and 1720 and returns around 1900. TR4 reaches a minimum at about 1890 whereas TR3 experiences a maximum during the 18^{th} century and never drops below the variability of EQ1500. Since all of these phenomena occur during the pre-industrial period, looking for triggering fluctuation in the natural forcing seems reasonable. About 40% of the drop of TR6 happens in the decade following the volcanic eruption of 1640. TR6 shows a smaller drop directly after an eruption in 1728. TR5 collapses after a series of eruptions at the end of the 17^{th} century. Two strong eruptions at the beginning of the 19^{th} century coincide with a solar minimum (the Dalton Minimum) and are accompanied by a strong reduction in freshwater content in TR4. TR4 and TR5 show a less drastic but still very distinct reaction after an eruption in 1882. However, due to the large long-term amplitude of the natural variability the behaviour of the different runs cannot be clearly attributed to volcanic or other natural forcing fluctuations.

3.2.2 Arctic Ocean basin

The freshwater budget of the Arctic Ocean and its temporal evolution is shown in Fig. 3.15 and in Table 3.2.2 the 30-year means are listed as they are applied also in Fig. 3.12 and 3.13.

Looking at Table 3.2.2 it is apparent that the biggest changes in the Arctic Ocean's freshwater budget occur between Period III and Period IV, when the greenhouse gas concentrations

Table 3.1: Freshwater budget of the Arctic Ocean. Averaging periods Period I through Period IV as defined in section 3.2. Abbreviations as defined in Fig. 3.13. Fluxes in $km^3\ yr^{-1}$, stores in km^3. Fluxes leaving the region are negative, the net transport is calculated as $P + E + R + FWT + IT$. The change from Period I to Period IV is given in percent.

time period quantity	Period I	Period II	Period III	Period IV	change [%]
P	228	207	287	697	206
E	-180	-167	-209	-384	113
R	3,160	3,121	3,369	4,210	33
FWT	-943	-437	-1,742	-5,249	457
IT	-1,923	-2,079	-1,700	-579	-70
net transport	*342*	*645*	*5*	*−1,305*	
FWC	126,930	118,230	144,220	222,650	75
IS	37,697	93,437	31,794	15,524	-59

increase. The relative changes are also significantly larger than in the whole Arctic region of 60-90° N. The oceanic freshwater export is more than quadrupled which might be due to the increasing imbalance of net precipitation and the growth in runoff volume. At the same time, ice volume and export decrease, which results in even more freshwater delivered to the ocean. As a consequence of this, the oceanic freshwater content in the Arctic Ocean rises despite the heavily increased oceanic freshwater export.

In Fig. 3.15 the temporal evolution of the quantities from Table 3.2.2 is shown. It again becomes evident that major changes in the freshwater budget of the Arctic Ocean occur in the industrial period. During the course of the 21st century the Arctic Ocean turns from a net freshwater source into a net freshwater sink, if one takes the net oceanic budget ($P+R+M+E+IT+FWT$) as a measure. This is consistent with the budget simulated for the whole Arctic region of 60-90° N. The freshwater content (FWC) and freshwater transport (FWT) both show strong increases already from Period II to Period III and are correlated with $R = 0.96$ on basis of annual means (see section 3.3).

3.2.3 Antarctic region

Compared to the Arctic region Antarctica and the Southern Ocean form a rather simple ocean bathymetry (Fig. 1.4). A complex ocean circulation with globally important deep-water formation regions as well as a strong atmospheric forcing by extreme winds and temperatures are well know characteristics of this region. Nevertheless, observational campaigns in this region are sparse due to difficult accessibility and lack an integral review study addressing the freshwater cycle of the Antarctic region as a whole. Analogously to the Arctic region, Fig. 3.16 presents an overview on the Antarctic region's freshwater budget as it is simulated in the model.

The storage of freshwater as atmospheric water vapour is roughly 30% smaller in the Antarctic region than in the Arctic, which is mainly due to the lower temperatures and the polar

vortex which suppresses meridional moisture advection. From Period I through Period IV this storage shows a behaviour similar to the one in the northern high latitudes with small changes (on the order of 1-5%) during the first three periods and a distinct increase in storage volume during the 21st century. With a rise of approximately 24% the changes are smaller than in the northern high latitudes. Meridional moisture advection increases at nearly the same percent rate as the water vapour storage. Precipitation and evaporation to and from the ocean surface both increase from Period I to Period II and do not show the slight decreasing trend the same quantities do in the northern high latitudes. Surprisingly, evaporation from the ocean surface during Period III is even lower than during the previous periods. As it was stated in section 3.1.3 evaporation does not show a strong reaction to the greenhouse gas forcing during the 21st century whereas precipitation increases by nearly 40%. Section 3.1.3 also concludes that runoff does not change significantly in its annual variability. Nevertheless, a small long-term increase of 13% can be detected during the 599 modeled years. Even though surface air temperatures do not increase as strongly as in the northern high latitudes, the freshwater storage in sea ice still decreases by over 35%, whereby the strongest loss is simulated between Period III and Period IV. At 60° S the export of freshwater by means of drifting sea ice is more widespread and over three times larger than at 60° N. However, the absolute volume of exported sea ice is reduced only by 26% while at 60° N a reduction of more than 80% compared to the pre-industrial amount occurs. The oceanic freshwater storage in the southern high latitudes also behaves differently from the northern counterpart as it does not build up over time but decreases by approximately 5% from Period I to Period III and remains on this slightly lower level during the 21st century. The oceanic outflow on the other hand shows a strong increase of over 75% throughout the four periods. As for the northern high latitudes, this results in a growing imbalance of the flux terms towards an export of freshwater from the region 60-90° S. Still, despite the decrease of the net ocean budget ($P + R + M + E + IT + FWT$) during the 21st century the ocean in the Antarctic region at 60-90° S remains a freshwater sink. Since the net ocean budget is a compilation of several fluxes it undergoes large inter-annual variability (Fig. 3.17).

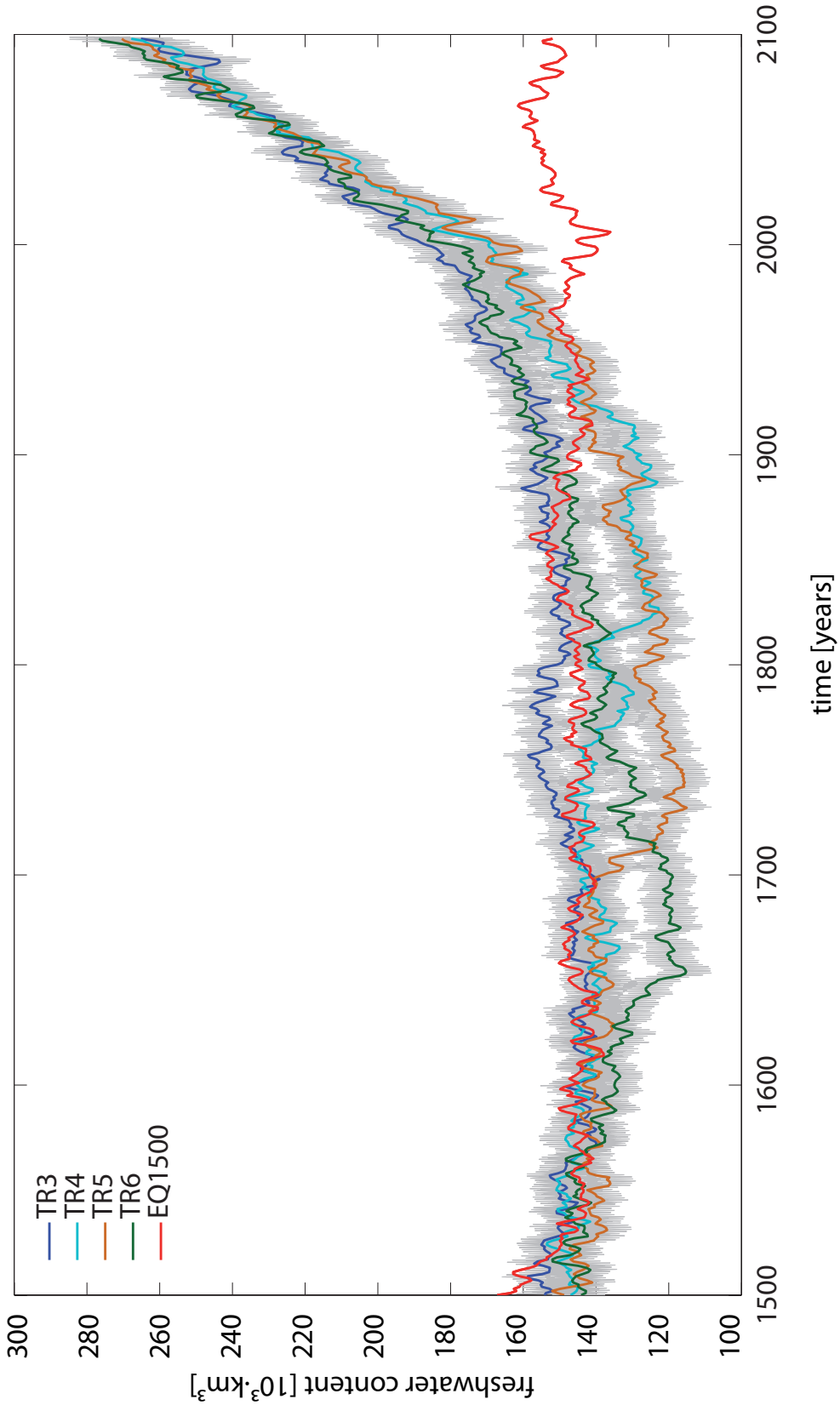

Figure 3.14: Oceanic freshwater content at 60-90° N. Monthly means (grey) and annual means (coloured) are plotted of the four transient runs and the control run.

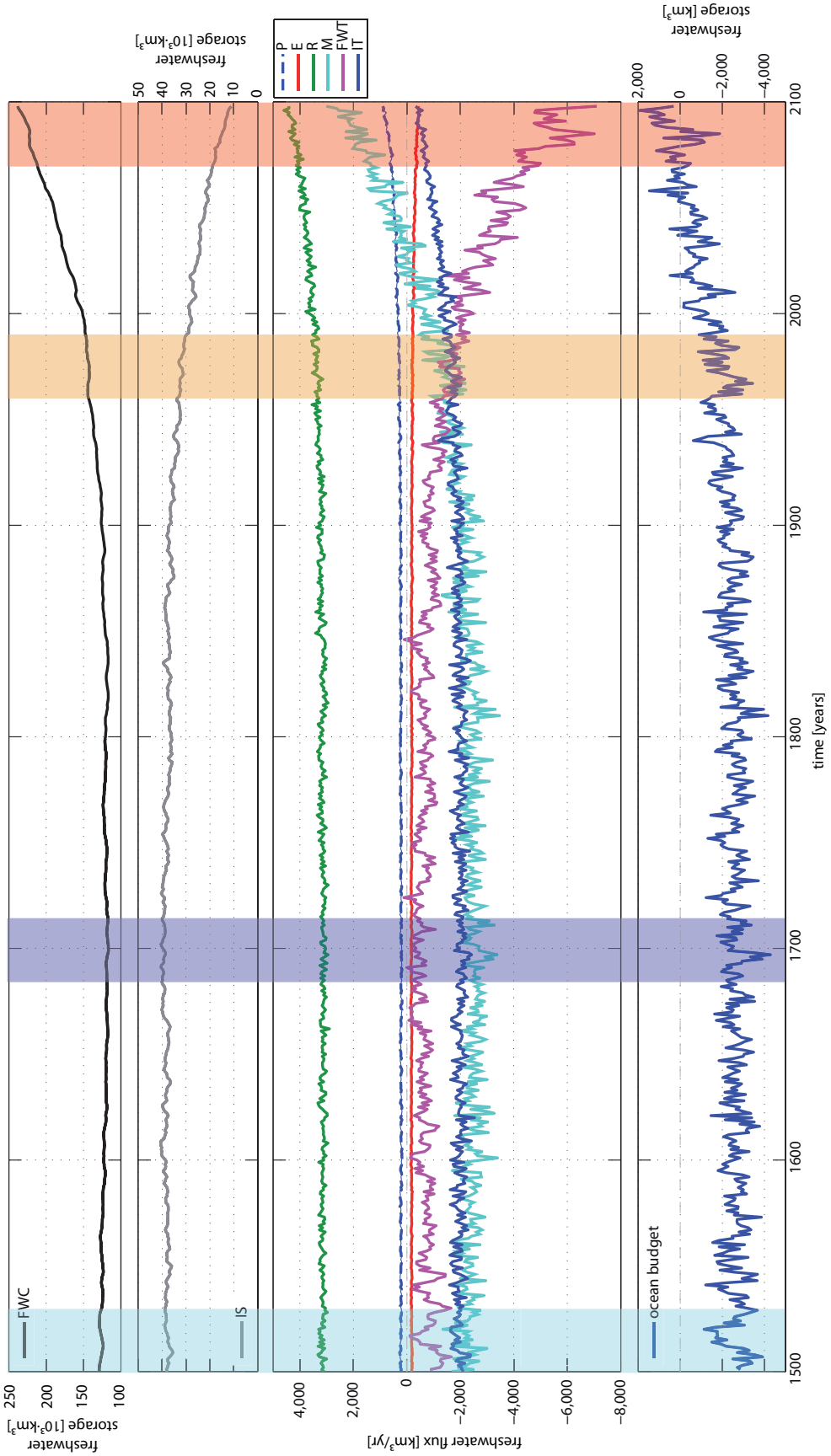

Figure 3.15: Temporal evolution of the single components of the freshwater budget of the Arctic Ocean from the ensemble mean. Abbreviations and units as in Fig. 3.13.

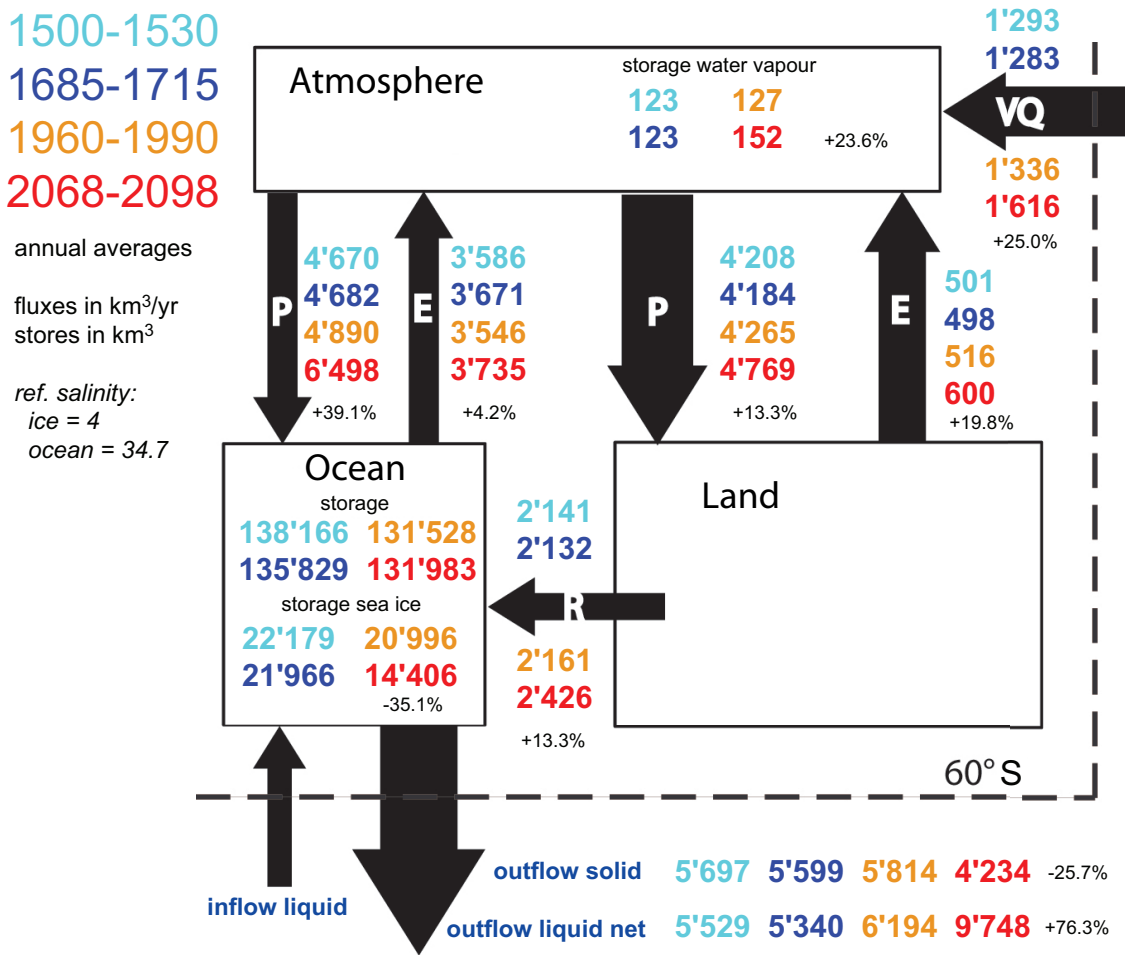

Figure 3.16: As in Fig. 3.12 but for 60-90° S.

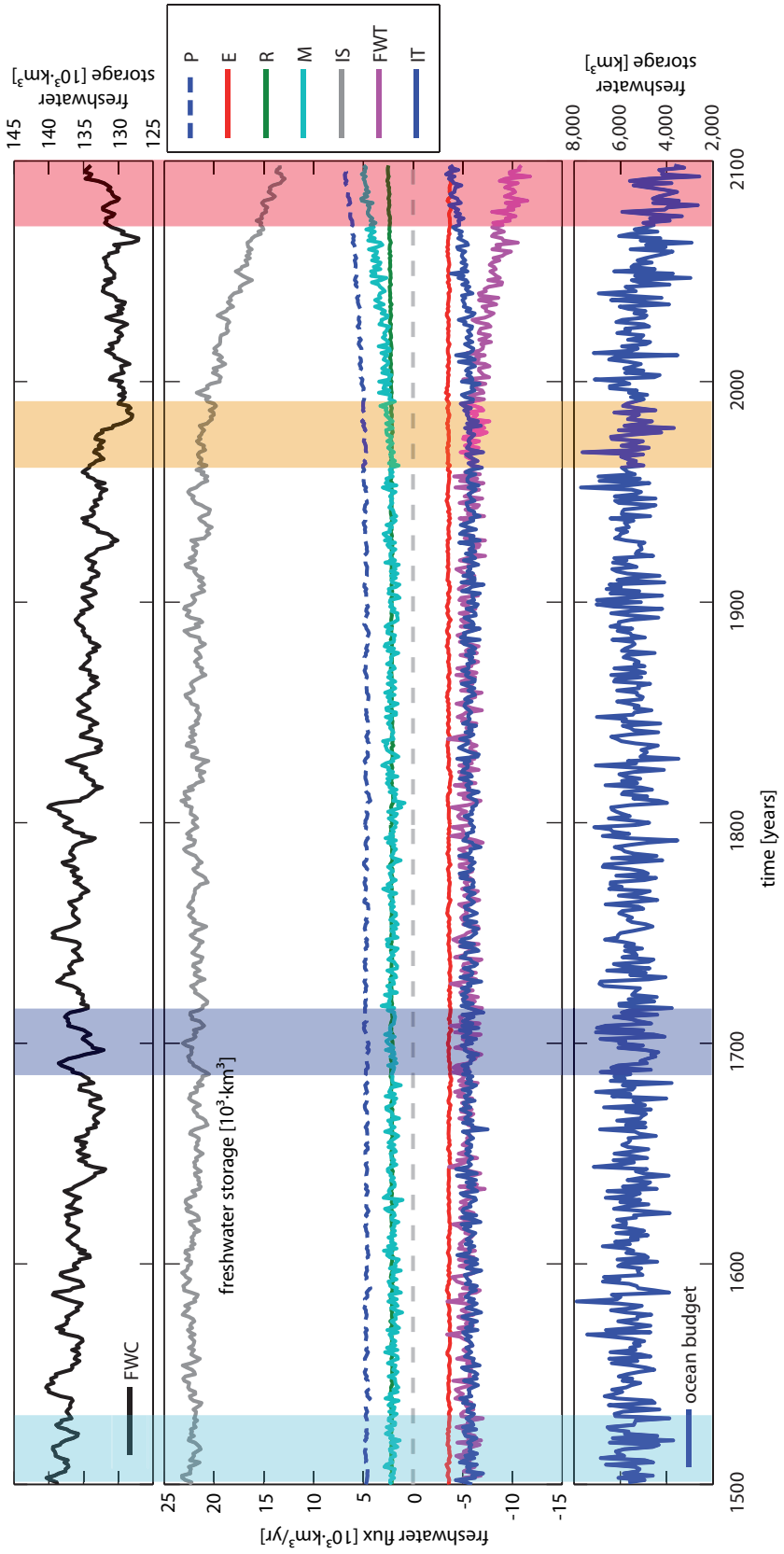

Figure 3.17: Temporal evolution of the single components of the freshwater budget of the ocean at 60-90° S from the ensemble mean. Abbreviations and units as in Fig. 3.13.

3.3 Freshwater transport and Meridional Overturning

3.3.1 Ocean passages

The oceanic transport out and into the Arctic Ocean is restricted to the Fram Strait, Barents Sea, CAA and Bering Strait (see Fig. 1.5). The ensemble annual means of the liquid transport through the four passages and their sum are shown in Fig. 3.20 from 1500-2100. During the pre-industrial period the liquid transport through all four passages does not show a trend and fluctuates within a range of $\pm$ 500 km^3 yr^{-1}. The reaction to the gradual increase in greenhouse gas concentrations during the industrial period is remarkably non-uniform among the four passages regarding its timing. At the beginning of the 20$^{\text{th}}$ century the transport through the Fram Strait increases, doubles until about 2020 and triples until the end of the 21$^{\text{st}}$ century. The inter-annual variability of the liquid freshwater transport through the Fram Strait increases as well during the 21$^{\text{st}}$ century. The liquid transport through the CAA increases at a smaller rate during the 21$^{\text{st}}$ century. However, the export through the CAA accelerates the upward trend during the 21$^{\text{st}}$ century and triples its export volume as well. The Bering Strait liquid transport, which is an import of freshwater into the Arctic Ocean at all times, shows no deviation during the 20$^{\text{th}}$ century from the long-term mean of approximately 2,500 km^3 yr^{-1}. However, during the 21$^{\text{st}}$ century it is strongly reduced to values between 0 and 1,000 km^3 yr^{-1}. Reasons for this might on the one hand be changes in the wind field. Fig. 3.18 shows the mean wind field for the periods 1500-1599 and 2000-2099 over the North Pacific. Therein no large changes which might be able to explain the decrease in Bering Strait liquid transport can be detected. The increasing sea surface height (SSH) gradient between the Arctic Ocean and the North Pacific, on the other hand, seems to be a plausible cause for the strongly reduced transport through the Bering Strait (Fig. 3.19). While the North Pacific maintains its SSH, the Arctic Ocean's SSH is lifted (not shown) and exceeds the SSH of the North Pacific in the first half of the 20$^{\text{th}}$ century. This suggests that the density decrease in the Arctic Ocean due to freshening and warming is mainly responsible for the increasing SSH gradient shown in Fig. 3.19.

The Barents Sea liquid transport varies around 0 km^3 yr^{-1} during the pre-industrial period with a net value of about -50 km^3 yr^{-1} during that time period. A possible reaction to the increasing greenhouse gas concentrations during the 20$^{\text{th}}$ century remains undetectable. During the 21$^{\text{st}}$ century, however, the Barents Sea liquid transport tends to act as an importer of freshwater to the Arctic Ocean. This finding is not very robust as the inter-annual variability of the freshwater transport becomes very large during the 21$^{\text{st}}$ century. In total, the four passages confirm the Arctic Ocean as a liquid freshwater source, whereby the amount of exported liquid freshwater grows remarkably by a factor of about ten from the pre-industrial period until the end of the 21$^{\text{st}}$ century. Regarding the combined liquid and solid export of freshwater, the factor is about two.

While the export of liquid freshwater from the Arctic Ocean is projected to increase, a shrinking of the export of solid freshwater is expected for the future (Fig. 3.21). In all four passages sea ice is exported during the simulated time period. However, at the beginning of the 21$^{\text{th}}$ century the sea ice transport is replaced by the liquid transport as the primary export mechanism of freshwater from the Arctic Ocean. The total transport of freshwater from sea ice is dominated by the the contributions from the Fram Strait and the Barents Sea, whereas

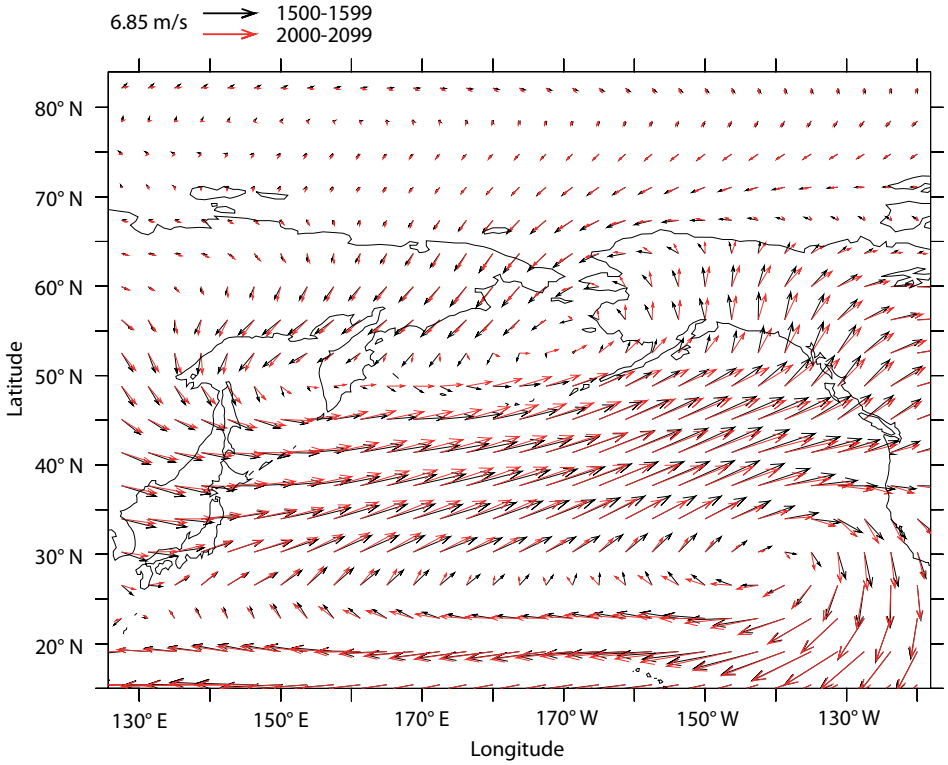

Figure 3.18: Ensemble average of the mean wind field over the North Pacific for the periods 1500-1599 and 2000-2099.

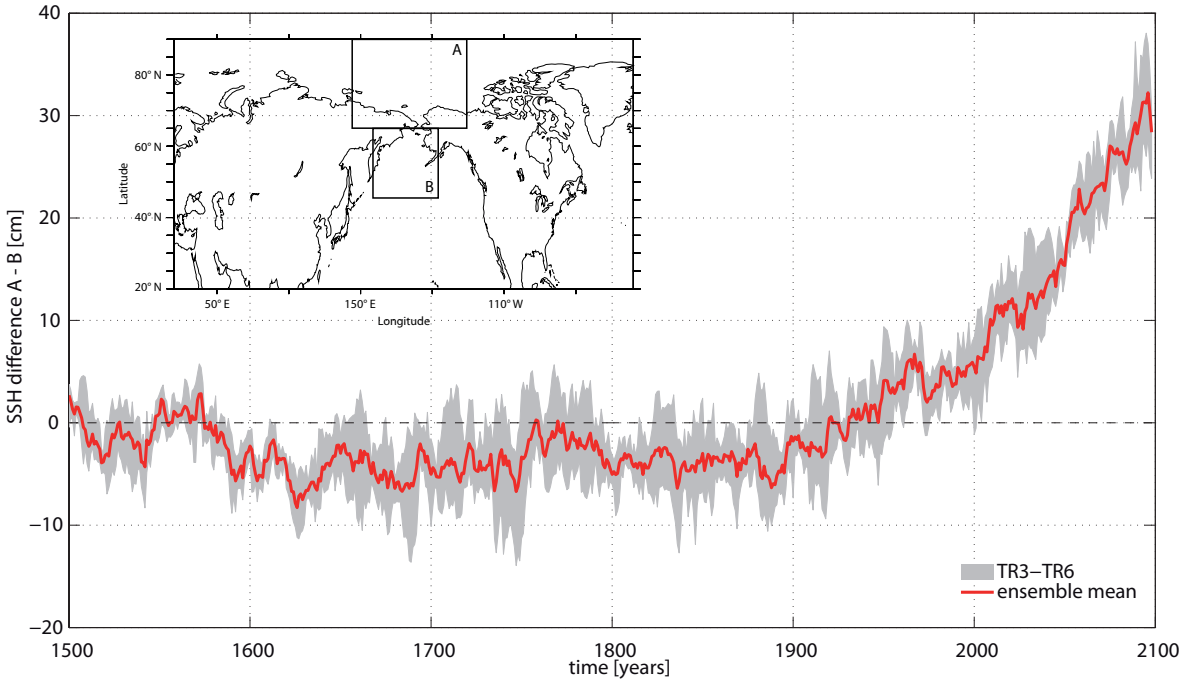

Figure 3.19: Sea surface height difference between the Arctic Ocean and the North Pacific, averaged over the areas defined in the small panel.

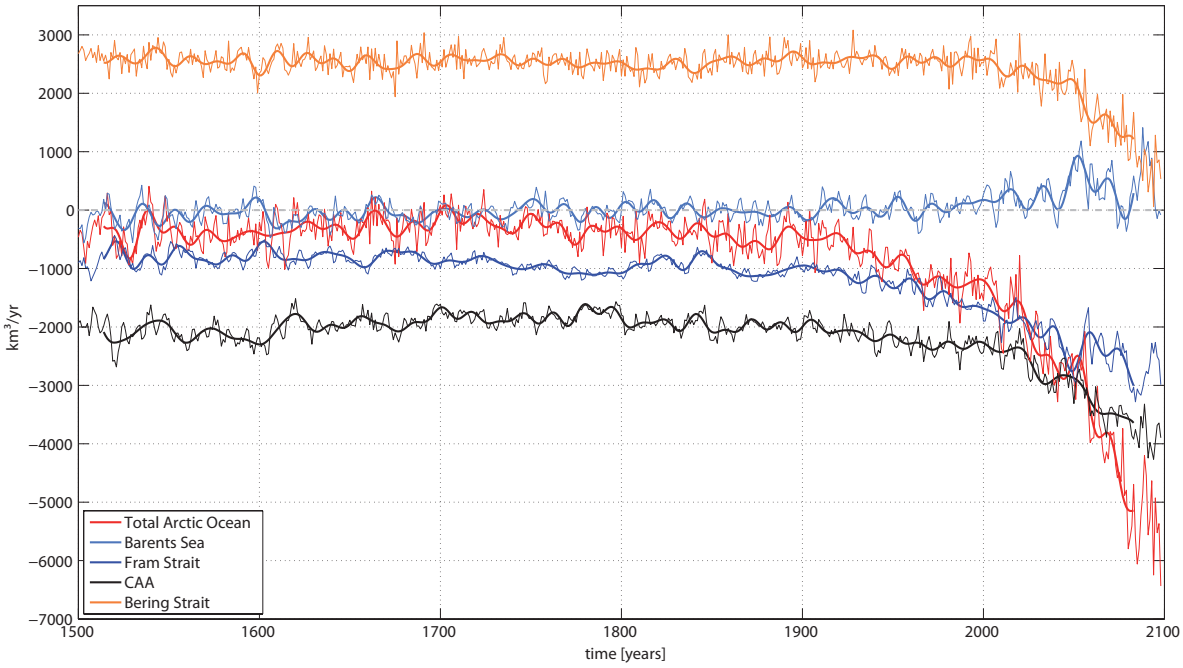

Figure 3.20: Ensemble mean liquid freshwater transport out and into the Arctic Ocean in $km^3\ yr^{-1}$ as total and subdivided in contributions from different straits. Thin lines denote annual means, thick lines 15-year low-pass filtered values. Negative values denote transport out of the Arctic Ocean.

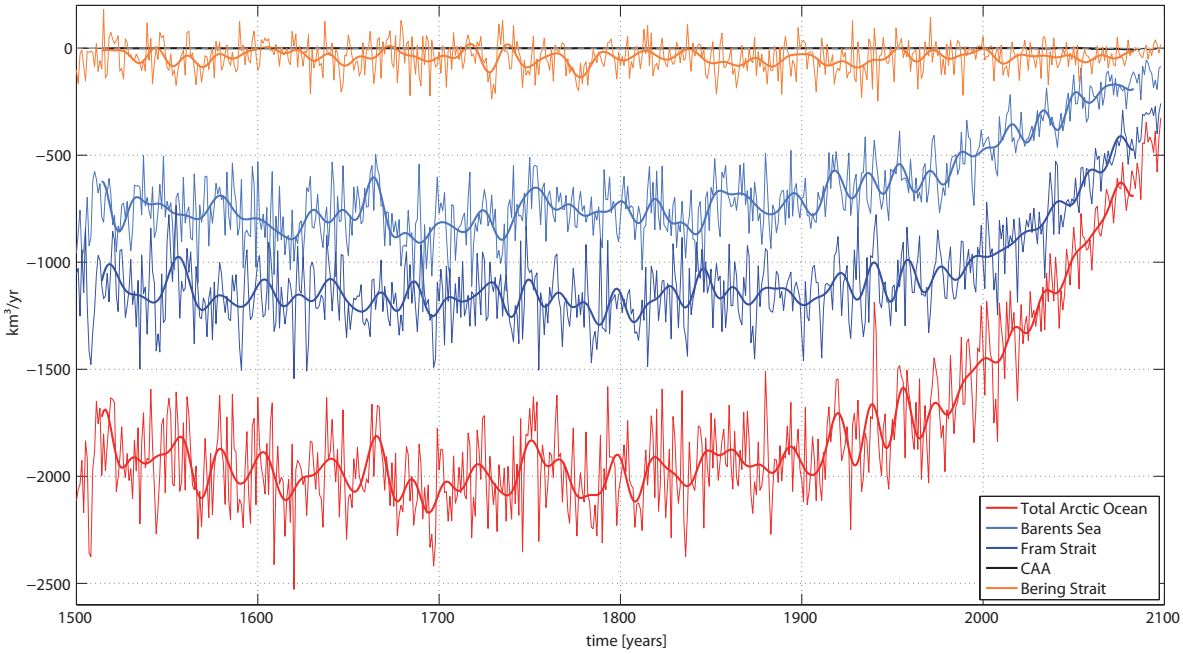

Figure 3.21: Ensemble mean solid freshwater transport out and into the Arctic Ocean by means of sea ice as total and subdivided in contributions from different straits. Units as in Fig. 3.20.

the CAA and the Bering Strait export only a small amount of sea ice. Reasons for this are discussed in section 3.4. The solid freshwater transport through the Fram Strait and Barents Sea is weakly anti-correlated ($R_a = 0.45$, ensemble mean from annual means) and responds without delay to the increase in greenhouse gas concentration. As the transport through all passages decreases, the total transport of sea ice drops drastically from approximately $-2{,}000$ km^3 yr^{-1} in the pre-industrial period to about -500 km^3 yr^{-1} at the end of the 21st century.

A large fraction of the liquid freshwater transport through the Fram Strait extends southwards via the East Greenland Current and passes through the Denmark Strait. This has been reported from both observations and model studies (e.g., *Karcher et al.*, 2005). In our simulations, the transports through the Fram Strait and the Denmark Strait show a high correlation, with the Denmark Strait exhibiting roughly four times larger values (Fig. 3.22). The correlation based on the annual means is highest at zero lag and at a lag of three to five years, this is, the Fram Strait is instantaneously correlated with the Denmark Strait, whereas it is also possible that the Denmark Strait leads the Fram Strait by three to five years. Looking at the pre-industrial period only, the correlations are weaker and the lag four to five years (average is 4.75 years). During the industrial period and into the future the correlations are high and the lag ranges from three to five years (average is 4.25 years).

As mentioned in section 3.2.2 the liquid freshwater content of the Arctic Ocean increases significantly during the 21st century and correlates well with the total freshwater transport out of the Arctic Ocean (Fig. 3.23). The correlation is, however, dominated by the synchronized increase in the industrial period. The highest correlations during the pre-industrial period yield only $R_a = 0.30$-0.47 and $R_f = 0.53$-0.81 while over the whole time period it is $R_a = 0.89$-0.90. The correlations during the pre-industrial period have a lag of two to five years, which means that the freshwater content of the Arctic Ocean leads the total freshwater transport. Several studies found that the sea surface height of the Arctic Ocean varies with the freshwater content and consequently can control the freshwater transport out of the Arctic Ocean when inducing a sea surface height difference between the Arctic Ocean and sub-polar basins (e.g., *Holland et al.*, 2006, *Koenigk et al.*, 2007, *Jahn et al.*, 2009). Here, this mechanism is addressed only for the Bering Strait transport (Fig. 3.19).

3.3.2 Deep water formation sites

As mentioned in the Introduction the global THC is mainly driven by high-density water masses which subside in areas of regional scale in the northern and southern high latitudes. According to Fig. 1.1 these areas of deep water formation (DWF) are considered to be in the GIN Seas, the Labrador and Irminger (LI) Seas, the Ross Sea and Weddell Sea. In this study the areas used to investigate the DWF were chosen according to the simulated hemispheric seasonal pattern of maximum mixed layer depth (Fig. 3.24), and the average mixed layer depth is used as a measure for DWF.

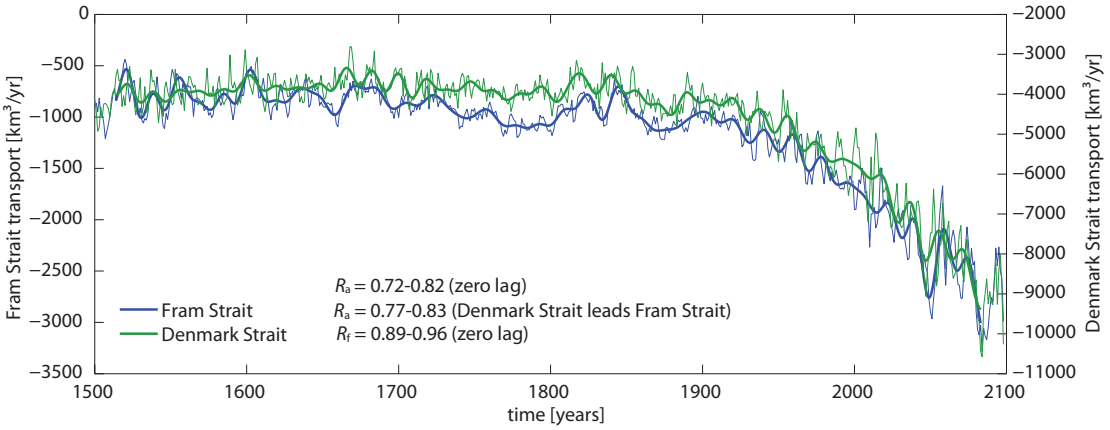

Figure 3.22: Ensemble mean liquid freshwater transport through the Fram Strait and Denmark Strait. Thin lines denote annual means, thick lines 15-year low-pass filtered values. Units as in Fig. 3.20. 'R_a' denotes the correlation of the annual means, 'R_f' the correlation of the filtered values.

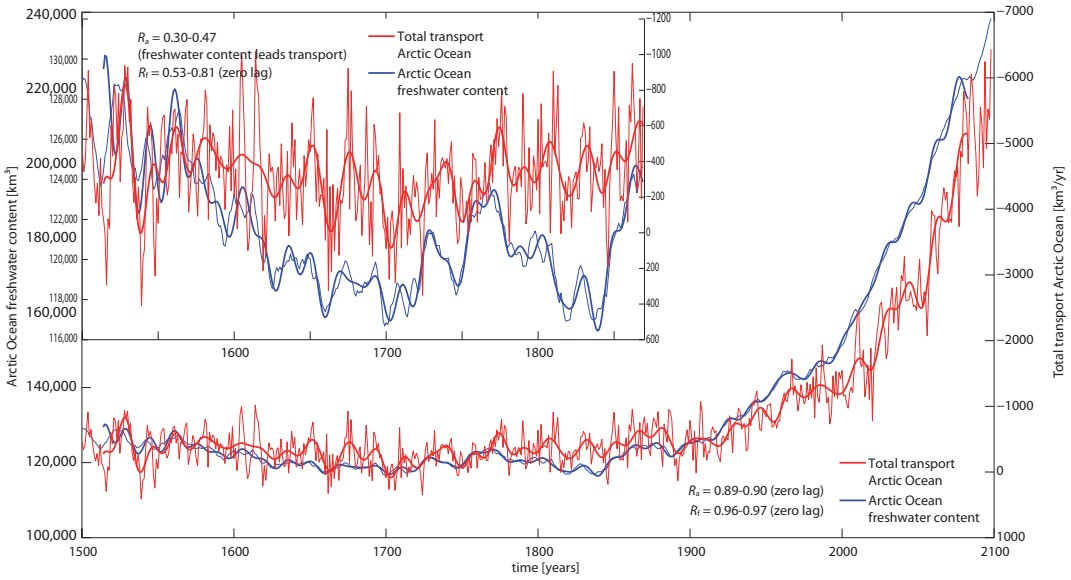

Figure 3.23: Ensemble mean total liquid freshwater transport out and into the Arctic Ocean in km^3 yr^{-1} and Arctic Ocean freshwater content in km^3. Thin lines denote annual means, thick lines 15-year low-pass filtered values. Note that the Y-axe for the total freshwater transport is inverted. Abbreviations as in Fig. 3.22.

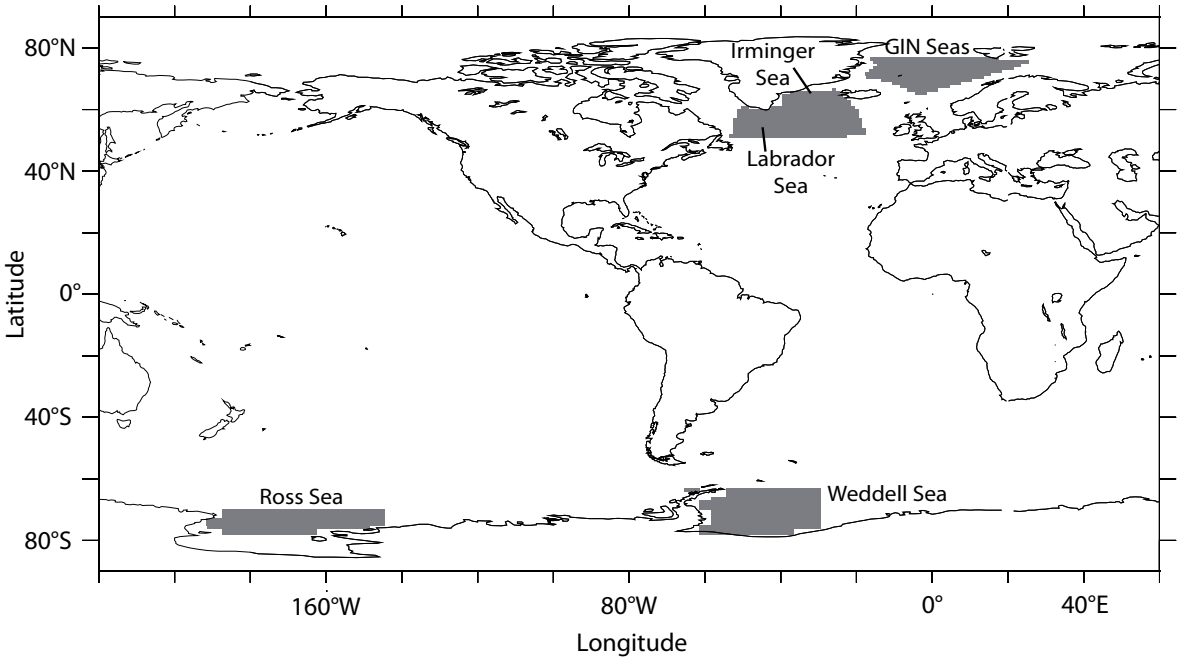

Figure 3.24: The areas of deep water formation as they occur in the CCSM3 T31x3 and are used in the following. Note that the areas are selected on the original grid and then regridded onto this regular grid and therefore do not form a rectangular shape here.

Northern Hemisphere

The model DWF sites of the Northern Hemisphere are positioned in the GIN and the LI Seas. A distinct characteristic of these two ocean regions is the direct freshwater supply from the nearby Fram Strait in case of the GIN Seas and the Denmark Strait and the CAA in case of the LI Seas. The liquid freshwater export through Fram Strait correlates best with the mean salinity of the top 104 meters of the GIN Seas at a lag of about two years ($R_a = 0.58$, ensemble mean), i.e., the liquid freshwater export through Fram Strait leads the GIN Seas upper-ocean salinity by two years. A similar situation is found in the LI Seas where the liquid freshwater transport through the Denmark Strait leads the upper-ocean salinity by about three years ($R_a = 0.50$, ensemble mean). The freshwater transport through the CAA is found to lead the LI Seas salinity by about three years as well. However, the correlation is sufficiently strong only for the TR3 ($R_a = 0.62$). The time series of the GIN Seas and LI Seas upper-ocean salinity and density are shown in Fig. 3.25 (a) and (b) and Fig. A.3 (a) and (b), respectively. The inter-annual variability of the salinity is large in both regions, whereby in the GIN Seas it even increases further during the 21st century. Salinity in the GIN Seas drops down to about 33 g kg^{-1} towards the end of the 21th century and leaves the range of the maximum spread of EQ1500. The upper-ocean salinity in the LI Seas does not show an increase in inter-annual variability. However, it decreases nearly linearly over the whole time series with a rate of approximately 0.048 g kg^{-1} per century. Natural variability indicated by the maximum spread of EQ1500 seems to be large, mainly because the LI Seas salinity of EQ1500 once decreases from approximately 34.4 to 33.7 within 15 years. It recovers at the same rate and remains a unique event throughout the whole EQ1500 time series. In contrast to the LI Seas, the GIN Seas upper-ocean salinity of EQ1500 shows a strong increase and

then decrease during that time, that is, being anti-correlated with the LI Seas salinity. It therefore is uncertain if the changes in upper-ocean salinity of the LI Seas can be attributed to external forcing alone. Further, temporary large spreads among the different transient runs were found for both regions (not shown), emphasizing the sensitivity of the upper-ocean salinity to perturbations in the freshwater forcing. While the upper-ocean salinity in the GIN and LI Seas remains curtly within the range of natural variability, the upper-ocean density does not. It changes more dramatically than the salinity and suggests that other parameters such as the ocean temperature may play a role in determining the density in the Northern Hemisphere DWF sites.

Compared to the upper-ocean salinity the mixed layer depths in the Northern Hemisphere regions of DWF do not show a significant trend throughout the time series and stay within the spread of EQ1500 (Fig. 3.26 (a) and (b)). In the GIN and LI Seas the ensemble mean mixed layer depths during the pre-industrial period are 105 ± 16 m and 106 ± 11 m, respectively. The ensemble means for the period 2068-2098 are 104 ± 12 m and 101 ± 9 m. After about 500 years in EQ1500 the LI Seas shows a strong and sudden lift of the mixed layer depth of more than 40 meters within about 15 years. This signal is temporally consistent with the massive drop in the LI Seas EQ1500 upper-ocean salinity described before. Indeed, the long-term correlation between the upper-ocean salinity and the mixed layer depth is highest at zero lag in both DWF sites and yields $R_a = 0.52$ and $R_a = 0.61$ for the GIN Seas and LI Seas, respectively.

Besides the ocean-internal freshwater transport mechanism, three external contributors of freshwater to the DWF sites can be considered: river runoff, $P - E$ and sea ice meltwater. Direct river runoff to the GIN and LI Seas is fairly small since the chosen regions only border on short coastlines (Svalbard in case of the GIN Seas, Greenland and Iceland in case of the LI Seas). Figs. A.1 (a) and (b) feature the corresponding time series. River runoff into the GIN Seas increases from 37 ± 4 $km^3\ yr^{-1}$ (pre-industrial) to 51 ± 4 $km^3\ yr^{-1}$ (2068-2098) and in the LI Seas from 198 ± 11 $km^3\ yr^{-1}$ (pre-industrial) to 227 ± 16 $km^3\ yr^{-1}$ (2068-2098). In comparison, the sea ice meltwater to these regions is roughly a magnitude larger than the river runoff. Additionally, there are dramatic changes projected for the contribution from sea ice meltwater in the GIN and LI Seas: In the GIN Seas the sea ice meltwater decreases from 1,625 ± 156 $km^3\ yr^{-1}$ (pre-industrial) to 693 ± 113 $km^3\ yr^{-1}$ (2068-2098) whereas in the LI Seas a even larger decrease from 3,284 ± 315 $km^3\ yr^{-1}$ (pre-industrial) to 870 ± 167 $km^3\ yr^{-1}$ (2068-2098) occurs (Fig. A.2 (a) and (b) in the Appendix A). The third and last ocean-external contribution of freshwater to the DWF sites comes from precipitation minus evaporation ($P - E$). In the GIN Seas $P - E$ is constantly negative, which means that the ocean loses freshwater to the atmosphere (Fig. A.4 (a)). $P - E$ denotes a weak linear upwards trend throughout the whole time series with no remarkable reaction to the increasing greenhouse gas concentrations. However, inter-annual variability increases slightly during the 21^{th} century. Changes between the pre-industrial period and 2068-2098 are approximately 38%. The LI Seas present a much different picture regarding $P - E$ (Fig. A.4 (b)). Here, the flux is always positive and acts as a source of freshwater to the upper-ocean in the LI Seas. Further, a clear signal from the increasing greenhouse gas concentrations is simulated. $P - E$ increases by over 88% from pre-industrial to 2068-2098 and exceeds the range of natural variability in all four transient runs.

Southern Hemisphere

In the southern high latitudes the Weddell Sea and the Ross Sea are the prominent sites of DWF (Fig. 3.25 (c) and (d) and Fig. A.3 (c) and (d)). Their long-term mean salinities are 34.3 and 34.2 g kg^{-1}, respectively. Both time series show a much smaller inter-annual variability and model spread than the Northern Hemisphere counterparts in the GIN Seas and LI Seas. The EQ1500 time series of the Weddell and Ross Seas both show a linear trend of 0.02 g kg^{-1} per century, which is an artificial trend superimposed to the ocean data as EQ1500 was not in perfect equilibrium when the transient runs were branched off (see section 2.2). In the Weddell Sea, salinity fluctuates within a range of $\pm$ 0.1 g kg^{-1} throughout the pre-industrial period. During the 20^{th} century, two sudden drops on the order of 0.1 and 0.05 g kg^{-1} within five years is simulated. Towards the end of the 20^{th} century the Weddell Sea salinity starts to decrease at an increasing rate and reaches minimal values of 33.6 g kg^{-1} at the end of the time series. The salinity in the Ross Sea shows a similar behaviour: after 400 years of stable salinity it starts to decrease at mid-20^{th} century and is reduced by 0.4 g kg^{-1} to 33.8 g kg^{-1} until the end of the 21^{st} century. During the 21^{st} century the salinity in both the Weddell and Ross Seas exceed the range of natural variability of EQ1500. The same hold true for the upper-ocean density which decreases in concert with the salinity. In contrast to the Northern Hemisphere DWF sites, ocean temperatures might be less important for the density changes in the Southern Hemisphere DWF sites. From this analysis it is shown that the salinity and especially the density in all four DWF sites experiences conspicuous changes as the atmospheric greenhouse gas concentrations increase.

Regarding mixed layer depth the two DWF sites in the southern high latitudes show different characteristics (Fig. 3.26 (c) and (d)). The ensemble mean mixed layer depths in the Weddell Sea during the pre-industrial period are 44 $\pm$ 3 m and in the Ross Sea it is 72 $\pm$ 3 m. The ensemble means for the period 2068-2098 are 48 $\pm$ 3 m and 55 $\pm$ 1 m, respectively. While the mixed layer depth in the Wedell Sea experiences no significant trend and is in the range of the variability of EQ1500, it shows a different behaviour in the Ross Sea. There, the mixed layer depth is lifted in concert with the decrease in upper-ocean salinity and increase in greenhouse gas concentrations from about mid-20^{th} century onwards. In the light of this finding it is surprising that the Weddell Sea does not show a similar reaction to the strong decrease in upper-ocean salinity and density as it is recorded in Fig. 3.25 (d) and Fig. A.3 (d).

In the southern high latitudes, the simulated runoff is dominated by continental ice sheet melting whereas sea ice meltwater originates from sea ice only. Consistent with the zonal averages for the southern high latitudes (see section 3.1) the runoff in the Weddell and Ross Seas increases throughout in the 21^{st} century (Fig. A.1 (c) and (d)). In the region of the Weddell Sea from 167 $\pm$ 12 km^3 yr^{-1} (pre-industrial) to 193 $\pm$ 12 km^3 yr^{-1} (2068-2098) and in region of the Ross Sea from 190 $\pm$ 14 km^3 yr^{-1} (pre-industrial) to 210 $\pm$ 13 km^3 yr^{-1} (2068-2098). However, for both regions the changes do not exceed the range of EQ1500. In the Weddell Sea the runoff shows no reasonable correlation with the mixed layer depth. In the Ross Sea, where runoff is slightly larger than in the Weddell Sea, a zero lag correlation of $R_a = -0.57$ exists between runoff and the mixed layer depth.

In contrast to the runoff, the freshwater flux to the ocean from sea ice meltwater in these two DWF regions is not always positive (Fig. A.2 (c) and (d)). In case of the Ross Sea it actually

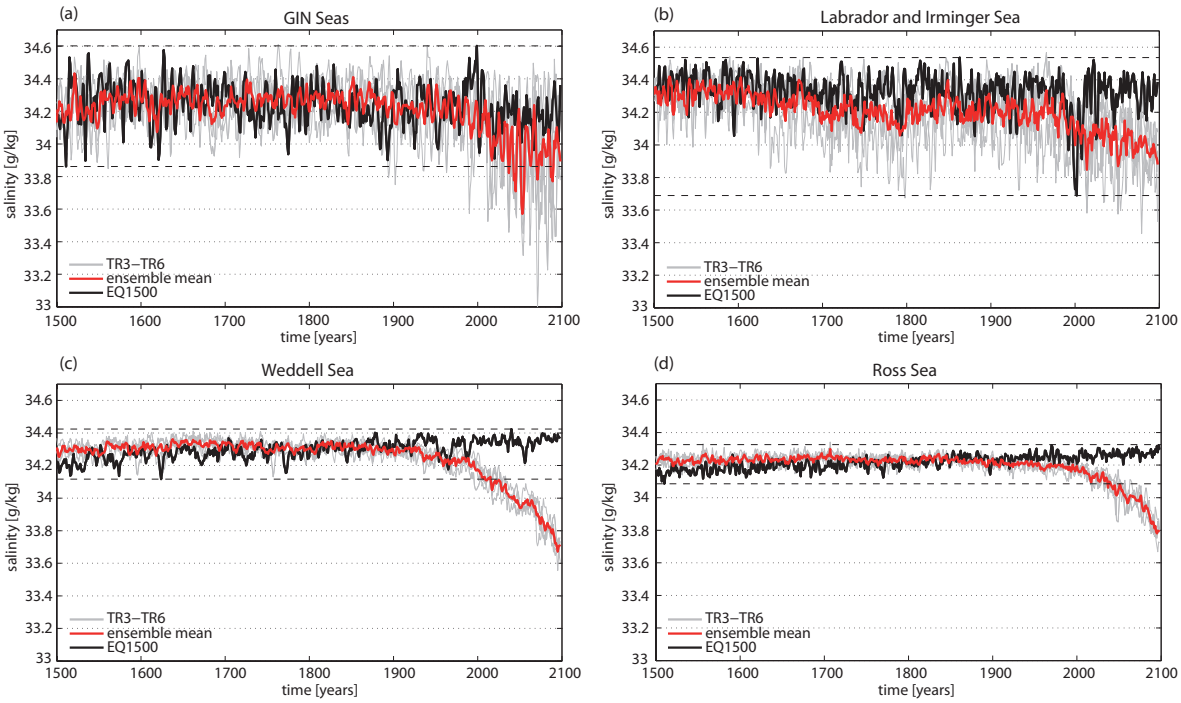

Figure 3.25: Temporal evolution of the annual mean salinity of the top 104 meters in the GIN Seas (a), Labrador and Irminger Sea (b), Weddell Sea (c) and Ross Sea (d), averaged over the areas defined in Fig. 3.24. Dashed black lines denote the spread of EQ1500.

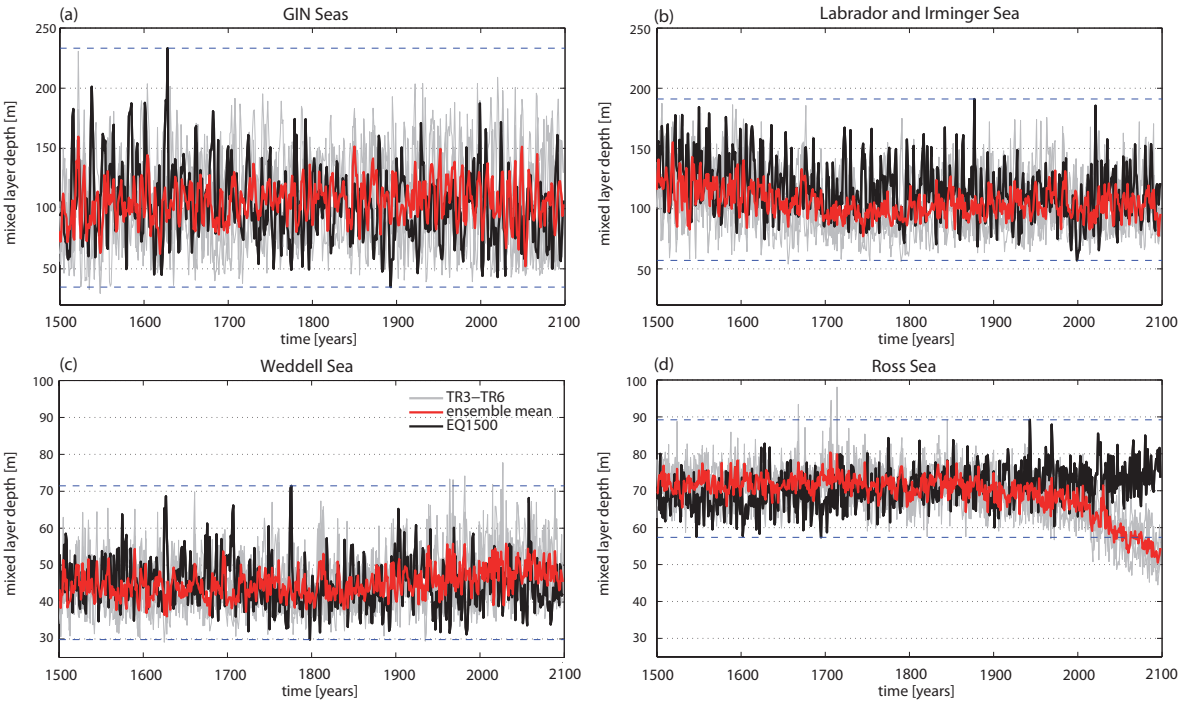

Figure 3.26: Temporal evolution of the annual mean mixed layer depth in the GIN Seas (a), Labrador and Irminger Sea (b), Weddell Sea (c) and Ross Sea (d), averaged over the areas defined in Fig. 3.24. Dashed black lines denote the spread of EQ1500. The legend in (c) is valid for (a), (b) and (d) as well.

is highly negative (-454 ± 50 km^3 yr^{-1} during the pre-industrial period) and has a future trend towards an even stronger negative flux (-563 ± 76 km^3 yr^{-1} for the period 2068-2098). This means that the Ross Sea is an area of constant sea ice building (annual range is approximately $-3{,}000$-$4{,}000$ km^3 yr^{-1}) and therefore acts as a sink for the Ross Sea freshwater budget. The Weddell Sea, which as well has a large seasonal range going from negative values in Southern Hemisphere winter to positive values in summer, is neither a sink nor a source in terms of net freshwater flux (9 ± 80 km^3 yr^{-1} during the pre-industrial period). However, as the greenhouse gas concentrations grow, the Weddell Sea sea ice meltwater flux turns into a freshwater source for the ocean, exhibiting a trend towards higher values (169 ± 104 km^3 yr^{-1} for the period 2068-2098). This increase is still within the range of EQ1500, nevertheless, a continuation of the trend into the 22$^{\text{nd}}$ century would clearly exceed the natural range. In the Weddell Sea small inter-decadal fluctuations of the sea ice meltwater flux to the ocean can inversely be recognized in the time series of the mixed layer depth. However, the significant correlation of both complete time series yields only $R_{\text{a}} = -0.27$ at zero lag. In the Ross Sea, where freshwater is net extracted from the ocean by the sea ice meltwater flux, the mixed layer depth leads the sea ice meltwater by three years, but again with a weak correlation ($R_{\text{a}} = 0.23$). To assess the details of the sea ice melting process an analysis of the ocean stratification and its dependence on mixed layer depth is necessary. A change in the Antarctic Circumpolar Current might alter the ocean stratification and enhance basal melting by advecting warmer waters (*Hattermann and Levermann*, 2010). However, ocean surface temperatures in this region were not found to increase noticeably during the 21$^{\text{st}}$ century.

$P - E$ in the two DWF sites of the Southern Hemisphere seem to balance each other which is in agreement with what was found for the whole region of 60-90° S (see section 3.1.3). Nevertheless, profound changes as response to the greenhouse gas forcing occur for $P - E$ as well. In the Weddell Sea $P - E$ increases from -19 ± 6 km^3 yr^{-1} (pre-industrial) to 21 ± 6 km^3 yr^{-1} (2068-2098) and therefore turns from a net sink to a source of freshwater for the upper-ocean (Fig. A.4 (c)). Thereby the frame of natural variability is left towards the end of the 21$^{\text{st}}$ century. In the Ross Sea changes are less dramatic, but $P - E$ still increases from -52 ± 8 km^3 yr^{-1} (pre-industrial) to -24 ± 6 km^3 yr^{-1} (2068-2098). In comparison to the Wedell Sea, the range of the Ross Sea $P - E$ of EQ1500 is larger and 21$^{\text{st}}$ century changes are still within that range.

3.3.3 Meridional Overturning

The Atlantic MOC is calculated as the Maximum Meridional Overturning north of 28° N and occurs on average at 32-33° N and in a depth of 800-1,000 meters. The long-term average of EQ1500 is 16.8 ± 1.1 Sv. Fig. 3.27 presents the annual mean Atlantic MOC for the transient runs as well as EQ1500. The transient runs show a incoherent behaviour. All four runs fluctuate within a narrow band during the first approximately 140 years, then TR6 drops to values beyond natural variability (maximum spread of EQ1500) and recover about 200 years later. TR5 shows a sharp rise at mid-17$^{\text{th}}$ century and then drops as well. Thirdly, TR4 decreases rapidly after about 1730. TR3 remains stable during this whole time. While around 1800 TR6 recovers to its initial strength, TR5 and TR4 continue at the low level they have stabilised at after their reduction. With the beginning of the 21$^{\text{st}}$ century all four transient runs weaken further and leave the range of natural variability. Note that the four transient

runs differ only in initial conditions whereas the physical forcing is identical. Compared to the mean of 1500-1530 the transient runs decrease by 17.6-23.2% until the end of the 21st century. Looking at EQ1500 in more detail, a drop of the Atlantic MOC occurs after about 500 model years, followed by a steep recovery to values around the long-term mean. This event appears synchronised with a massive drop and recovery in LI Seas upper-ocean salinity and a lift of the mixed layer depth in the same region. Further, the GIN Seas upper-ocean salinity increases remarkably during the same time.

To look into the event of a short-term drop in the EQ1500 Atlantic MOC between about 490 and 510 simulated years, normalized time series of the MOC, Fram Strait, Barents Sea, Denmark Strait and CAA freshwater transport, upper-ocean salinity and mixed layer depth of the Northern Hemisphere DWF sites are presented in Fig. 3.29 (a). It is visible that the upper-ocean salinity is highly correlated with the mixed layer depth in both the GIN and LI Seas, especially during this event. In case of the mixed layer depth a decreasing index actually equals a shoaling of the mixed layer. This correlation is highest at zero lag. The analysis of the interplay of the upper-ocean salinity in the GIN Seas with the Fram Strait liquid freshwater transport in the previous section revealed the Fram Strait transport to lead the GIN Seas salinity by about two years. This is not well visible in Fig. 3.29 (a), suggesting additional sources to influence the upper-ocean salinity at that time. Such might be $P - E$, sea ice meltwater or the combined freshwater forcing from the Fram Strait and Barents Sea. The latter indeed shows a better accordance with the salinity and mixed layer depth than the Fram Strait transport alone (upper panel in Fig. 3.29 (a)). However, the Fram Strait transport is in clear anti-phase with the GIN Seas salinity on basis of five-year filtered data (not shown) and might still be dominating the GIN Seas salinity on these short time scales. In the LI Seas, on the other hand, Denmark Strait transport leads the upper-ocean salinity by about four years. The CAA transport tends to peak shortly after the maximum values in Denmark Strait and so additionally strengthens the freshwater forcing to the LI Seas with a lag. This is especially well visible when the salinity and mixed layer depth index in the LI Seas drop massively between 490 and 510 years (lower panel of Fig. 3.29 (a)). During these drops in LI Seas salinity and mixed layer depth the MOC weakens as well.

A similar interplay cannot clearly be identified in the time series of the GIN Seas (upper panel of Fig. 3.29 (a)). However, correlations for the time period of 470 to 520 simulated years of the salinity and mixed layer depth of the GIN Seas with the MOC yield $R_a = 0.51$ and $R_a = 0.50$, respectively, at a lag of 11 years (upper panel of Fig. 3.29 (b)).

At a lag of 8 years the Fram Strait and Barents Sea transport is correlated highest with the MOC ($R_a = 0.60$). This means, that fluctuations in the strength of the MOC are significantly rediscovered in the Fram Strait transport, and in the salinity and mixed layer depth of the GIN Seas 8 and 11 years later, respectively.

The same analysis is conducted for the LI Seas (lower panel of Fig. 3.29 (b)). There, the best significant correlations between the Atlantic MOC and the LI Seas upper-ocean salinity were found at lags of +1 years ($R_a = 0.47$) and −10 years ($R_a = 0.47$). The same hold true for the correlations of the Atlantic MOC with the LI Seas mixed layer depth, where the best correlations are at lags +1 years ($R_a = 0.46$) and −10 years ($R_a = 0.42$) as well. This means that two modes seem possible: the MOC leads the LI Seas salinity and mixed layer depth by

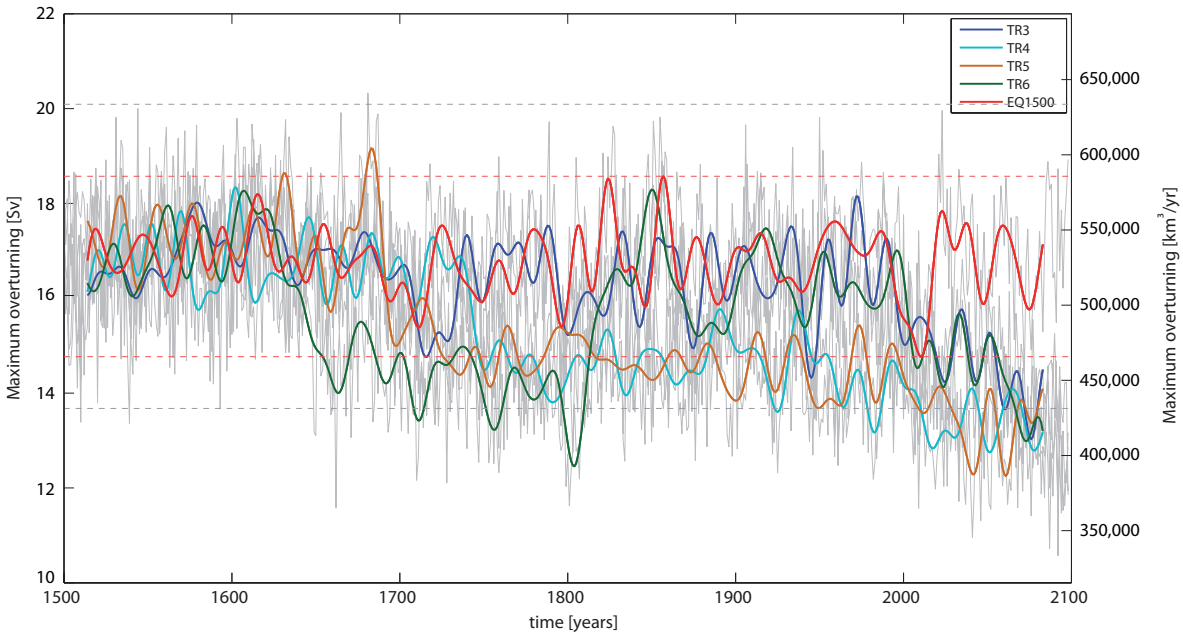

Figure 3.27: Maximum Meridional Overturning Atlantic north of 28° N in Sv and km^3yr^{-1} of the four transient runs and EQ1500. A 15-year filter (coloured) and the annual means (grey) are shown. The dashed lines denote the maximum and minimum of EQ1500 for its filtered (red) and unfiltered values (grey).

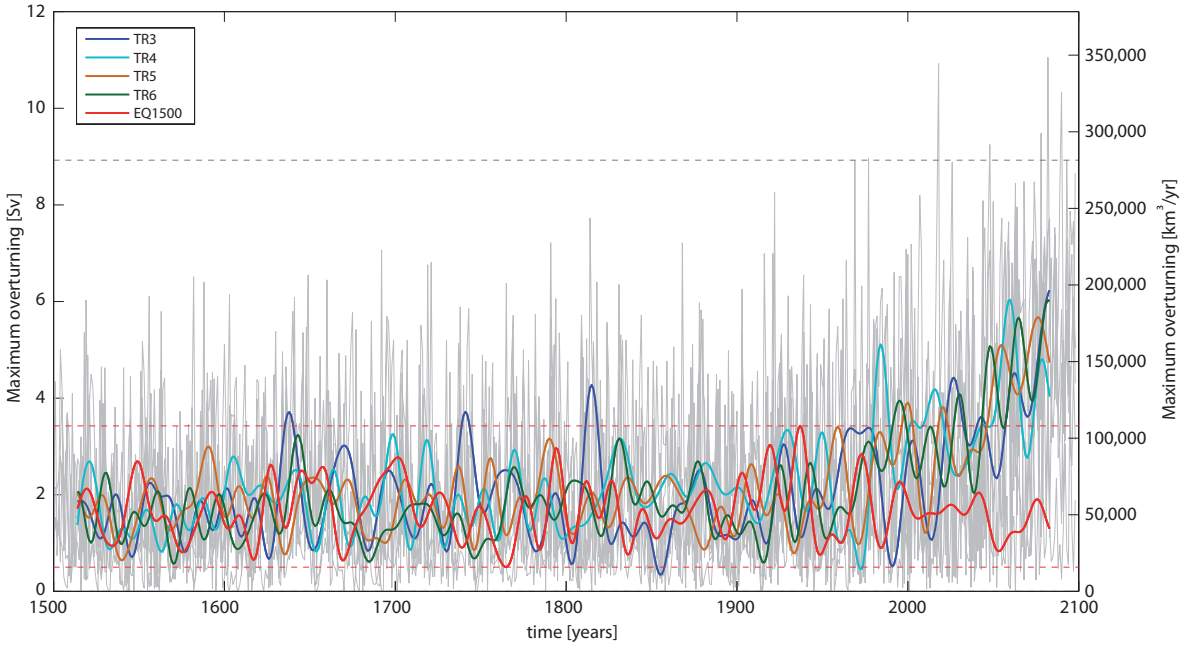

Figure 3.28: Maximum Meridional Overturning in the Southern Ocean south of 60° S in Sv and km^3yr^{-1} of the four transient runs and EQ1500. A 15-year filter (coloured) and the annual means (grey) are shown. The dashed lines denote the maximum and minimum of EQ1500 for its filtered (red) and unfiltered values (grey).

one year or the LI Seas salinity and mixed layer depth lead the MOC by ten years. As the LI Seas upper-ocean properties are directly influenced by the freshwater discharge through the Denmark Strait and the CAA, a signal of this freshwater discharge might be rediscovered in the MOC strength. However, the correlation of the Denmark Strait and CAA transport with the MOC is highest at zero lag ($R_a = 0.59$) and does not allow to attribute either the Denmark Strait and CAA transport or the MOC to lead the other quantity.

These results suggest that in the specific case presented here a weakening of the MOC can partly be explained by a preceded freshening of the LI Seas and accompanied shoaling of the mixed layer depth. These changes in the LI Seas upper-ocean properties are partly due to fluctuations in the freshwater forcing from the Denmark Strait and CAA transport, whereby the Denmark Strait's influence is more direct due to the proximity to the DWF site of the LI Seas. The GIN Seas, in contrast, seem to be dominated by the MOC, however, with a large lag of 8 to 11 years. How much of LI Seas salinity fluctuations can be explained by anomalous inflow of saline Atlantic waters as consequence of MOC variations and how these waters ultimately control the sea surface height difference between the GIN Seas and the Arctic Ocean remains to be assessed. After all, it became clear that the two DWF sites in the Northern Hemisphere not necessarily act in phase with each other.

The Southern Ocean Maximum Meridional Overturning is computed between the Antarctic continent and 60° S and is shown in Fig. 3.28. The long-term average of EQ1500 is 1.7 ± 1.4 Sv. Compared to the Atlantic MOC the four transient runs are within the natural variability of EQ1500 and do not taken different paths until the end of the 20th century. With beginning of the 21st century the transient runs consistently exhibit a strengthening of the Southern Ocean MOC. The inter-annual variability increases as well. The different runs show similar increase rates in the 21st century while the individual change in percent from the mean of 1500-1530 to 2068-2098 ranges from 145-211%. Looking at the filtered data, the transient runs clearly abandon the range of EQ1500. However, the natural variability of the Southern Ocean Overturning may include outliers as high as five times the long-term average (Fig. 3.28).

A schematic overview on the water fluxes between ocean basins and from land and atmosphere to the ocean is given in Fig. 3.30 and illustrates the results in the 21st century. It exhibits nicely the geographical differences between the northern and southern high latitudes as well as the consequences for the water cycle. The relative size of the symbols allows to place the regional changes in a global context when comparing the two time periods 1500-1870 and 2068-2098. Whereas the region around Antarctica loses freshwater the freshwater storage in the Arctic Ocean grows. However, by the present analysis it is not possible to determine whether the Arctic Ocean gains freshwater only at the expense of the Antarctic region or if the anomalous freshwater of the Arctic Ocean originates from Northern Hemisphere sources alone. Nevertheless, the largest part of the increased freshwater content in the Arctic Ocean comes from river runoff.

In the southern high latitudes the oceanic freshwater content is controlled by several mechanisms as well. The runoff from the Antarctic changes only little and is therefore considered nearly stable on the time scale of this study. On the other hand, the total oceanic export of freshwater increases despite decreasing sea ice export. This finding is supported by an strengthening of the Meridional Overturning at 60° S, but atmospheric circulation patterns

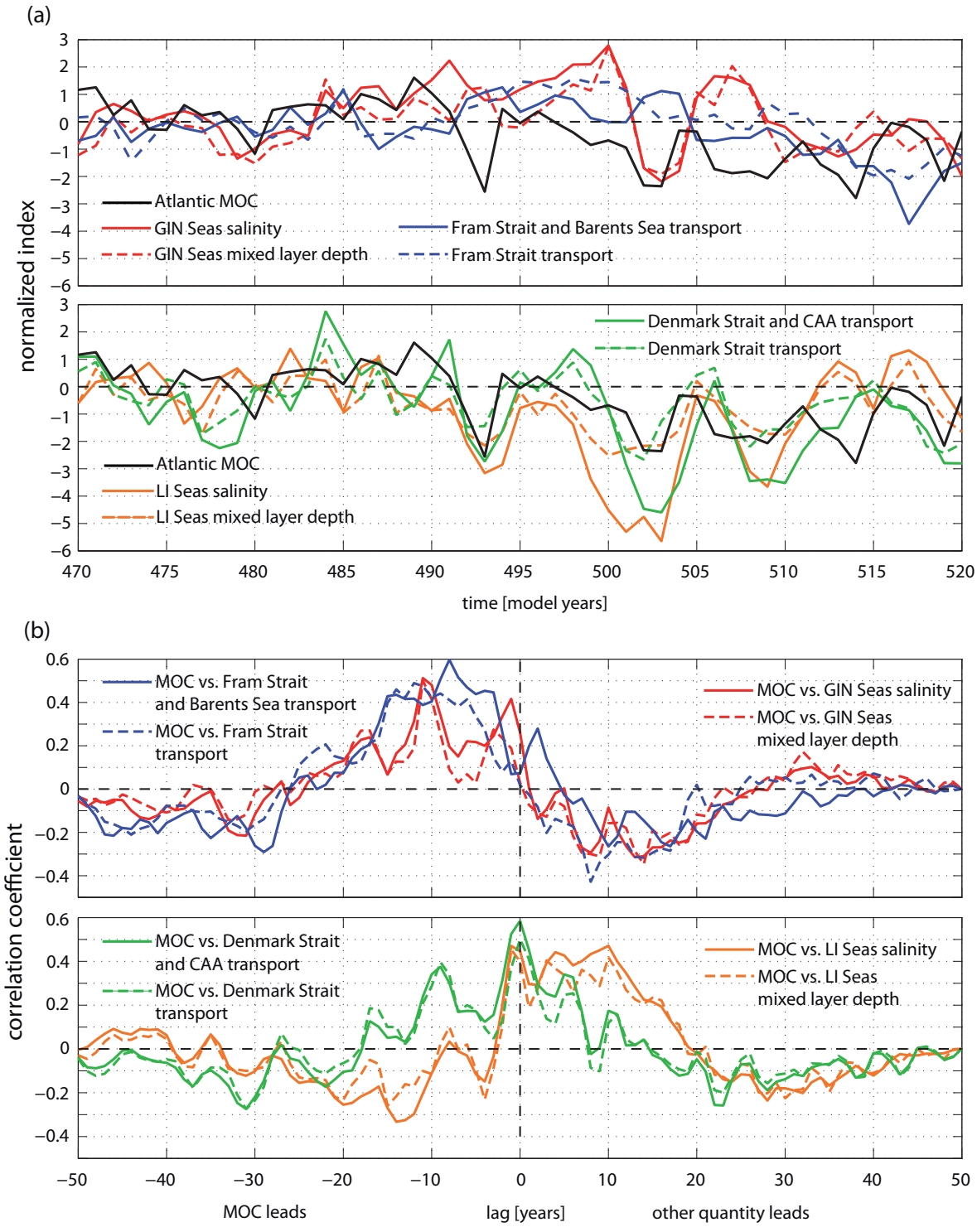

Figure 3.29: Normalized time series (for calculation see equation (2.32)) of the EQ1500 Atlantic MOC, LI Seas and GIN Seas upper-ocean salinity and mixed layer depth, and the Fram Strait and Denmark Strait liquid freshwater transport (a) and lag correlations for the same time period of the Atlantic MOC with LI and GIN Seas salinity and mixed layer depth, and with the Fram Strait and Denmark Strait liquid freshwater transport (b).

might play a role in this too. At the same time the net freshwater input to the ocean south of 60° S from precipitation minus evaporation increases as well. These two mechanisms of atmospheric input and oceanic export are the major source and sink of freshwater of the region. A growing imbalance of the in- and export of freshwater by these two mechanism might alter the freshwater content of the Antarctic region. A freshening of the upper-ocean and a lift of the mixed layer depth at the DWF sites are possible first consequences from this.

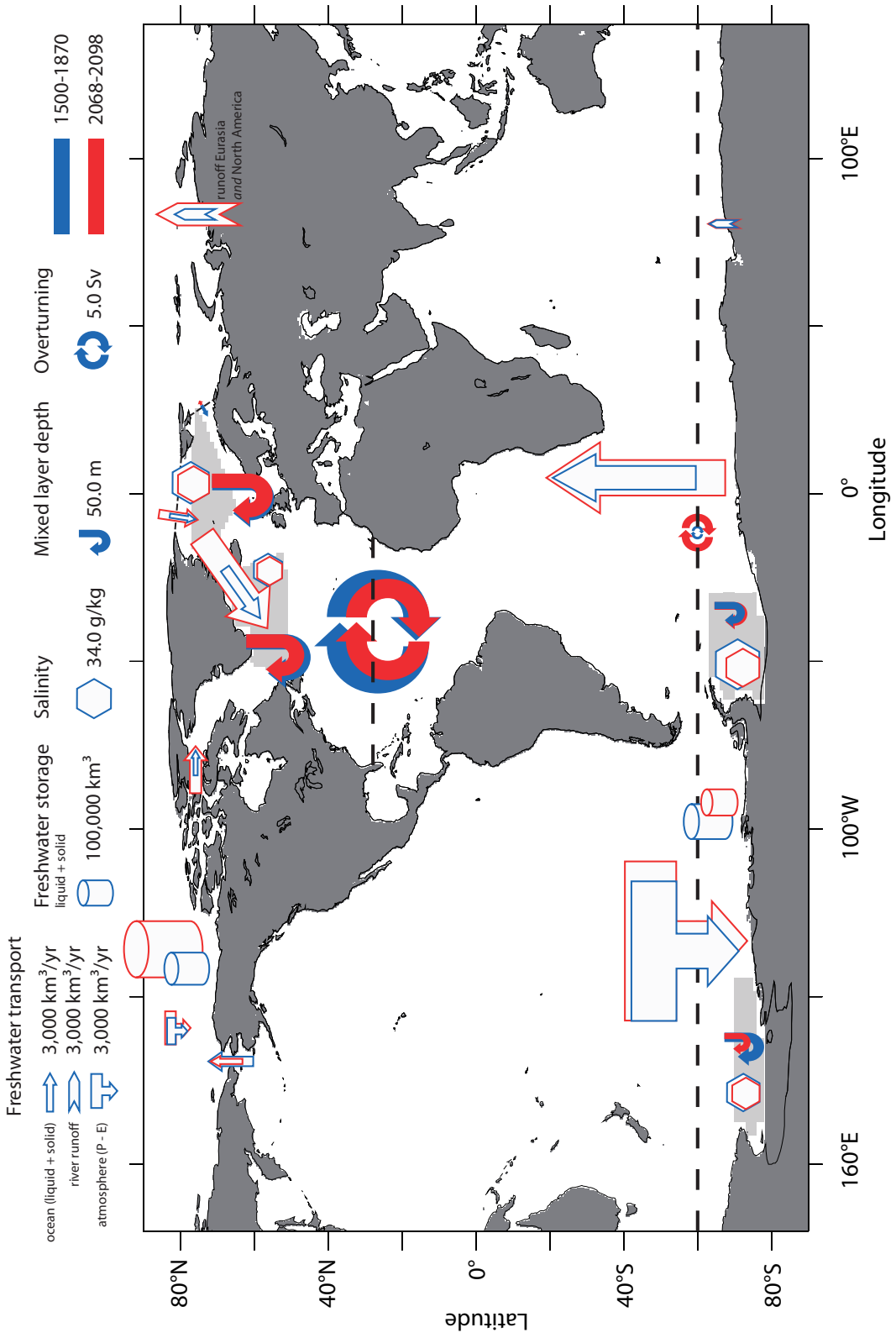

Figure 3.30: Overview on water fluxes between basins and between the system components land, ocean, atmosphere. Quantities and units as given in the figure. The size of every symbol is relative to the reference at the figure side. Atmospheric freshwater flux is given as total over the ocean area. Domains are the Arctic Ocean and 60-90° S. Transects for the Meridional Overturning are at 28° N and 60° S.

3.4 Comparison with observations and other models

Despite large efforts in observing the climate in the polar regions the spatial and temporal coverage of measurements is still sparse due to difficult accessibility, especially during winter months. Nevertheless, a comparison of the model output with the World Ocean Atlas (WOA, *Antonov et al.*, 2006) and the Version 3.0 University of Washington Polar Science Center Hydrographic Climatology (PHC, *Steele et al.*, 2001) is undertaken with respect to sea surface salinity (SSS) of the Arctic region (Fig. 3.31). Results from a modeling study and a model-intercomparison study (*Holland et al.*, 2006 and *Holland et al.*, 2007, respectively) are considered to evaluate the representation of the freshwater budgets in the CCSM3. Regarding river runoff and freshwater flux to the Arctic Ocean, observations and model results are taken from *Peterson et al.* [2002] and *Wu et al.* [2005], respectively. In the Antarctic region, a reanalysis of moisture budgets serves as a reference (*Tietäväinen and Vihma*, 2008).

In the Arctic region the model is able to reproduce the fresh shelf conditions arising from the shallow water and the river runoff into those, although the detailed spatial pattern is not captured very well (Fig. 3.31, (a)-(c)). In the Barents Sea, GIN Seas, Labrador Sea, Baffin Bay and off the south-eastern coast of Greenland, the model tends to be too fresh. This underestimation mainly arises from the fact that the model at the resolution T31x3 produces conditions in the Arctic that are too cold compared to observations. This is largely

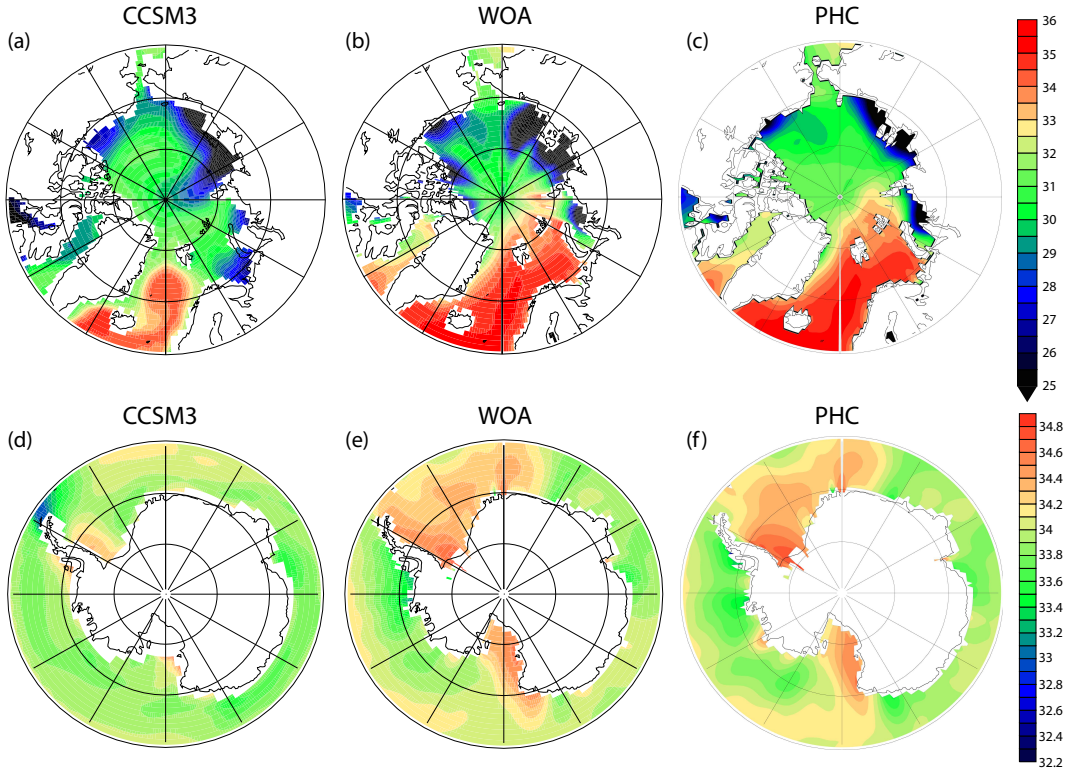

Figure 3.31: Sea surface salinity (SSS) in PSU in the Arctic and Antarctic region, model output averaged from 1990-1999 (a) and (d), from the World Ocean Atlas (WOA) (b) and (e) and the Polar Hydrographic Climatology (PHC) observations (c) and (f).

due to an underestimation of the heat flux through Bering Strait and Barents Sea (*Yeager et al.*, 2006). Along with this the sea ice extends further to the south, which results in an anomalous freshwater delivery to the basins. Additionally, the modeled sea ice covers larger areas, suppressing evaporation from the ocean surface and therefore freshens the ocean. This problem is greatly reduced if the model is run at T85x1, as was shown by *Holland et al.* [2006].

Holland et al. [2007] examined the performance of eight models in the Arctic region, including the CCSM3 at T85x1. Most of the models seem to capture the saline conditions in the Barents Sea and Baffin Bay better than the CCSM3 at T31x3. However, some of them fail to correctly reproduce the pattern of the fresh shelf waters and the average central Arctic Ocean salinity of approximately 31 g kg^{-1}. Note that only two of the eight investigated models feature a passage through the CAA and that the resolution varies greatly among the models.

In the Antarctic region the model generally tends to be too fresh as well. It is able to simulate the saline areas of the Weddell Sea and Ross Sea whereby it underestimates the amplitude by about 0.2 g kg^{-1}. Furthermore, the model produces a patch of very fresh water at the northern end of the Antarctic Peninsula which has not been observed in reality. The explanation for the mentioned deviations from observations may again lie in the model's excessive sea ice production due to a cold bias.

Serreze et al. [2006] published a comprehensive review of the large-scale freshwater cycle of the Arctic Ocean and the adjacent land masses based on recent observations. They subdivided the cycle into atmospheric, oceanic and terrestrial freshwater fluxes and storage capacities. The study features data collected mainly in the 1980s and 1990s. Note that *Serreze et al.* [2006] focus on the Arctic Ocean basin only, while Fig. 3.12 covers 60-90° N. Table 3.2 lists the estimates by *Serreze et al.* [2006] and the multi-model study by *Holland et al.* [2007] as well as the ensemble mean values obtained in this study for the Arctic Ocean basin and for the larger region of 60-90° N.

Moreover, table 3.3 compares the estimates by *Serreze et al.* [2006] and *Holland et al.* [2007] as well as this study's ensemble mean values for the liquid and solid freshwater transport through the four passages surrounding the Arctic Ocean obtained in this study. The total export of freshwater through the Fram Strait and the CAA is underestimated considerably, which might be due to the excessive sea ice production in the T31x3 resolution of the CCSM3: a sea ice-covered ocean area is less exposed to surface wind stress which is considered to strongly influence the export of water masses through the Fram Strait and the CAA (this problem occurs in other models as well, e.g., *Jahn et al.*, 2009). Therefore, the influence of atmospheric circulation modes on the export of liquid freshwater from the Arctic may be underestimated in this study. Additionally, the CAA is represented only coarsely in the model and therefore features a passage width of only one active grid cell. This might also explain the small value of solid freshwater transport through the CAA (average around 0, maximum at -100 km^3 yr^{-1}). The CCSM3 at T85x1 resolution and the MIROC3.2 in *Holland et al.* [2007] underestimates the freshwater transport through the CAA as well. The simulated overestimation of the Barents Sea freshwater transport clearly arises from the sea ice excess as the observations by *Serreze et al.* [2006] do not report any transport by sea ice at all for this area. The Bering Strait transport, in contrast, is in excellent agreement. The transport through the Denmark Strait (not shown in Table 3.3) is commonly given as absolute water

Table 3.2: Freshwater budgets in the Arctic region. Fluxes in $km^3\ yr^{-1}$, stores in km^3. Fluxes leaving the Arctic Ocean are negative.
*Note that *Holland et al.* [2007] feature no transport through the CAA.

study	*Serreze et al.* [2006]	*Holland et al.* [2007]	CCSM3	CCSM3
averaging period	∼1980-2000	1980-1999	1970-2000	1970-2000
region	Arctic Ocean	Arctic Ocean	Arctic Ocean	60-90° N
precipitation	**3,300**	**2,411**	**3,269**	**20,579**
— to ocean	—	—	311	2,863
— to ice	—	—	2,958	17,716
evaporation	**−1,300**	**−868**	**−766**	**−2,523**
— from ocean	—	—	−220	−850
— from ice	—	—	−546	−1,673
runoff	**3,200**	**3,162**	**3,417**	**5,423**
— ocean in liquid	3,250	−2,339	—	—
— ocean out liquid	−6,700	−3,727*	—	—
ocean net liquid	**−3,450**	**−1,388***	**−1,964**	**−8,159**
ocean out solid	**−2,460**	**−1,841***	**−2,051**	**−1,714**
imbalance ocean	**−710**	**1,476***	**1,905**	**13,606**
storage atmosphere	200	—	41	200
storage ocean	74,000	47,756	147,079	170,591
sea ice storage	10,000	13,851	29,785	36,177

volume transport rather than as freshwater transport. Simulated values range between 2.5 and 3.0 Sv and agree well with observations and other model results (*Käse et al.*, 2003).

The simulated values for total precipitation over the Arctic Ocean basin are in very good agreement with the observations, but it is not possible to compare the amount of freshwater that directly reaches the ocean surface by precipitation. Since the model tends to overestimate the sea ice area (*Kiehl et al.*, 2006), the simulated value of precipitation to the ocean surface of 311 km^3 might be too low. Following this, the underestimation of evaporation can be interpreted as an artefact of the too cold conditions at the poles: the large sea ice area inhibits the ocean to evaporate, whereas the sea ice has a much lower evaporation rate than the ocean surface. Runoff is in excellent agreement, pointing out the importance of a highly resolved river transport model. The oceanic net liquid outflow calculated from equation (2.30) is underestimated by over 40% compared to observations. *Holland et al.* [2006] simulated values between 3,000 and 4,000 $km^3\ yr^{-1}$, using the CCSM3 at T85x1 and with a more complete set of forcing parameters (*Meehl et al.*, 2006). The model-intercomparison study by *Holland et al.* [2007] yields a mean ocean net liquid outflow of 1,388 $km^3\ yr^{-1}$ and a mean solid outflow of 1,841 km^3. It is mentioned again that these results do not include transport through the CAA and that inter-model standard deviations for these transports are nearly as big as the transports themselves. The export of sea ice modeled in the present study is surprisingly close to observations. It seems that the overestimation of sea ice does not result

Table 3.3: Annual mean freshwater flux through oceanic straits delimiting the Arctic Ocean. Fluxes in $km^3\ yr^{-1}$. Fluxes leaving the Arctic Ocean are negative.
*Note that *Holland et al.* [2007] features no transport through the CAA.

study averaging period	*Serreze et al.* [2006] ∼1980-2000	*Holland et al.* [2007]* 1980-1999	CCSM3 1980-2000
Fram Strait			
total	**−4,710**	**−4,468**	**−2,646**
in liquid	500	—	—
out liquid	−3,160	—	—
— net liquid	*−2,660*	*−3,093*	*−1,619*
out solid	−2,300	−1,375	−1,027
Barents Sea			
total	**−90**	**−1,043**	**−420**
in liquid	250	—	—
out liquid	−340	—	—
— net liquid	*−90*	*−634*	*90*
out solid	—	−409	-510
Bering Strait			
total	**2,500**	**2,282**	**2,534**
in liquid	2,500	2,339	2,554
out solid	—	−57	−20
CAA			
total	**−3,360**	—	**−2,309**
out liquid	−3,200	—	−2,309
out solid	−160	—	∼ 0
total	**−5,660**	**−3,229**	**−2,841**

in an anomalous export of the ice to lower latitudes. The oceanic imbalance in terms of net freshwater flux is observed to be about 700 km^3 or ∼8% of the total estimated inflow and judged as "indistinguishable from zero" by *Serreze et al.* [2006]. The CCSM3 shows a larger imbalance of 1,905 km^3. This continuous positive imbalance might also be the reason for the heavily overestimated freshwater content in the Arctic Ocean, which would also be consistent with the too fresh conditions in the Arctic region displayed in Fig. 3.31. The considerably low atmospheric moisture content might again be due to the too cold conditions simulated by the model.

The simulated values for the river runoff into the Arctic Ocean from the Eurasian watershed are overestimated by the CCSM3 as well as by the HadCM3 (Fig 3.32). However, the timing and amplitude of the data compare very well to the observations. The trend of the CCSM3 tends to be too large, but is just within the uncertainty of the observations whereas the HadCM3 is closer to observations. Regarding the total river runoff to the Arctic Ocean, the

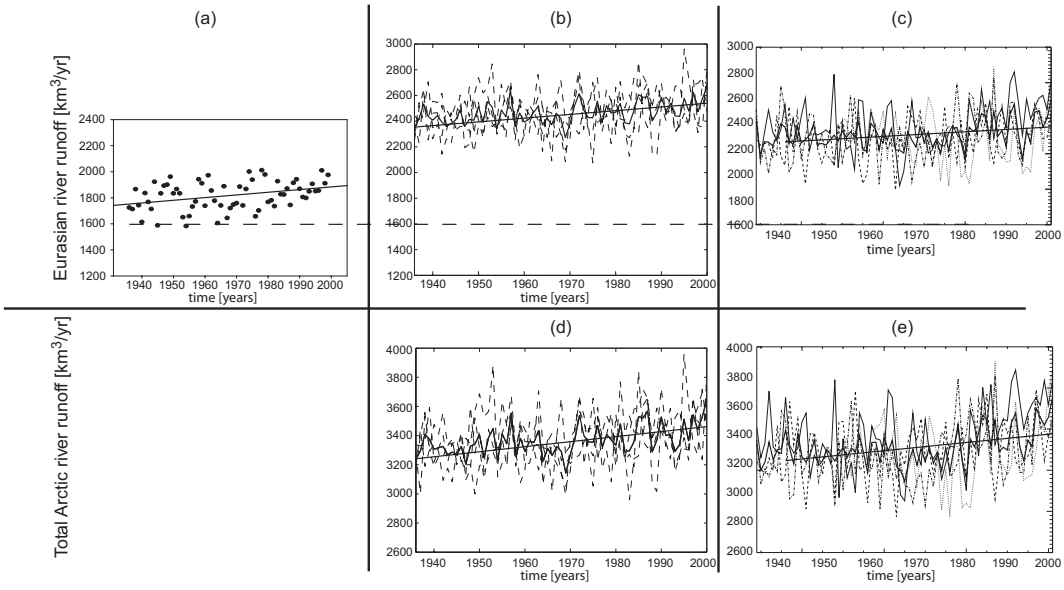

Figure 3.32: Annual river runoff into the Arctic Ocean from the Eurasian watershed (see Fig. 1.3) from observations by *Peterson et al.* [2002] (a), the CCSM3 (b) and the HadCM3 from *Wu et al.* [2005] (c). Annual river runoff into the Arctic Ocean from all Arctic rivers from the CCSM3 (d) and the HadCM3 (e). In (b)-(e) the dashed lines indicate different ensemble members while the solid line is the ensemble mean. All trend lines are from 1936-1999: 2.0±0.7 km^3 yr^{-1} per year (a), 2.7 km^3 yr^{-1} per year (b), 1.8 km^3 yr^{-1} per year (c), 3.0 km^3 yr^{-1} per year (d), 2.8 km^3 yr^{-1} per year (e).

two models are in closer agreement for both absolute values and trend.

Tietäväinen and Vihma [2008] recently analysed the atmospheric moisture budget over Antarctica based on the ERA-40 reanalysis. The pattern of meridional moisture transport at 60-90° S is compared to the CCSM3 output in Fig. 3.33. The transport over the ice sheet is well reproduced by the model with somewhat too small values in the area of the Ross Shelf. Over the ocean the general pattern of southward transport is also simulated well by the model, whereby the northward gradient off the coast of Wilkes Land is slightly underestimated. According to *Tietäväinen and Vihma* [2008] the Antarctic Peninsula acts as a barrier separating southward transport on its western side from northward transport on its eastern side. This pattern is also recognisable in the model output. Precipitation to and evaporation from the ice sheet are overestimated by the model compared to different reanalysis studies, as listed in Table 3.4. This can partly be explained by the slightly overestimated meridional moisture transport, since this quantity dominates the mean circumpolar convergence and, following from that, the net precipitation of the region.

The MOC represents another quantity which lacks robust measurements over time. The relatively recent attempt by *Cunningham et al.* [2007] estimates the Atlantic MOC to be 18.7 ± 5.6 Sv on basis of daily data. The long-term ensemble mean Atlantic MOC in this study here is 15.6 ± 0.7 Sv on basis of annual means. The ensemble mean for the period 1970-2000 does not differ significantly from the long-term mean (15.4 ± 0.6 Sv) and is somewhat too weak as well compared to the observations. In a CCSM3 T31x3 control experiment with perpetual 1870 forcing *Bryan et al.* [2006] found the Atlantic MOC to be at a very similar

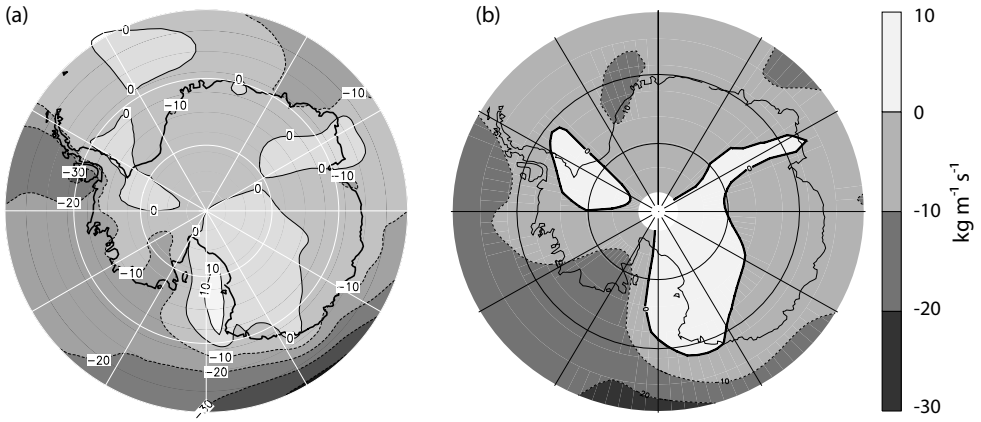

Figure 3.33: Annual meridional moisture transport at 60-90° S in kg m^{-1} s^{-1} for the period 1979-2001, modified from *Tietäväinen and Vihma* [2008] (a) and this study (b). Contour interval is 10 kg m^{-1} s^{-1} and negative values indicate southward water vapour transport. The colour bar is valid only for (b).

Table 3.4: Estimates of precipitation (P) and evaporation (E) in mm yr^{-1} over the Antarctic continental ice sheet from *Tietäväinen and Vihma* [2008], *Monaghan et al.* [2006], *Bromwich and Fogt* [2004] and CCSM3. Data source and averaging period are given.

study	data source	time period	P	E
Tietäväinen and Vihma, 2008	ERA-40	1979-2001	177 ± 8	25 ± 1
Monaghan et al., 2006	ERA-40, NCEP-2, MM5	1985-2001	183	—
Bromwich and Fogt, 2004	ERA-15, NCEP-2, ECMWF TOGA	∼1979-2000	188 ± 15	29 ± 1
this study	CCSM3 CLM2	1970-2000	245 ± 2	29

level as this study. When comparing the different resolutions of the CCSM3, they discovered the T31x3 to have the weakest MOC while T85x1 produces the highest (∼21.8 Sv). The standard deviation of the MOC increases as well with the model resolution. Generally, the mean MOC, its variability on decadal time scales, the rate of decrease under increasing greenhouse gas forcing and the rate of recovery when greenhouse gas forcing is stabilized all increase along with the model resolution (*Bryan et al.*, 2006). Therefore, this Atlantic MOC of the CCSM3 is considered to be at the lower end regarding absolute values and sensitivity. The simulated large range of Atlantic MOC strength among the different transient runs is a know feature of this and other models. *Yoshimori et al.* [2009] used the CCSM3 at T31x3 and provided some of the simulations used for this study. The found a similar variety of different transient runs and concluded that the simulated MOC does not directly respond to external forcing but rather reacts when a certain threshold is reached by a complex interplay of different parameters. A reason for the weak Atlantic MOC in the T31x3 resolution might be the inadequate representation of the DWF sites: the T31x3 lacks a band of deep mixed layers along the Greenland-Iceland-Scotland ridge (*Bryan et al.*, 2006). The T31x3 resolution further features lower densities than the other resolution versions and the DWF site south of Greenland is situated more to the East. The reasons for these differences are traced back

to the sea ice excess in the T31x3 resolution, as a anomalous sea ice coverage constrains the area where DWF is possible (*Bryan et al.*, 2006, *Yeager et al.*, 2006).

3.5 Discussion

The present study aimed at investigating the polar freshwater cycle, its components and their response to changing forcing parameters. The question, whether solar and volcanic forcing can significantly alter the water cycle in polar regions was addressed as well as what the response of the water cycle to prescribed rising greenhouse gas concentrations might be. A further goal was to determine the role of the river runoff in changing the Arctic Oceans freshwater budget in a warming climate. Finally, we tried to detect response mechanisms through which the changing freshwater cycle in polar regions (in particular the Arctic Ocean) potentially influences sub-polar waters and ultimately the Atlantic MOC. These projections are based on the IPCC SRES A2 scenario.

3.5.1 Summary of main results

We found the freshwater flux to the tropical ocean and the high northern and southern latitudes to increase strongly, the subtropical and lower mid-latitudinal oceans tend to obtain less freshwater. The increase in the northern high latitudes is stronger than in the high southern. The inter-annual variability is high, and significant fluctuations, potentially induced by variations in the solar forcing (such as the Maunder Minimum or the Dalton Minimum around 1800), cannot be detected for the domains 60-90° N and 60-90° S. Regarding the volcanic forcing it was discovered that the hydrological parameters of the domains 0-60° N and 0-60° S show some significant response to large eruptions (not shown in this study). This signal weakens towards the poles and becomes untraceable in the areas north and south of 60° N and 60° S, respectively. Additional analysis techniques might reveal more details on this topic.

The annual cycle of the freshwater flux and its components precipitation, evaporation and runoff at these latitudes share a pronounced seasonal character. At 60-90° N runoff is the main contributor to the freshwater flux, whereas precipitation and evaporation are nearly balanced. Changes occur during the 21st century when the net flux from precipitation and evaporation feeds more strongly into the freshwater flux of the autumn months. This counterbalances the decrease in runoff during these months which is potentially related to the decreasing availability of soil moisture in the Siberian and northern Canadian region (*IPCC*, 2007, reproduced with CCSM3 but not documented in this study).

At 60-90° S the freshwater flux is smaller than at 60-90° N, as is its annual amplitude. During Southern Hemisphere summer months runoff and net flux from precipitation and evaporation each share approximately 50% of the freshwater flux while during winter months runoff is the sole contributor. This substantially changes by the end of the 21st century when precipitation increases and becomes the primary source feeding the freshwater flux to the ocean. Similar to the freshwater flux, the modeled evolution of the freshwater budget in both polar regions shows only minor reactions to the variations of the combined forcing in the pre-industrial period.

A surprisingly large variability among the four transient runs in the pre-industrial period are found for the oceanic freshwater content of the region 60-90° N, whereby a link to specific sequences of natural forcing fluctuation cannot be established. The projected changes due to increasing greenhouse gas concentrations during the 20th and 21st century, however, feature

a significant deviation from the long-term mean of all fluxes involved in the freshwater cycle of the Arctic region. Precipitation, evaporation, runoff and the meridional advection of moisture all increase from the pre-industrial period until the end of the 21st century. The net storage of freshwater in the atmosphere and in the ocean also rise. The net oceanic transport of freshwater is negative (export) and will increase the exported volume. Meanwhile, the freshwater storage in the form of sea ice decreases substantially, as does the export of sea ice.

When the area of interest is reduced to the Arctic Ocean basin only, the simulated changes are even larger, which qualifies the Arctic Ocean as the leading region in terms of freshwater budget changes in the Arctic region. The Arctic Ocean transforms from a net freshwater sink to a massive freshwater source as the influx of freshwater from different sources increases heavily during the 21st century. The freshwater content of the Arctic Ocean clearly leads the oceanic freshwater export. This can partly be explained by the growing sea surface height difference between the Arctic Ocean and surrounding ocean basins.

The liquid freshwater transport through the oceanic passages which confine the Arctic Ocean basin show a definite response to the increasing greenhouse gas concentrations. However, these responses do not occur with the same timing and magnitude among the different passages. Until the end of the 21st century the Fram Strait and CAA triple and double their freshwater export from the Arctic Ocean compared to pre-industrial means, respectively. This clearly dominates the total freshwater transport in the Arctic Ocean which develops this ocean basin into a massive freshwater source to adjacent basins as the climate warms. At the same time, the inflow of freshwater through the Bering Strait is substantially reduced due to an increasing sea surface height gradient between the Arctic Ocean and the North Pacific. Further, a direct relationship between the Fram Strait and the Denmark Strait transport exists in form of the East Greenland Current. The transport through these two passages correlates well, whereby two lags seem to be possible: synchronized fluctuations occur here with zero lag on basis of annual means, while another significant correlation reveals the Denmark Strait to lead the Fram Strait by three to five years. This latter lag is larger during the pre-industrial period compared to the 21st century, prompting the question if the coupling of these two passages will strengthen in the future.

The solid freshwater transport through the oceanic passages shows a more uniform reaction to the changing greenhouse gas forcing than the liquid counterpart and tends to decrease in all passages. The total export of sea ice from the Arctic Ocean is dominated by the Fram Strait and the Barents Sea (the latter actually exports sea ice, in contradiction to observations which do not show any sea ice export). These two passages show a strong correlation and change their export in concert. This is a hint towards their sensitivity to large-scale external forcing such as atmospheric circulation patterns or the Atlantic MOC which possibly influence both passages simultaneously.

The freshwater budget in the Antarctic region experiences slightly different changes from the one in the Arctic region as the greenhouse gas concentrations increase. Precipitation and the meridional advection of moisture also increase significantly whereas evaporation and runoff show only slightly increased values. The exported volume from net oceanic transport rises massively, overcompensating the increased influx from the before mentioned fluxes. The decrease in sea ice transport is substantial as well, but somewhat less pronounced than in the

Arctic region. Despite the increase of fluxes into the ocean its freshwater content undergoes a slight decrease. A reason for this might be the open geographical structure of the Southern Ocean, which enables the ocean to directly discharge increasing influxes into areas north of 60° S (seen as the oceanic freshwater export increases strongly). This is in distinct contrast to the situation at 60-90° N where the Arctic Ocean forms a basin which retains the increasing influx and builds up its freshwater content.

In an integral view of the global four DWF sites, following key findings can be summarized regarding the temporal evolution of the DWF: at all sites but the Weddell Sea a lift of the mixed layer depth occurs with the Ross Sea experiencing the largest lift by far. The Ross Sea differs from the the other DWF sites by building up sea ice rather than melting it. The sea ice production is even increasing in the Ross Sea while the sea ice meltwater decreases at the other sites. That means, the Weddell, GIN and LI Seas all tend to lose the freshwater input from the melting sea ice. Other possible surface freshwater forcings are runoff and $P - E$, which both show a similar increasing trend for all DWF sites. This implies that all these DWF sites which maintain their mixed layer depth, are able to do so due to decreasing sea ice meltwater as this counterbalances the large increase in freshwater from runoff and $P-E$. The Ross Sea, on the other hand, is not counterbalanced by such a trend and responds promptly with a lifted mixed layer depth and a possibly reduced convection.

EQ1500 exhibits a stable Atlantic MOC whereas the different transient runs vary considerably and even take significantly different paths throughout the whole times series. Since the applied forcing is identical for all transient runs, the differences between the runs originate from the different initial conditions. However, all four runs react to the increasing greenhouse gas concentrations and weaken by around 20% throughout the 21st century. In contrast, the MOC at 60° S is weaker and shows more consistency among the four transient runs, whereby this study lacks an explanation. However, the transient runs strengthen by 145-211% during the 21st century and deviate significantly from the long-term mean. Relative changes are therefore considerably larger in the Southern Ocean MOC compared to the Atlantic MOC.

A more detailed analysis of a specific weakening phase of the Atlantic MOC in EQ1500 revealed the two northern DWF sites to interact with the Meridional Overturning in anti-phase. Large changes in the LI Seas upper-ocean properties – partly induced by Denmark Strait and CAA transport anomalies – proceed changes in the MOC. These changes in the MOC provoke a response of the GIN Seas upper-ocean properties as well as the Fram Strait and Barents Sea transport with a lag of 11 and 8 years. This mechanisms is one among several possibilities of interplay between the DWF sites and might be heavily influenced by the MOC natural variability, as this was found to responds rather to certain threshold exceeds than single forcing pulses.

A comparison with observational data qualifies the model to correctly simulate the main features of the freshwater cycle and budget in the polar regions. However, it tends to produce too much sea ice and too fresh conditions in some ocean areas, which has to be taken into account when analysing freshwater budgets in absolute sense. Further, the CCSM3 at T31x3 resolution lacks DWF along the Greenland-Iceland-Scotland ridge system and features a relatively weak DWF site in the GIN Seas.

3.5.2 Related work and comparison to other studies

Regarding the freshwater flux and its components following findings by the IPCC are confirmed in the present study (not all were shown): precipitation is projected to increase in areas of monsoon activity, the tropical Pacific and high latitudes, while a decrease is expected for subtropical regions. At the same time, evaporation will increase in a similar way, mostly balancing the precipitation changes. In polar regions, however, a growing imbalance might emerge from $P - E$. Runoff is increased at high latitudes, particularly in the northern high latitudes, with a notable uncertainty regarding the amplitude of the increase (*IPCC*, 2007).

Wu et al. [2005] were able to simulate the 20^{th} century increase in river runoff at high northern latitudes in close agreement with observations by *Peterson et al.* [2002]. The CCSM3 includes a high resolution river transport model which produces very reasonable runoff values as well. *Wu et al.* [2005] further revealed the increase in runoff to be due to anthropogenic forcing and project the runoff volume to grow further in the 21^{st} century. This again is in line with this study's findings. However, *Wu et al.* [2005] used the IPCC SRES B2 scenario and found the high northern latitudes river runoff to flatten towards mid-21^{st} century, whereas this study uses the A2 scenario and discovers the upward trend to last throughout the 21^{st} century. This might serve as another confirmation of the sensitivity of the simulated river runoff to the projected path of the greenhouse gas emissions, as this is the major difference between the two scenarios used.

The presented results for the Arctic Ocean basin are well within the range of *Holland et al.* [2007], who examined the output of ten general circulation models between 1950 and 2050, using the IPCC SRES A1B scenario (see Fig. 2.6). *Holland et al.* [2007] project significant future changes in several Arctic freshwater transport mechanisms such as $P - E$, sea ice transport and oceanic transport of freshwater. In agreement with the current study these changes are largely attributed to the increase in greenhouse gas concentrations, as this is the common forcing of the different models. The emissions pathway of the A1B and A2 scenario are similar only until mid-21^{st} century. After that the rate of change of Arctic climate parameters decreases in the A1B scenario while they continue to increase under the A2 scenario. Thereby, the dominance by the greenhouse gas concentrations over processes in the Arctic region is demonstrated yet again. Regarding contemporary climatology the simulated runoff and net precipitation in *Holland et al.* [2007] agree well with observations and the inter-model standard deviation is quite small. By contrast, a large range in simulated sea ice and oceanic freshwater transport occurs, which leads *Holland et al.* [2007] to the conclusion that the models as a group do not simulate the ocean and sea ice conditions very well. These findings are confirmed to some extent also within this study, where we find atmospheric and terrestrial quantities to vary little among the four transient runs, whereas quantities like oceanic freshwater storage or the Atlantic MOC show a more stochastic behaviour and spread wide among the transient runs.

Holland et al. [2006] examined simulated trends in the Arctic hydrological cycle using the CCSM3 at T85x1 with the IPCC SRES A1B scenario and therefore predict the major changes in the Arctic to occur within the first half of the 21^{st} century. This again is in apparent contrast to the results obtained from this study's simulation until 2100, where quantities involved in the freshwater budget continuously undergo changes, also - and especially - in the second

half of the 21st century. A prominent example is the annual mean sea ice meltwater flux to the ocean, which is projected to reach positive values by about 2040. This implies that sea ice meltwater acts as a source of freshwater to the ocean rather than a sink. As a consequence, the ocean net budget becomes positive as well by the end of the 21st century and adds to the list of major changes occuring in the second rather than in the first half of the 21st century. Another controversial scenario is proposed by *Koenigk et al.* [2007] using the IPCC SRES A1B scenario: the total freshwater export from the Arctic Ocean is increased only slightly during the 21st century and it is not until the Arctic Ocean freshwater content peaks in 2120 before this freshwater export increases strongly. Whether the major changes in freshwater storage and export from the Arctic Ocean occur during the first or second half of the 21st century or even later seems to be model- and scenario-dependent.

As concerns the different ocean passages delimiting the Arctic Ocean, it became clear that the model resolution of the different passages plays a significant role. The model inter-comparison by *Holland et al.* [2007] showed that the existence or non-existence of an open passage through the CAA significantly influences the upper-ocean salinity in the Baffin Bay and Labrador Sea. If existing, the grid box spacing of the CAA is of importance too and might affect simulations of the freshwater transport through this passage (*Holland et al.*, 2006).

Many models project the CAA together with the Fram Strait to carry out the task of exporting the anomalous Arctic Ocean freshwater storage of the 21st century to the North Atlantic. Together with the build-up of the Arctic Ocean freshwater storage the increasing export of liquid freshwater through the CAA and Fram Stait is the striking change in the Arctic freshwater cycle on which a broad consensus exists. Regarding the liquid freshwater transport through the Fram Strait, the CAA and the Barents Sea trends in this study are consistent with *Holland et al.* [2006]. In *Holland et al.* [2006] the Bering Strait liquid freshwater transport shows negligible trends over the 21st century. This is in contrast to the Bering Strait transport simulated in this study, where the inflow is drastically reduced in the future. Whether this difference arises from the model resolution (T31x3 vs. T85x1 in *Holland et al.*, 2006) or from the different forcing scenarios (IPCC SRES A2 vs. A1B) is not clear. A model performance analysis suggests that the sea ice distribution, which differs significantly between the two model resolutions, contributes to the differences in Bering Strait through-flow (*Yeager et al.*, 2006). Another explanation might be the higher reference salinity of 34.8 psu in *Holland et al.* [2006] compared to 34.7 in this study.

In agreement with other studies (e.g., *Jahn et al.*, 2009) we suggest the sea surface height difference between the Arctic Ocean and southern basins to be a driving mechanism for the export rates of liquid freshwater through the passages. *Jahn et al.* [2009] additionally propose large-scale atmospheric circulation to control the timing of the freshwater export from the Arctic Ocean. This has not been investigated in the present study.

Regarding the DWF sites, several studies examined the sensitivity of Northern Hemisphere DWF sites to increasing greenhouse gas concentrations (e.g., *Holland et al.*, 2006, *Bryan et al.*, 2006, *Koenigk et al.*, 2007). They all found the GIN upper-ocean salinity and density to decrease, however, they attribute the decreasing density to a large part to rising ocean temperatures. This has been proposed in the present study as well. Further, consensus exists on the counterbalancing role the decreasing sea ice has on the GIN Seas upper-ocean

freshwater budget and density. *Koenigk et al.* [2007] projected a significant shoaling of the mixed layer depth in both the GIN and LI Seas which stands in contrast to *Holland et al.* [2006], *Bryan et al.* [2006] and the present study (all CCSM3), which all predicted the mixed layer depths in the GIN Seas to be fairly stable throughout the 21st century. In the LI Seas *Holland et al.* [2006] and *Bryan et al.* [2006] projected a weakening of the DWF which was not rediscovered in this study. This again points towards substantial differences among the models and resolutions concerning simulated climate change in the Arctic.

Jahn et al. [2009] assessed the impact of the liquid freshwater export on the MOC. They found the freshwater export through the Fram Strait into the GIN Seas to explain 20% of the variance of the MOC strength whereas the freshwater export through the CAA into the LI Seas has no significant effect on the MOC. However, they emphasized that the magnitude of the simulated Fram Strait and CAA transport is strongly model-dependent and may vary considerably among studies. In fact, the CCSM3 at T31x3 resolution exhibits a somewhat different behaviour. The presented control simulation shows that the DWF site in the LI Seas more actively influences the MOC than the GIN Seas DWF site. This might be due to the comparably weak GIN Seas convection in the CCSM3 T31x3 (*Bryan et al.*, 2006). Once again, the extensive sea ice coverage of the T31x3 resolution is held responsible and the need for high resolution models when investigating MOC responses is stressed. Further, it was shown that the combined freshwater forcing of the Denmark Strait and the CAA transport strongly affects the upper-ocean properties in the LI Seas on small time scales. Therefore, we cannot deny that the CAA freshwater transport variability has an impact on the MOC.

Yoshimori et al. [2009] used the CCSM3 at T31x3 to investigate decadal oscillations of the Atlantic MOC in a cold climate state. They found the MOC strength to evolve along significantly different paths even when exposed to an identical forcing. *Yoshimori et al.* [2009] suggest that a weakening of the MOC cannot be distinguished as an immediate response of the MOC to external forcing. They conclude that the timing of the response is controlled strongly by unforced internal variability. This is consistent with the findings of the present study.

Chapter 4

Conclusions

This study investigated the natural variability and possible changes in the freshwater cycle and budget in polar regions under transient forcing from 1500 to 2100. However, the main focus of the analysis is on future changes. We use the CCSM3 at T31x3 resolution and applied the IPCC SRES A2 scenario for the 21st century.

The freshwater cycle of the polar regions remained fairly unaffected by solar and volcanic forcing during the pre-industrial period. Strong volcanoes and periods of solar minima were reflected in small precipitation and evaporation changes in the Arctic region. The ocean in both polar regions, however, appeared to be stable throughout the pre-industrial period on basis of annual means. We showed that the zonal mean freshwater flux to the ocean will change substantially with rising greenhouse gas concentrations, and will do so in a non-uniform way across latitudes. In agreement with other model studies we find the ocean in polar regions to receive more freshwater whereas subtropical regions will receive less. In the Arctic region river runoff is mainly responsible for the increase while in the southern high latitudes precipitation plays the dominant role. The hypothesis whether such an asynchronous change in freshwater flux will lead to an inter-hemispheric redistribution of water masses and will actually result in a net transfer of freshwater from the Southern to Northern Hemisphere could not be confirmed yet. Therefore, the analysis of the freshwater cycle needs to be taken onto a hemispheric scale.

Due to its geographical setting the Arctic Ocean is increasingly unable to discharge the freshwater at the rate it is entering this ocean basin via river runoff, $P - E$ and sea ice meltwater. Consequently, the freshwater content in the Arctic Ocean grows substantially. Nevertheless, the export of liquid freshwater from the Arctic Ocean and the total Arctic region north of 60° N is projected to increase strongly as well in the future. In the Southern Ocean on the other hand, where no land mass avoids exchange with adjacent basins, the freshwater content will decrease slightly because freshwater exporting rates in the ocean sharply exceed the importing rates in the atmosphere. This projects both polar regions to exert a feedback on adjacent regions in terms of freshwater forcing. A large part of the projected increase in liquid freshwater export from polar regions is suggested to occur because of the growing meridional sea surface height difference resulting from the density decrease in polar upper-ocean waters. Other possible mechanisms enhancing the freshwater export rate from the polar regions might be long-lasting changes in large-scale atmospheric circulation patterns.

In the Arctic region the ocean passages delimiting the Arctic Ocean all reflect the changing climate by shifts in their freshwater transport. The CAA, the Fram Strait and with that the Denmark Strait all increase their liquid and decrease their solid freshwater transport to southern regions. Together with the increasing surface freshwater flux (runoff and $P - E$ both increase) this has distinguishable consequences for the two DWF sites in the Northern Hemisphere. Both become fresher and lighter in the upper part, whereby the warming ocean contributes to the decreasing density as well. Despite this density increase and freshening, the DWF sites seem to remain in operation. This is due to the weakening freshwater forcing from sea ice. As less sea ice is transported from the Arctic Ocean to the DWF sites, the freshwater influx from the melting of this sea has to decrease. This counteracts to some extent the upper-ocean density decrease due to warming and the increase of all other freshwater fluxes to the DWF sites. However, if Arctic sea ice export fades out completely after 2100, the consequences for the DWF sites might be more dramatic. An outlook on such an event might be possible already in the 21st century when looking at the Southern Ocean. In the DWF site of the Ross Sea no decreasing trend from sea ice meltwater is projected. Therefore, no counteracting to other freshwater fluxes as it appears in all other DWF sites can be expected. And as the freshwater forcing from runoff and $P - E$ strengthens in the Ross Sea, density is actually reduced to the extent that the mixed layer depth is lifted considerably and DWF weakens. The analysis of this process has to be refined however, because not all mechanisms potentially altering the DWF were studied in detail, nor are they included in the coarse-resolution model version.

Further it can be concluded that the often discussed role of the increasing river runoff to the Arctic is not to directly alter DWF and consequently the MOC. Rather it contributes to the build-up of freshwater in the Arctic Ocean and thereby exerts an indirect feedback on the DWF sites when the Arctic Ocean discharges its freshwater through the Fram Strait and the CAA.

The response of the MOC to the increasing greenhouse gas concentrations is profound both in the Atlantic Ocean and at 60° S. However, there are several underlying mechanisms explaining the MOC response and they operate in complex interaction. We suggest a possible interplay between the Denmark Strait/CAA freshwater export and the Atlantic MOC and show that the response in the GIN Seas as well as in the Fram Strait/Barents Sea transport is important. To what extent the freshwater export from the Arctic can be held responsible for the projected future weakening of the Atlantic MOC is still to asses. Meanwhile the Southern Ocean MOC increases strongly in concert with the liquid freshwater export from the Southern Ocean. However, possible feedback processes between changes of the freshwater budget of the Southern Ocean and the strength of the MOC are to be determined in detail and are beyond the scope of this study.

From comparing the presented results with other model studies it became evident that the prescribed greenhouse gas forcing ultimately dominates simulated changes in the polar freshwater cycle. While studies using the IPCC SRES B2 or A1B scenario find the largest changes to occur in the first half of the 21st century, the here used simulations suggest that many parameters of the polar freshwater cycle accelerate their alteration during the complete 21st century, thereby reflecting the continuously rising greenhouse gas concentrations of the A2 scenario used.

Chapter 5

Outlook

The presented study investigated on the one hand large-scale processes such as changes in total freshwater budget of the polar regions and on the other hand, took a more detailed look at local to regional mechanisms such as the local upper-ocean density or the freshwater transport through ocean passages. From this point, the current study could be taken to a broader, hemispheric scale, where the meridional freshwater transfer between latitudinal partitions such as 0-30° N and S, 30-60° N and S and, to sum up, 0-90° N and S could be analysed. This might answer the question whether an actual inter-hemispheric freshwater transfer occurs or if a redistribution takes place only within an individual hemisphere. Another large-scale research path goes towards atmosphere-ocean interaction. A growing number of studies address the possible influence of atmospheric circulation patterns on the distribution of freshwater in the ocean. Extreme freshwater export events from the Arctic Ocean during the 20^{th} century were traced back to strong positive phases of the NAO (*Jahn et al.*, 2009). Therefore, large-scale atmospheric forcing has to be taken into account when studying processes that possibly lead to a discharge of the increasing Arctic Ocean freshwater content.

In contrast, the present study could also be continued towards the examination of small-scale processes and their further changes. The here conducted research lacks in particular a comprehensive investigation of the changing ocean properties. The freshwater transport anomalies found in different ocean passages need to be segmented into changes of velocity and changes in salinity. Further, a closer look has to be taken on whether salinity or temperature changes determine density changes and what responsible mechanisms can be derived therefrom. To enhance the process-understanding in regions of DWF, techniques such as the water-mass transformation function used in *Bryan et al.* [2006] could be applied – especially in the Southern Hemisphere DWF sites, where the present study only briefly addressed ocean changes due to alteration of the freshwater influx. As the sea ice plays an important role for the freshwater budgets of polar regions, its continued investigation is crucial as well. Possible changes of ocean surface heat flux and the transport of heat to high latitudes by ocean currents and atmospheric circulation has to be considered when trying to understand sea ice melting trends. However, in order to follow up this avenue, the grid resolution of the climate model would need to be increased.

Considering the dramatic changes which were projected for the polar regions, a continuation of this research in the framework of a detection and attribution study might lead to new

understanding of changing mechanisms in the ocean.

Even though addressed in numerous studies, the dynamics of the MOC, and processes controlling and possibly altering it in the future, are not completely understood. More efforts are necessary in trying to quantify the impact of retreating sea ice and increasing freshwater fluxes on the stability of the DWF sites and, following from that, the MOC. As we showed, the MOC evolves on fairly different paths when started from different initial conditions with the CCSM3 at T31x3. While the signal of the rising greenhouse gas forcing is well visible, the causes for the fluctuations during the pre-industrial period remain unknown. Internal variability and the effect of external forcing such as volcanoes and solar variability are potential mechanisms which are currently discussed (*D. Hofer*, personal communication, 2009). Thereby, the feasibility of the low-resolution version of the CCSM3 for studying DWF and MOC responses might be addressed as well, as the question of resolution arises frequently from model studies.

This study's focus was on the future changes in the freshwater cycle, whereas pre-industrial natural variability of the parameters participating in the freshwater cycle was addressed only shortly. However, an improved understanding of past changes by analysing the model results of the pre-industrial period and comparing it with proxy-data is crucial. Mechanisms detected in the past might be tracked to the present and the future and help to explain observed and simulated changes in the freshwater cycle and the climate system as a whole.

Appendix A

Ocean data

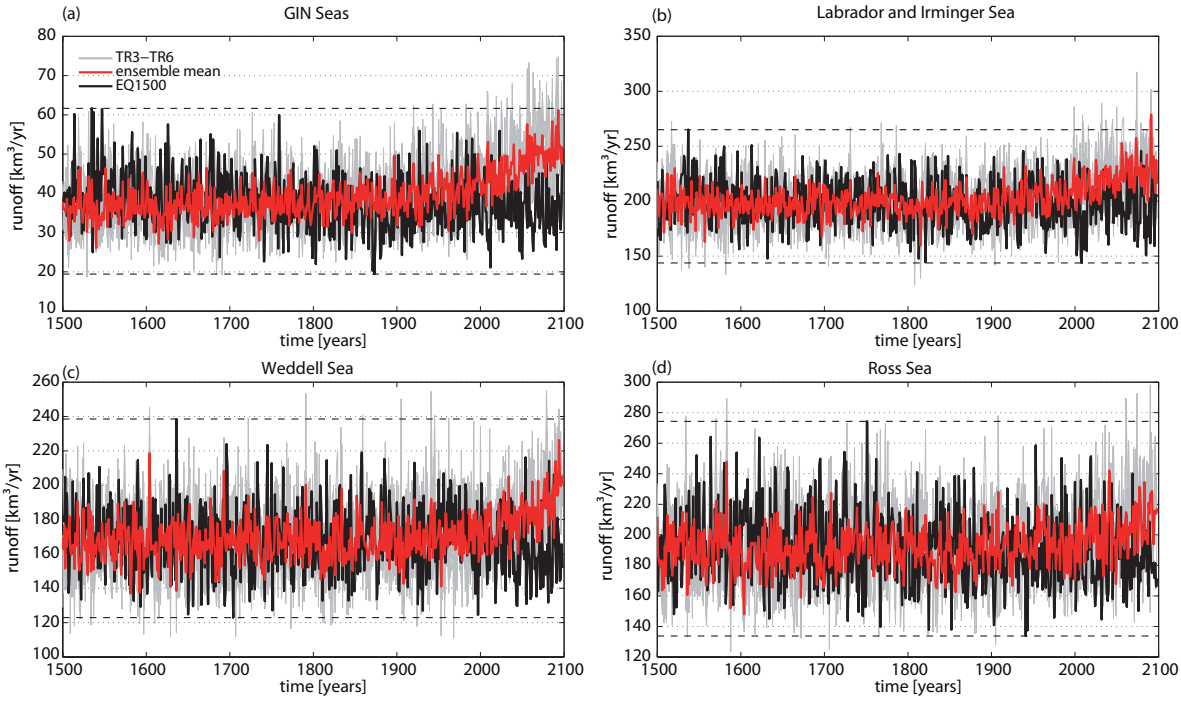

Figure A.1: Temporal evolution of the annual mean runoff to the GIN Seas (a), Labrador and Irminger Sea (b), Weddell Sea (c) and Ross Sea (d), integrated over the areas defined in Fig. 3.24. Dashed black lines denote the spread of EQ1500. The legend in (a) is valid for (b), (c) and (d) as well.

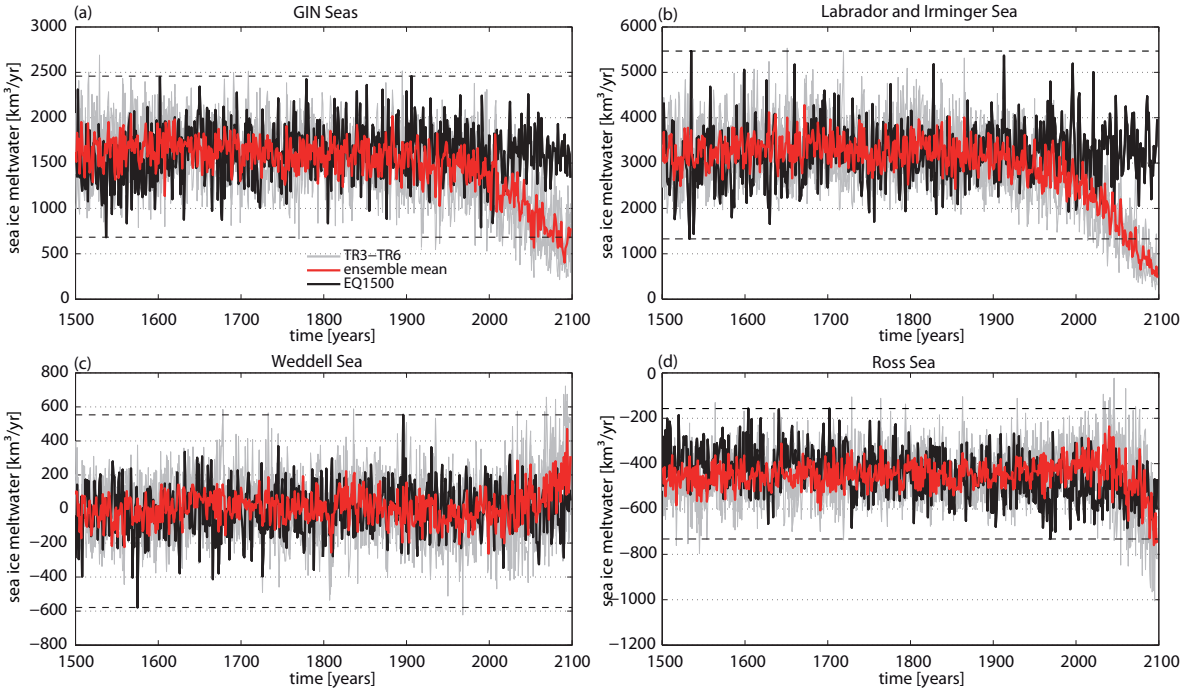

Figure A.2: Temporal evolution of the annual mean sea ice meltwater flux to the GIN Seas (a), Labrador and Irminger Sea (b), Weddell Sea (c) and Ross Sea (d), integrated over the areas defined in Fig. 3.24. Dashed black lines denote the spread of EQ1500. The legend in (a) is valid for (b), (c) and (d) as well.

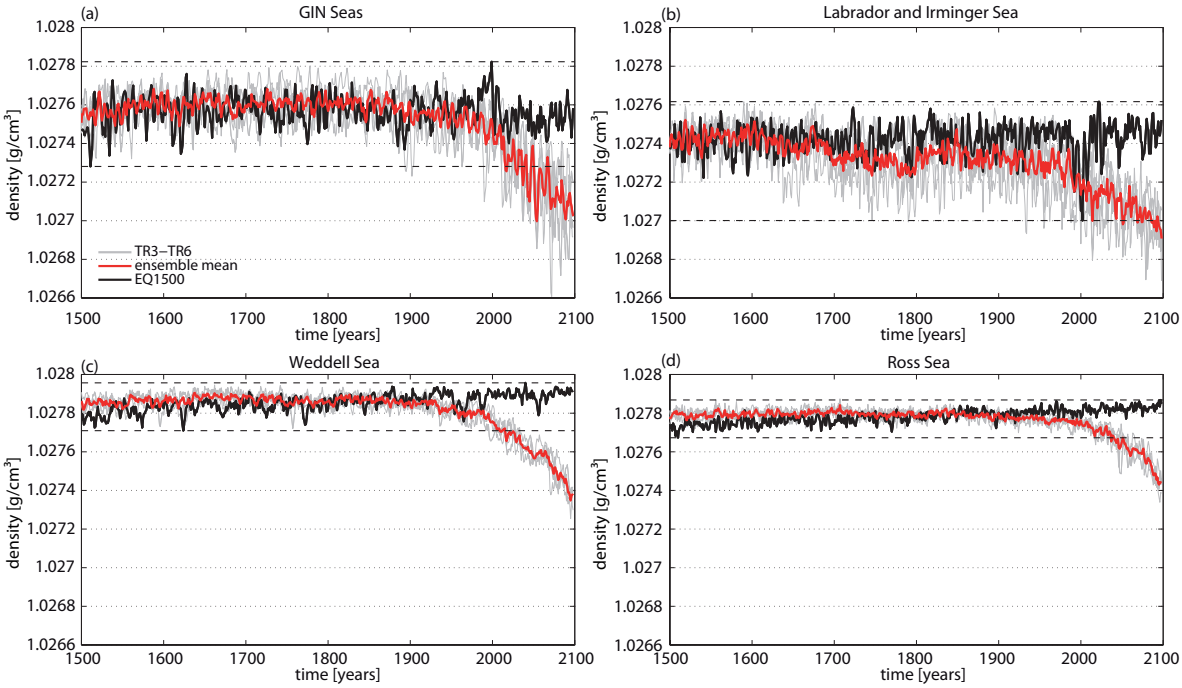

Figure A.3: Temporal evolution of the annual mean density of the top 104 meters in the GIN Seas (a), Labrador and Irminger Sea (b), Weddell Sea (c) and Ross Sea (d), averaged over the areas defined in Fig. 3.24. Dashed black lines denote the spread of EQ1500. The legend in (a) is valid for (b), (c) and (d) as well.

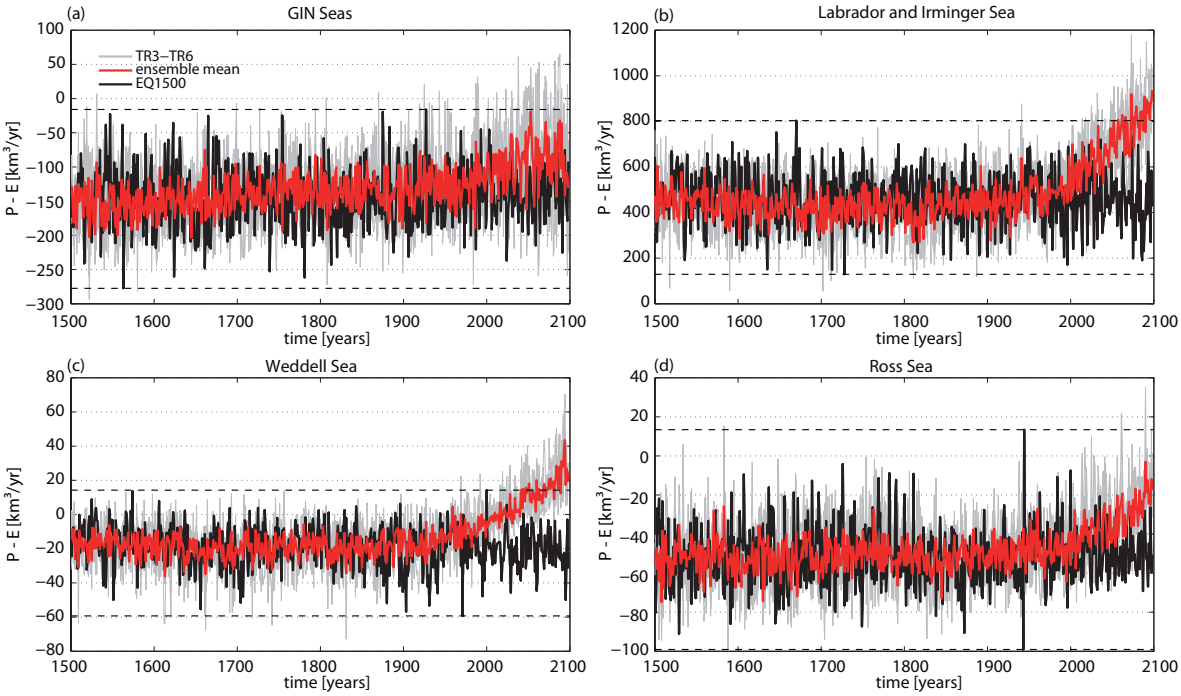

Figure A.4: Temporal evolution of the annual mean precipitation minus evaporation flux to the GIN Seas (a), Labrador and Irminger Sea (b), Weddell Sea (c) and Ross Sea (d), integrated over the areas defined in Fig. 3.24. Dashed black lines denote the spread of EQ1500. The legend in (a) is valid for (b), (c) and (d) as well.

List of Tables

2.1 List of simulations 20

3.1 Freshwater budget of the Arctic Ocean 41
3.2 Freshwater budgets in the Arctic region 65
3.3 Freshwater flux through oceanic straits delimiting the Arctic Ocean 66
3.4 Precipitation and evaporation of the Antarctic continental ice sheet 68

List of Figures

1.1 Thermohaline Circulation 2
1.2 Surface air temperature 60°-90° N and 60°-90° S 7
1.3 Pan-arctic region watershed 8
1.4 Northern and southern high latitudes ocean bathymetry 8
1.5 Ocean currents in the Arctic region 9

2.1 CLM RTM flow chart 15
2.2 RTM river flow January 2011 and average 2011-2021 16
2.3 Line integration in SCRIP 18
2.4 Overlapping cells between RTM and POP 19
2.5 Natural and anthropogenic forcing used in the simulations 21
2.6 SRES scenario families 22
2.7 Global mean 2m temperature of EQ1500 23
2.8 Grid boxes at 60° N and 60° S on the displaced-pole grid and interpolation scheme 25

3.1 Hovmöller diagram of annual mean freshwater flux anomaly 1990-2098 27
3.2 Hovmöller diagram of annual mean freshwater flux anomaly 1990-2098 28
3.3 Hovmöller diagram of annual mean freshwater flux anomaly 1500-2098 29
3.4 Hovmöller diagram of annual mean freshwater flux anomaly 1500-2098 of EQ1500 29
3.5 Spatially integrated freshwater flux 60°-90° N and 60°-90° S 30
3.6 100-year average freshwater flux from EQ1500 60°-90° N and 60°-90° S 30
3.7 Spatial structure of annual mean precipitation, evaporation, runoff and sea ice meltwater from EQ1500 32
3.8 Hovmöller diagram of precipitation, evaporation and runoff anomaly 1500-2098 33
3.9 Freshwater flux annual cycle 60°-90° N 34
3.10 Freshwater flux annual cycle 60°-90° S 35
3.11 Freshwater flux 50-year moving window standard deviation 60°-90° N and 60°-90° S 36
3.12 Freshwater budget 60-90° N 38
3.13 Oceanic freshwater budget 60-90° N 39
3.14 Oceanic freshwater content 60-90° N 43
3.15 Freshwater budget Arctic Ocean 44
3.16 Freshwater budget 60-90° S 45
3.17 Oceanic freshwater budget 60-90° S 46
3.18 Mean wind field over the North Pacific 48

3.19 Sea surface height difference between the Arctic Ocean and the North Pacific 48
3.20 Liquid freshwater transport out and into the Arctic Ocean 49
3.21 Solid freshwater transport out and into the Arctic Ocean by means of sea ice 49
3.22 Liquid freshwater transport through Fram Strait and Denmark Strait 51
3.23 Total liquid freshwater transport out and into the Arctic Ocean and Arctic Ocean freshwater content 51
3.24 Areas of deep water formation in the CCSM3 T31x3 52
3.25 Salinity in the GIN Seas, Labrador and Irminger Sea, Weddell Sea and Ross Sea 55
3.26 Mixed layer depth in the GIN Seas, Labrador and Irminger Sea, Weddell Sea and Ross Sea 55
3.27 Atlantic Meridional Overturning 58
3.28 Southern Ocean Meridional Overturning 58
3.29 Response to Atlantic MOC changes 60
3.30 Overview 62
3.31 Sea surface salinity in the Arctic region 63
3.32 River runoff into the Arctic Ocean 67
3.33 Meridional water vapour flux 60-90° S 68

A.1 Runoff in the GIN Seas, Labrador and Irminger Sea, Weddell Sea and Ross Sea 80
A.2 Sea ice meltwater in the GIN Seas, Labrador and Irminger Sea, Weddell Sea and Ross Sea 81
A.3 Density in the GIN Seas, Labrador and Irminger Sea, Weddell Sea and Ross Sea 81
A.4 Precipitation minus evaporation in the GIN Seas, Labrador and Irminger Sea, Weddell Sea and Ross Sea 82

References

ACIA, *Impacts of a Warming Arctic*, Arctic Climate Impact Assessment, Cambridge University Press, 2004.

Ammann, C. M., G. A. Meehl, W. M. Washington, and Z. C. S., A monthly and latitudinally varying volcanic forcing dataset in simulations of 20th century climate, *Geophys. Res. Let., 30*, 1657–1660, 2003.

Antonov, J. I., R. A. Locarnini, T. P. Boyer, A. V. Mishonov, and H. E. Garcia, *World Ocean Atlas 2005, Volume 2: Salinity*, U.S. Government Printing Office, Washington, D.C., 2006.

Baringer, M. O., and J. C. Larsen, Sixteen Years of Florida Current Transport at 27° N, *Geophys. Res. Let., 28*, 3179–3182, 2001.

Beven, K. J., and M. J. Kirkby, A Physically Based Variable Contributing Area Model of Basin Hydrology, *Hydrol. Sci. Bull., 24*, 43–69, 1979.

Blunier, T., J. Chappellaz, J. Schwander, B. Stauffer, and D. Raynaud, Variations in atmospheric methane concentration during the Holocene epoch, *Nature, 374*, 46–49, 1995.

Boyer, T., S. Levitus, J. I. Antonov, R. A. Locarnini, and H. E. Garcia, Linear trends in salinity for the World Ocean, 1955-1998, *Geophys. Res. Let., 32*, 2005.

Brix, H., and R. Gerdes, North Atlantic Deep Water and Antarctic Bottom Water: Their interaction and influence on the variability of the global ocean circulation, *J. Geophys. Res., 108*, 2003.

Broecker, W., G. Bond, M. Klas, E. Clark, and J. McManus, Origin of the northern Atlantic's Heinrich events, *Clim. Dyn., 6*, 265–273, 1992.

Broecker, W. S., S. Sutherland, and T.-H. Peng, A Possible 20th-Century Slowdown of Southern Ocean Deep Water Formation, *Science, 286*, 1132–1135, 1999.

Bromwich, D. H., and R. L. Fogt, Strong Trends in the Skill of the ERA-40 and NCEP-NCAR Reanalyses in the High and Midlatitudes of the Southern Hemisphere, 1958-2001, *J. Clim., 17*, 4603–4619, 2004.

Bryan, F. O., G. Danabasoglu, N. Nakashiki, Y. Yoshida, D.-H. Kim, J. Tsutsui, and S. C. Doney, Response of the North Atlantic Thermohaline Circulation and Ventilation to Increasing Carbon Dioxide in CCSM3, *J. Clim., 19*, 2382–2397, 2006.

Collins, W. D., P. J. Rasch, B. A. Boville, J. J. Hack, D. L. McCaa, D. L. Williamson, C. M. Briegleb, S. J. Bitz, S. J. Lin, and M. Zhang, The formulation and atmospheric simulation of the Community Atmosphere Model: CAM3, *J. Clim., 19*, 2144–2161, 2006.

Crowley, T. J., Causes of climate change over the past 1000 years, *Science, 289*, 270–277, 2000.

Cunningham, S. A., T. Kanzow, D. Rayner, M. O. Baringer, W. E. Johns, J. Marotzke, H. R. Longworth, E. M. Grant, J. J.-M. Hirschi, L. M. Beal, C. S. Meinen, and H. L. Bryden, Temporal Variability of the Atlantic Meridional Overturning Circulation at 26.5°N, *Science, 317*, 935–938, 2007.

Curry, R., B. Dickson, and I. Yashayaev, A change in the freshwater balance of the Atlantic Ocean over the past four decades, *Nature, 426*, 826–829, 2003.

Dickson, B., I. Yashayaev, J. Meincke, W. R. Turrell, S. Dye, and J. Holfort, Rapid freshening of the deep North Atlantic Ocean over the past four decades, *Nature, 416*, 832–837, 2002.

Dickson, R. R., T. J. Osborn, J. W. Hurrell, J. Meinke, J. Blindheim, B. Adlandsvik, T. Vinje, G. Alekseev, and W. Maslowski, The Arctic Ocean Response to the North Atlantic Oscillation, *J. Clim., 13*, 2671–2696, 2000.

Etheridge, D. M., L. P. Steele, R. L. Langenfelds, R. J. Francey, J.-M. Barnola, and V. I. Morgan, Natural and anthropogenic changes in atmospheric CO_2 over the last 1000 years from air in Antarctic ice and firn, *J. Geophys. Res., 101*, 4115–4128, 1996.

Flückiger, J., A. Dällenbach, B. Stauffer, T. F. Stocker, D. Raynaud, and J.-M. Barnola, Variations in Atmospheric N_2O Concentration During Abrupt Climatic Changes, *Science, 285*(227), 1999.

Flückiger, J., E. Monnin, B. Stauffer, J. Schwander, T. F. Stocker, J. Chappellaz, D. Raynaud, and J.-M. Barnola, High-resolution Holocene N_2O ice core record and its relationship with CH_4 and CO_2, *Global Biogeochemical Cycles, 16*(L1010), 2002.

Gerten, D., S. Rost, W. von Bloh, and W. Lucht, Causes of change in 20th century global river discharge, *Geophys. Res. Let., 35*, 2008.

Graham, S. T., J. S. Famiglietti, and D. R. Maidment, Five-Minute, 1/2°, and 1°Data Sets of Continental Watersheds and River Networks for Use in Regional and Global Hydrologic and Climate System Modeling Studies, *Water Resour. Res., 35*, 1999.

Groves, D. G., and J. A. Francis, Variability of the Arctic atmospheric moisture budget from TOVS satellite data, *J. Geophys. Res., 107*, 2002.

Hansen, B., W. R. Turrell, and S. Østerhus, Decreasing overflow from the Nordic seas into the Atlantic Ocean through the Faroe Bank channel since 1950, *Nature, 411*, 927–930, 2001.

Hattermann, T., and A. Levermann, Response of Southern Ocean circulation to global warming may enhance basal ice shelf melting around Antarctica, *Clim. Dyn.,*, doi 10.1007/s00382–009–0643–3, in press, 2010.

Heinrich, H., Origin and consequences of cyclic ice rafting in the northeast Atlantic Ocean during the past 130,000, *Quat. Sci. Rev.,*, 143–152, 1988.

Hemming, S. R., Heinrich events: Massive late Pleistocene detritus layers of the north atlantic and their global climate imprint, *Reviews of Geophysics, 42*, 2004.

Holland, M. M., J. Finnis, A. P. Barrett, and M. C. Serreze, Projected changes in Arctic Ocean freshwater budgets, *J. Geophys. Res., 112*, G04S55, 2007.

Holland, M. M., J. Finnis, and M. C. Serreze, Simulated Arctic Ocean Freshwater Budgets in the Twentieth and Twenty-First Centuries, *J. Clim., 19*, 6221–6242, 2006.

IPCC, *Climate Change 2007, The Science of Climate Change*, Intergovernmental Panel on Climate Change, Cambridge University Press, 2007.

IPCC SRES, *Special Report on Emissions Scenarios*, Intergovernmental Panel on Climate Change, Cambridge University Press, 2000.

Jahn, A., B. Tremblay, L. A. Mysak, and R. Newton, Effect of the large-scale atmospheric circulation on the variability of the Arctic Ocean freshwater export, *Clim. Dyn.,*, 2009.

Jones, P. W., First- and Second-Order Conservative Remapping Schemes for Grids in Spherical Coordinates, *Mon. Weather Rev., 127*, 2204–2210, 1999.

Jones, P. W., A User's Guide for SCRIP: A Spherical Coordinate Remapping and Interpolation Package, *Los Alamos National Laboratory, Los Alamos, NM*, *Tech. Rep.*, 2001.

Joos, F., and R. Spahni, Rates of change in natural and anthropogenic radiative forcing over the past 20,000 years, *Proc. US Natl. Acad. Sci., 105*, 1425–1430, 2008.

Karcher, M., R. Gerdes, F. Kauker, C. Köberle, and I. Yashayae, Arctic Ocean change heralds North Atlantic freshening, *Geophys. Res. Let., 32*, L21606, 2005.

Käse, R. H., J. B. Girton, and T. B. Sanford, Structure and variability of the Denmark Strait Overflow: Model and observations, *J. Geophys. Res., 108*, 2003.

Kauffmann, B. G., R. Jacob, T. Craig, and W. G. Large, The CCSM Coupler Version 6.0. User's Guide, Source Code Reference and Scientific Description, *National Center for Atmospheric Research, Boulder, CO.80307-3000*, *Tech. Rep.*, 2004.

Kiehl, J. T., C. A. Shields, J. J. Hack, and W. D. Collins, The Climate Sensitivity of the Community Climate System Model Version 3 (CCSM3), *J. Clim., 19*, 2584–2596, 2006.

Köberle, C., and R. Gerdes, Simulated Variability of the Arctic Ocean Freshwater Balance 1948-2001, *J. Phys. Oceanogr., 37*, 1628–1644, 2006.

Koenigk, T., U. Mikolajewicz, H. Haak, and J. Jungclaus, Arctic freshwater export in the 20th and 21st centuries, *J. Geophys. Res., 112*, G04S41, 2007.

Kuhlbrodt, T., A. Griesel, M. Montoya, A. Levermann, M. Hofmann, and S. Rahmstorf, On the driving processes of the Atlantic Meridional Overturning Circulation, *Reviews of Geophysics, 45*, /2004RG000166, 2007.

Lean, J., and R. Bradley, Reconstruction fo solar irradiance since 1610: Implications for climate change, *Geophys. Res. Let., 22(23)*, 3195–3198, 1995.

Lüthi, D., M. Le Floch, B. Bereiter, T. Blunier, J.-M. BArnola, U. Siegenthaler, D. Raynaud, J. Jouzel, H. Fischer, K. Kawamura, and T. F. Stocker, High-resolution carbon dioxide concentration record 650,000-800,000 years before present, *Nature, 453*, 379–182, 2008.

Meehl, G. A., W. M. Washington, B. D. Santer, W. D. Collins, J. M. Arblaster, A. Hu, D. M. Lawrence, H. Teng, L. E. Buja, and W. G. Strand, Climate Change Projections for the Twenty-First Century and Climate Change Commitment in the CCSM3, *J. Clim., 19*, 2597–2616, 2006.

Monaghan, A. J., D. H. Bromwich, and S.-H. Wang, Recent trends in Antarctic snow accumulation from Polar MM5 simulations, *Phil. Trans. Roy. Soc., London, 364*, 1683–1708, 2006.

NATO, *The Freshwater Budget of the Arctic Ocean*, NATO Science Partnership, Springer, 644 pp., 2000.

Oleson, K. W., Y. Dai, G. Bonan, M. Bosilovich, R. Dickinson, F. Dirmeyer, P. Hoffman, P. Houser, S. Levis, G.-Y. Niu, P. Thornton, M. Vertenstein, Z.-L. Yang, and X. Zeng, Technical description of the Community Land Model (CLM). Technical Report NCAR/TN-461+STR, National Center for Atmospheric Research, Boulder, CO.80307-3000, *Tech. Rep.*, 2004.

Peterson, B. J., R. M. Holmes, J. W. McClelland, C. J. Vörösmarty, R. B. Lammers, A. I. Shiklomanov, I. A. Shiklomanov, and S. Rahmstorf, Increasing River Discharge to the Arctic Ocean, *Science, 298*, 2171–2173, 2002.

Peterson, B. J., J. W. McClelland, R. Curry, R. M. Holmes, J. E. Walsh, and K. Aagaard, Trajectory Shifts in the Arctic and Subarctic Freshwater Cycle, *Science, 313*, 1061–1066, 2006.

Quéré, C. L., M. Raupach, P. Ciais, T. Conway, C. Field, S. Houghton, G. Marland, and P. Canadell, Global Carbon Project (2008) Carbon budget and trends 2007, [www.globalcarbonproject.org, 26 september 2008], *Global Carbon Project (2008)*, *Tech. Rep.*, 2008.

Rahmstorf, S., Bifurcations of the Atlantic thermohaline circulation in response to changes in the hydrological cycle, *Nature, 378*, 145–149, 1995.

Row, L. W., D. A. Hastings, and P. K. Dunbar, TerrainBase Worldwide Digital Terrain Data, CD-ROM and Documentation Manual, *NOAA. National Geophysical Data Center, Boulder, CO*, *Tech. Rep.*, 1995.

Schmittner, A., and T. F. Stocker, The stability of the thermohaline circulation in global warming experiments, *J. Clim., 12*, 1117–1133, 1999.

Serreze, M., A. Barrett, A. Slater, R. Woodgate, K. Aagaard, R. Lammers, M. Steele, R. Moritz, M. Meredith, and C. Lee, The large-scale freshwater cycle of the Arctic, *J. Geophys. Res., 111*, /2005JC003424, 2006.

Steele, M., R. Morley, and W. Ermold, A global ocean hydrography with a high-quality Arctic Ocean, *J. Clim., 14*, 2079–2087, 2001.

Stocker, T. F., Past and future reorganizations in the climate system, *Quat. Sci. Rev., 19*, 301–319, 2000.

Stocker, T. F., and C. C. Raible, Water cycle shifts gear, *Nature, 434*, 830–832, 2005.

Stocker, T. F., and A. Schmittner, Influence of CO_2 emission rates on the stability of the thermohaline circulation, *Nature, 388*, 862–865, 1997.

Swingedouw, D., T. Fichefet, P. Huybrechts, H. Goosse, E. Driesschaert, and M.-F. Loutre, Antarctic ice-sheet melting provides negative feedbacks on future climate warming, *Geophys. Res. Let., 35*, L17705, 2008.

Thompson, D. W. J., and J. M. Wallace, Regional climate impacts of the northern hemisphere annular mode, *Science, 293*, 85–89, 2001.

Tietäväinen, H., and T. Vihma, Atmospheric moisture budgets over Antarctica and the Southern Ocean based on the ERA-40 reanalysis, *International Journal of Climatology, 28*, 1977–1995, 2008.

Vellinga, M., and R. A. Wood, Global climatic impacts of a collapse of the Atlantic Thermohaline Circulation, *Clim. Change, 54*, 251–267, 2002.

White, D., L. Hinzmann, L. Alessa, J. Cassano, M. Chambers, K. Falkner, J. Francis, W. J. Gutowski, M. Holland, R. M. Holmes, H. Huntington, D. Kane, A. Kliskey, C. Lee, J. McClelland, B. Peterson, T. S. Rupp, F. Straneo, M. Steele, R. Woodgate, D. Yang, K. Yoshikawa, and T. Zhang, The arctic freshwater system: Changes and impacts, *J. Geophys. Res., 112*, G04S54, 2007.

Wu, P., and M. J. Rodwell, Gulf stream forcing of the winter North Atlantic oscillation, *Atmospheric Science Letters, 5*, 57–64, 2004.

Wu, P., R. Wood, and P. Stott, Human influence on increasing Arctic river discharge, *Geophys. Res. Let., 32*, 2004GL021570, 2005.

Wu, P., R. Wood, P. Stott, and G. S. Jones, Deep North Atlantic freshening simulated in a coupled climate model, *Progress in Oceanography, 73*, 370–383, 2007.

Yeager, S. G., C. A. Shields, W. G. Large, and J. J. Hack, The Low-Resolution CCSM3, *J. Clim., 19*, 2545–2566, 2006.

Yoshimori, M., C. C. Raible, T. F. Stocker, and M. Renold, Simulated decadal oscillations of the Atlantic meridional overturning circulation in a cold climate state, *Clim. Dyn.*,, 2009.

Acknowledgements

I would like to thank...

... Thomas Stocker for encouraging me to write my thesis at the Climate and Environmental Physics department, for interesting and stimulating discussions, for keeping me on track and for his support during the whole year.

... Christoph Raible and Dominik Hofer for always lending an open ear, for their enormous patience in explaining technical details and for their help in keeping my motivation high and my fears small.

... Reidun Gangstø, Karin Weiler, Markus Gerber, Tobias Tschumi and Siswanto for the pleasant working atmosphere in the office.

... Markus Gerber and Thomas Frölicher in specific for their support as well as for introducing me to the future Swiss football champion.

... Kay Bieri and Doris Rätz for their excellent support. Special thanks to Kay for saving the data from my mortally wounded notebook.

... all the other people at KUP who contribute to the lively and comfortable atmosphere at the department.

... the "Climate Guerillas" Alex Nauels, Beni Stocker, Anil Bozbiyik, Philippe Wäger and Silvan Aerni for the frequent mental rehabilitation sessions, the pleasant lunch breaks and for making the time in Bern so memorable.

... Giuliana for her love and patience and for keeping the non-scientific part in me alive.

... my family for their support during my never-ending story of education.

... my dear friends Basil, Tobi and Remo in Basel for appreciating my sporadic returns and for being reliable agents of mental distraction.